SRC TR 75-148
October 1976

Copy ___ of 15

See 1473 in back

COHERENT AND WIDEBAND IMAGING ANALYSIS WORKBOOK

Contract F41689-75-C-0141
Contract F41689-77-C-0006

Prepared for

U.S. Air Force
Air Training Command
Randolph Air Force Base, Texas

File No. D0140

SYRACUSE RESEARCH CORPORATION, MERRILL LANE, SYRACUSE, NEW YORK 13210

FOREWORD

This workbook was originally prepared by the Syracuse Research Corporation (SRC) for use in a training course sponsored by the U.S. Air Force Air Training Command under Contract F41689-75-C-0141. It is reprinted here in its entirety with corrections for the current course being presented under Contract F41689-77-C-0006. The notes presented in this workbook represent a substantial portion of the material for a three-week training course covering coherent and wideband imaging analysis.

The notes presented in this document were prepared by A. Moceyunas and Dr. R. Wallenberg, both of SRC. This document is identified as SRC TR 75-148.

TABLE OF CONTENTS

Section 1 — Coherent Processing Methods

SECTION 1

COHERENT PROCESSING METHODS

1.1 COHERENT SIGNAL THEORY

1.1a Review of the Complex Representation of a Radar Signal

A radar signal in its simplest "real world" form may be regarded as a quantity whose time variation is sinusoidal with carrier frequency ω. This form of time variation is sometimes described as time harmonic. In space the signal is an electromagnetic field, and within the radar hardware it may be regarded as a voltage or current. When the radar signal is of this form, mathematical analyses may be simplified by using complex quantities. The basis for this is Euler's identity

$$e^{j\alpha} = \cos\alpha + j \sin\alpha \tag{1-1}$$

where $j = \sqrt{-1}$. This gives a relationship between real sinusoidal functions and the complex exponential function.

In its simplest form, a sinusoidal quantity, such as a voltage, might be represented as

$$v(t) = V_o \cos(\omega t + \alpha) \tag{1-2}$$

where V_o and α can be a function of time. We can also write (1-2) in complex exponential form as

$$v(t) = \mathrm{Re}(V_o\, e^{j(\omega t + \alpha)}) \tag{1-3}$$

The notation Re( ) stands for "the real part of," that is, the part not associated with j when in the form of the right hand side of (1-1). Equation (1-3) can also be written in the form

$$v(t) = \mathrm{Re}(V\, e^{j\omega t}) \tag{1-4}$$

where

$$V = V_o\, e^{j\alpha} \tag{1-5}$$

is the complex signal.

The complex signal V is defined by its magnitude, V_o, and phase, α, or by its real (in-phase) and imaginary (out-of-phase) parts, $V = a' + ja''$. Equation (1-4) states that the instantaneous voltage, v(t), may be found by multiplying the complex signal V by $e^{j\omega t}$ and taking the real part of the result.

It is convenient to analyze radar signals in terms of their complex signal representation given by (1-5) (magnitude and phase) and omit their sinusoidal time dependence. (When an instantaneous time representation is desired, we can use (1-4).) In this way, we avoid having to repetitively write $\sin\omega t$ to show the harmonic time dependence of a signal. The time dependence is assumed in the complex signal representation.

Complex notation is convenient and easy to use in analyzing linear processes. A necessary condition for processes to be linear is that the principle of superposition holds. To analyze the combined effect of a number of excitations, we can start with the effect of each individual excitation as if the other excitations were not present and then combine the results. In addition, for linear systems, the response is directly proportional to the forcing function, that is, the magnitude of the scale factor is preserved.

The computation of power is an example of a nonlinear computation which does not obey the rules of linear processes. Instantaneous power is normally defined as $p(t) = v(t)\, i(t)$, where i(t) is the instantenous current associated with a voltage v(t). For our purposes, assume that the voltage v(t) appears across a 1 ohm resistor so that $p(t) = [v(t)]^2$. Then, assuming v(t) is of the form (1-2),

$$p(t) = V_o^2 \cos^2(\omega t + \alpha)$$

$$= \frac{1}{2} V_o^2 [1 + \cos(2(\omega t + \alpha))] \qquad (1\text{-}7)$$

The time average of the power is given by

$$\overline{p} = \frac{1}{2} V_o^2 \qquad (1\text{-}8)$$

where the bar denotes time average.

For the following, we shall need the concept of complex conjugate quantities, denoted by *, and defined as follows. If $A = a' + ja'' = |A|\, e^{j\alpha}$, the conjugate of A is $A^* = a' - ja'' = |A|\, e^{-j\alpha}$. It follows from this that $AA^* = |A|^2$.

We now construct an expression for the instantaneous power using the complex signal representation by noting that

$$VV^* = |V|^2 = V_o^2 \tag{1-9}$$

It is evident that the equivalent of (1-7) is

$$p(t) = \frac{1}{2}\, \mathrm{Re}(VV^* + (Ve^{j\omega t})^2) \tag{1-10}$$

from which it follows that the time average power is

$$\bar{p} = \frac{1}{2}\, |V|^2 \tag{1-11}$$

It is important to note here that one cannot obtain the correct expression for instantaneous power by forming the real part of $(Ve^{j\omega t})^2$.

1.1b Radar Cross Section Definitions

In most radar applications, the same antenna is used for transmission and reception. One is interested here in detecting a target, which may be characterized by its "scattering cross section". The scattering cross section, σ, is defined as the effective area intercepting that amount of power which, when scattered isotropically, produces an echo equal to that observed from the target. If the power flux density incident at the scatterer is S_i, then the power intercepted by the target is σS_i. If this power is reradiated isotropically, the flux density S_r at a receiving point a large distance, R, away is $\sigma S_i / 4\pi R^2$. This leads to the equation for the radar cross section

$$\sigma = \lim_{R\to\infty} 4\pi R^2\, \frac{S_r}{S_i} \tag{1-12}$$

Another descriptive definition of σ, which should be obvious from (1-12), is that the radar cross section is the power scattered into a unit solid angle divided by the incident power per unit area.

The electric and magnetic fields, $\vec{E}$ and $\vec{H}$, transmitted by an antenna and scattered by a target are vector quantities denoted by arrows; that is, they are fields which have a prescribed polarization. For plane waves, the electric and magnetic fields are orthogonal to each other and are both orthogonal to the direction of propagation. In addition, their magnitudes are related by the impedance of free space; that is, $|\vec{E}| = \eta|\vec{H}|$, where $\eta \approx 377$ ohms. The power flux density, or Poynting vector, associated with a plane wave electromagnetic field is given by $S = |\vec{E}|^2/\eta = \eta|\vec{H}|^2$. The definition of the radar cross section can then be written from (1-12) as

$$\sigma = \underset{R\to\infty}{4\pi R^2} \left|\frac{\vec{E}^s}{\vec{E}^i}\right|^2 = \underset{R\to\infty}{4\pi R^2} \left|\frac{\vec{H}^s}{\vec{H}^i}\right|^2 \tag{1-13}$$

where particular polarizations must be specified for $\vec{H}$ and $\vec{E}$, i.e., σ is a function of the transmit and receive polarizations.

To relate radar cross section to practical radar system parameters, it is useful to define the effective area of a matched receiving system as

$$A_r(\theta, \phi) = \frac{\lambda^2}{4\pi} G(\theta, \phi) \tag{1-14}$$

where λ is the wavelength and $G(\theta, \phi)$ is the gain of the antenna system. The gain is defined as the ratio of the power radiated in a given direction per unit solid angle to the average power radiated per unit solid angle. Thus, $G(\theta, \phi)$ expresses the increase in power radiated in a given direction by the antenna over that from an isotropic radiator emitting the same total power. It is independent of the actual power level.

The effective receiving area, A_r, relates the power flux density at the antenna to the total power received, P_r, as $P_r = S_r A_r$. If the total transmitted power is P_t, then the power flux density, S_i, in the direction (θ, ϕ) is $S_i = (P_t/4\pi R^2)G_t$. Upon making these substitutions in (1-12) and using (1-14), we obtain

$$\sigma = \frac{(4\pi)^3 R^4 P_r}{G_r G_t P_t \lambda^2} \tag{1-15}$$

where G_r and G_t refer to receive and transmit antenna gains. Equation (1-15) gives an expression for calculating radar cross section if the transmitted power, P_t, and received power, P_r, are known. In this expression, G_r and G_t are dimensionless, P_r and P_t are in the same units, R and λ are in the same units, and σ is in square units of λ or R.

1.1c Elementary Point Target Theory

Signal reflections from most practical tracking radar targets tend to arise from localized regions on the targets in a manner which gives at least some validity to characterizing such targets as collections of rigidly-connected point scatterers. A particular idealization of a set of points in terms of their locations and scattering amplitudes may hold only for a narrow region of aspect angles, and different arrangements of points may be applicable for different regions of aspect angles. Targets at some aspects may not be as well modeled by collections of points as others, and some targets may not be amenable to this idealization at any aspect.

Assume a target made up of a number of point scatterers for which individual σ_i's are specified. Also assume that each scatterer's reflections are independent of the others; that is, there are no multiple bounces or reflections from one point reaching another and then reflected back to the radar. Then, if the group is at a large mean distance from the radar, all the scatterers may be assigned a common mean range value, r_o. The relative phase of each scatterer will depend on its distance, r_i, from a reference plane at distance r_o from the radar and all the r_i can be considered parallel (see Figure 1-1). For a scatterer placed at the reference plane a distance r_o from the radar, the magnitude of the received voltage will depend on the square root of the assigned radar cross section value, σ_i. The phase of the voltage will be proportional to the distance between the radar and the target, and will be denoted by $\phi_o + \phi_i$. Here ϕ_i is a function of r_i and ϕ_o a function of r_o. We may write

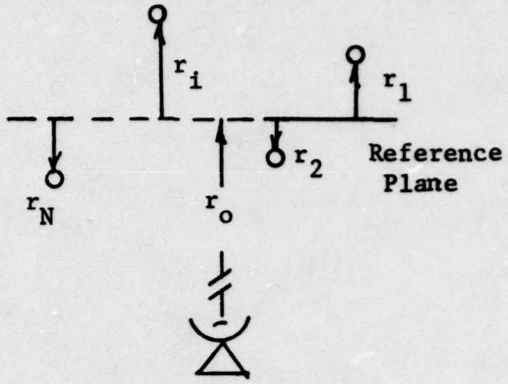

Figure 1-1

$$V_i' = k_p \sqrt{P_r}\, e^{-j\phi} = k_p k_c \sqrt{\sigma_i}\, e^{-j(\phi_o + \phi_i)} \tag{1-16}$$

where k_p is a constant with the dimensions of $(\text{ohms})^{1/2}$ and k_c is the constant relating P_r and σ in the radar range equation (1-15). Therefore,

$$k_c^2 = \frac{G_r G_t P_t \lambda^2}{(4\pi)^3 R^4} \tag{1-17}$$

It is also convenient to define a normalized voltage proportional to the square root of the radar cross section of the ith scatterer as

$$V_i = \frac{V_i' e^{j\phi_i}}{k_p k_c} = \sqrt{\sigma_i}\, e^{-j\phi_o} \tag{1-18}$$

The resultant total voltage from a sum of the returns is

$$V_T = \sqrt{\sigma_t}\, e^{-j\phi} = \sum_i \sqrt{\sigma_i}\, e^{-j(\phi_o + \phi_i)} = \sum_i V_i\, e^{-j\phi_i} \tag{1-19}$$

and the total cross section is $\sigma_T = V_T V_T^*$.

Each phase angle, $\phi_o + \phi_i$, can be determined by considering the time an electromagnetic wave takes to travel the reference distance, r_o plus r_i, to the ith point target and back again. Since the wave travels at the speed of light, c, the total time in free space is

$$t = \frac{2(r_o + r_i)}{c} \tag{1-20}$$

Relative to the total period, T_p, of the sine wave representing the transmitted wave, this time delay represents a phase shift given by (see Figure 1-2)

$$\phi_o + \phi_i = \frac{t}{T_p} 2\pi = \frac{2(r_o + r_i)}{cT_p} (2\pi) \qquad (1\text{-}21)$$

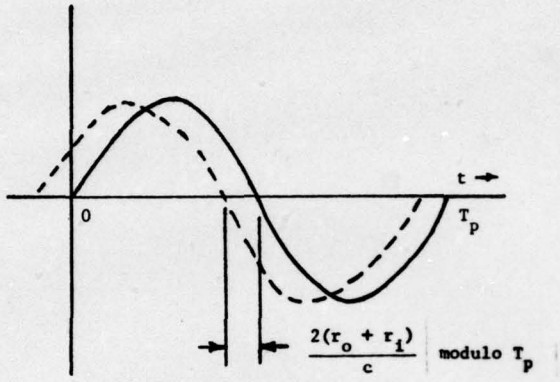

Figure 1-2

Here, $T_p = 1/f$ where f is the transmitted carrier frequency and the wavelength, λ, is defined by $\lambda = c/f$. The total phase shift to the target and back can be written as

$$\phi_o + \phi_i = (2\pi)(r_o + r_i)/(\lambda/2) \qquad (1\text{-}22)$$

In other words, the number of cycles of phase shift for the two-way travel is equal to the number of half wavelengths between the radar and the point scatterer. Defining the wave number as $k = 2\pi/\lambda$, (1-19) may be written as

$$V_T = \sum_i \sqrt{\sigma_i}\, e^{-j2k(r_o + r_i)} = \sum_i V_i\, e^{-j2kr_i} \qquad (1\text{-}23)$$

Equation (1-23) provides a useful starting point in the analysis of coherent cross section data. The average range to the target and the conversion from radar cross section to voltage in the antenna system have been incorporated into the complex voltage, V_i.

1.1d Practical Coherent Radar Data

This section is intended to review only briefly certain aspects of practical radar systems which are used to obtain the type of data to which the theoretical formulations of other sections apply. Other radar handbooks should be consulted for additional circuit or hardware details.

A coherent radar is one which is phase and frequency stable for a long enough period of time so that an accurate measurement of the phase between the transmitted and received signal can be made. In an amplifier-chain type of transmitter*, this is done using a low-level stable master local oscillator (MLO) that is allowed to run continuously. The oscillator acts essentially as a timing standard by which the return delay is measured to extract range information, accurate to within a small fraction of a wavelength, modulo $\lambda/2$. In a simple pulsed radar system, the transmitted signal is an amplified (and possibly multiplied and modulated) version of the oscillator signal, and the phase of the received signal is measured with respect to that of the continuously running oscillator. The oscillator must, therefore, maintain good phase stability in the system over the short time interval between transmission and reception. Phase variations in the oscillator system during the long time intervals between different pulse transmissions may have little effect on a set of short-duration relative phase measurements that can then be used to estimate target Doppler frequency shifts relative to the transmitted frequency. Thus, Doppler frequency phase measurements may readily be made stable enough to give very fine frequency resolution by integration of many pulses over long time intervals if the short term stability criterion is met.

Coherent systems transmitting more complex waveforms, like linear FM (Frequency Modulated) pulses, have these waveforms synchronized in a coherent sense with respect to an MLO. The signal processing is more complex, but coherent phase measurements can be made in a sense similar to that of simple pulsed systems.

---

*Oscillator type transmitters, such as those using magnetrons, may also be made to operate coherently with proper synchronization techniques, but are of lesser interest here.

Digital coherent data can be obtained in either of two different forms. They can be obtained as an amplitude and phase, or in the form of two different numbers termed I and Q. These numbers stand for the in-phase and quadrature phase components, respectively. Whether the data are obtained as amplitude and phase or as I and Q numbers, they have the carrier frequency removed. (The significance of removing the carrier frequency is discussed below and in Section 1.2b.) We say that the amplitude is a video signal which has been "shifted to baseband." The I and Q numbers can vary through positive and negative values and are called bipolar video signals.

If A(t) is the amplitude of the signal and θ is its phase, the I and Q numbers are given by

$$I = A\cos\theta, \qquad Q = A\sin\theta \tag{1-24}$$

Conversely, if the I and Q numbers are available, the amplitude and phase numbers are obtained from

$$A = \sqrt{I^2 + Q^2}, \qquad \theta = \tan^{-1} Q/I \tag{1-25}$$

The amplitude of the signal may be related directly to the radar cross section of a target as given by (1-15) and (1-16). However, when data are coherently processed on a digital computer, the complex number form of the data (I and Q) is generally used to do arithmetic operations such as complex addition, multiplication, and division. If the data are recorded on tape in the form of amplitude and phase numbers, the conversion using (1-24) must be performed before further computer processing.

When recording radar returns for analysis on a digital computer, I and Q signals may be practically recorded if the dynamic range of the data is small. Where the dynamic range is large, phase and logarithmic amplitude are usually used to minimize the number of required bits needed to form binary representions of the signals.

Amplitude data can be recorded using an envelope detector. A common example is a diode half-wave rectifier (a nonlinear device) followed by an RC low-pass filter, as illustrated in Figure 1-3.

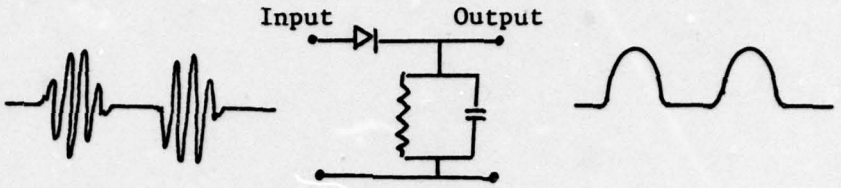

Figure 1-3

As the name indicates, the output of the detector represents the envelope of the incoming modulated carrier wave. The RC time constant is long enough to hold the incoming amplitude over many carrier cycles, yet short enough compared to the envelope functional variation to follow the envelope.

Phase data may be obtained using any one of a number of different types of phase detectors. Examples are a multiplier detector using a Field Effect Transistor (FET), a balanced diode detector, a coincidence phase detector, and a digital phase detector. All phase detectors are preceded by one or more limiter stages if the input signal is expected to vary widely in amplitude.

A pair of synchronous detectors may be operated in quadrature to obtain coherent data in "I and Q" form. The incoming radar signal is a real signal of the form $\sin(\omega t + \theta)$. The detectors are operated as described in Figure 1-4.

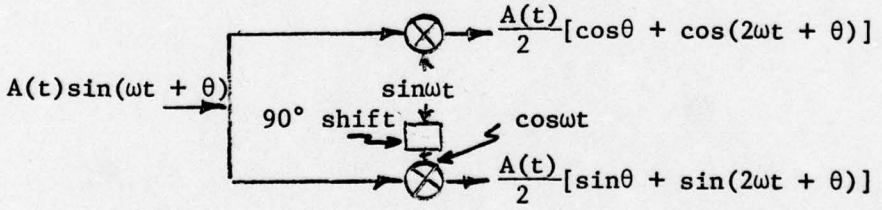

Figure 1-4

The outputs of the multipliers contain harmonics at twice the input frequency. These harmonics can be filtered out using a low pass filter. The output of the top multiplier is the in-phase, I, component of the signal and the output

of the bottom multiplier is the out-of-phase, Q, component. Note that multiplication of the signal by both $\sin\omega t$ and $\cos\omega t$ is necessary to obtain the complete complex signal. A further discussion of the means of obtaining coherent data may be found in Chapter 5 of Skolnik's "Radar Handbook" (McGraw-Hill, 1970).

1.2 TECHNIQUES FOR OBTAINING POINT SCATTERER DOPPLER RESPONSE FUNCTIONS

1.2a Doppler Frequency Shift Relationships

The Doppler effect is defined as a change in the observed frequency of a wave caused by motion of the source or of the observer. A familiar example for sound waves is the increase (decrease) in pitch of a train whistle as the train approaches (passes).

Consider an electromagnetic wave of the form $A(t)\sin\omega_o t$ transmitted from a radar and scattered from a target. The up and back time delay is $2T_D$. If the target is moving at radial velocity v parallel to the radar line-of-sight (RLOS), the distance R(t) to the target is given by

$$R(t) = R_o + vt \tag{1-26}$$

Then,

$$T_D = \frac{R(t - T_D)}{c} = R_o/c + v(t - T_D)/c \tag{1-27}$$

where $R(t - T_D)$ is R(t) evaluated at $t - T_D$. Equation (1-27) may be solved for T_D as

$$T_D = \frac{R_o + vt}{c + v} \tag{1-28}$$

so that (1-26), evaluated at $t - T_D$, becomes

$$R(t - T_D) = R_o + vt - v\,\frac{R_o + vt}{c + v} \tag{1-29}$$

The received signal is $A(t - 2T_D)\sin[\omega_o(t - 2T_D)]$. The argument of the sine term can be written as $[\omega_o(t - 2R(t - T_D)/c)]$ which, upon substitution from (1-28) and grouping of terms, yields

$$\omega_o(t - 2T_D) = \omega_o\left[\frac{c - v}{c + v}\, t - \frac{2R_o}{c + v}\right] \qquad (1\text{-}30)$$

Because $\omega_o = 2\pi f_o$, the apparent frequency is

$$f_a = f_o \frac{c - v}{c + v} \qquad (1\text{-}31)$$

The shift in frequency or Doppler shift, f_d, for a target with radial velocity v is then

$$f_d = f_o - f_o \frac{c - v}{c + v} = \frac{2vf_o}{c + v} \approx 2v/\lambda$$

$$= kv/\pi \qquad (1\text{-}32)$$

where the approximation $v << c$ has been made, and $k = \frac{2\pi}{\lambda} = \omega/c$.

It is important to remember that v is the radial component of velocity, that is, the component of velocity parallel to the direction of propagation. If a target has a velocity v' in an arbitrary direction, v is given by $v = v' \cos\gamma$ where γ in the angle between the velocity and direction of propagation (RLOS).

As a passing note, the preceding description of the Doppler effect is not the most exact. The general theory of relativity predicts a direction-indedendent effect between a moving source and receiver according to which the observed frequency will be lower than the source frequency regardless of the apparent motion of the target. For transverse relative motion, the one-way transverse Doppler effect is $f_d \sim f_o\sqrt{1 - v'^2/c^2}$ where f_o is the true source frequency.

It is useful to relate the Doppler frequency shift, f_d, to the phase of a point scatterer as given by (1-22) or (1-23). The time derivative of the phase ϕ_i is given by

$$\frac{d\phi_i}{dt} = \frac{d}{dt}(2kr_i) = 2k\dot{r}_i = (2\pi)\, 2v_i/\lambda = 2\pi f_d = \omega_d \qquad (1\text{-}33)$$

where $v_i = \dot{r}_i$.

1.2b Fourier Transform Techniques for Resolving Points

Consider a target consisting of a number of point scatterers. Each point scatterer is moving at some velocity, $v_i = \dot{r}_i$, with respect to the radar. Different points may have different velocities. The points may be resolved as separated targets in at least three ways with a radar system. If the radar beam is narrow enough, the points may lie in different beam positions, so that scanning the target region may resolve the points in angle. If the radar pulse is short enough, the points may be distinguished on the basis of their different range positions. A third method, which is the one in which we are presently most interested, resolves the points on the basis of their radial velocity differences.

In this third case, the radar beamwidth and pulsewidth both may be broad enough to encompass all the targets, but the radar data must be coherent. The coherent signals may then be passed through a bank of Doppler filters arranged in a contiguous band of frequencies to be searched, each filter having a narrow enough bandwidth to obtain a desired resolution of equivalent radial velocity. Detection of significant signal levels at the filter outputs would allow a determination of the number of resolved reflecting points and their radial velocities. With digital coherent data, Fourier transform techniques may be used to form the equivalent of a Doppler filter bank. A review of classical Fourier transform theory as related to resolving Doppler frequency shifts follows.

The Fourier transform relates an arbitrary time function, $f(t)$, to its radian frequency components, ω, by use of the transform pair:

$$f(t) = \frac{1}{2\pi} \int_{-\infty}^{\infty} g(\omega)\, e^{j\omega t}\, d\omega \qquad (1\text{-}34)$$

$$g(\omega) = \int_{-\infty}^{\infty} f(t)\, e^{-j\omega t}\, dt \qquad (1\text{-}35)$$

The function $f(t)$ may be real or complex. In general, $g(\omega)$ is complex and a plot of $|g(\omega)|$ versus ω shows the relative frequency distribution of $f(t)$. Equation (1-35) is usually called the direct transform and (1-34) the inverse

transform. The function f(t) is in the "time domain", g(ω) is in the "frequency domain" and defines the spectrum of f(t). Note that f(t) is a continuous function of time, although the radar signal may only be sampled at finite increments in time. For now, let us assume the data are continuous. The discrete sampling problem will be treated in the next subsection.

Let us now compute the Fourier transform or spectrum of the signal from a point scatterer moving with radial velocity v. It will be informative to obtain the response considering: (1) the complex signal at baseband (carrier frequency removed), and (2) a real radar signal before it is shifted to baseband. The following identities are useful in computing these transforms:

$$\cos ax = \frac{e^{jax} + e^{-jax}}{2} \tag{1-36}$$

$$\sin ax = \frac{e^{jax} - e^{-jax}}{2j} \tag{1-37}$$

$$\int_0^T e^{-jax}\, dx = T\, e^{-jaT/2}\ \frac{\sin a\, T/2}{a\, T/2} \tag{1-38}$$

Using the forms of Section 1.1c and 1.2a, the complex time signal from a moving point target may be written as

$$v_1(t) = \sqrt{\sigma}\ e^{-j2k(R_o + vt)} \tag{1-39}$$

Substitution in (1-35) and integrating over a period of time, T, results in the spectrum

$$g_1(\omega) = \sqrt{\sigma}\ e^{-j[2kR_o + (\omega + \omega_d)T/2]}\, T\, \frac{\sin(\omega + \omega_d)T/2}{(\omega + \omega_d)T/2} \tag{1-40}$$

where $\omega_d = 2\pi f_d = 2kv$. The magnitude of $g_1(\omega)$ is sketched in Figure 1-5. It consists of a $|\sin x/x|$ function whose peak is at $\omega_d = 2\pi f_d$.

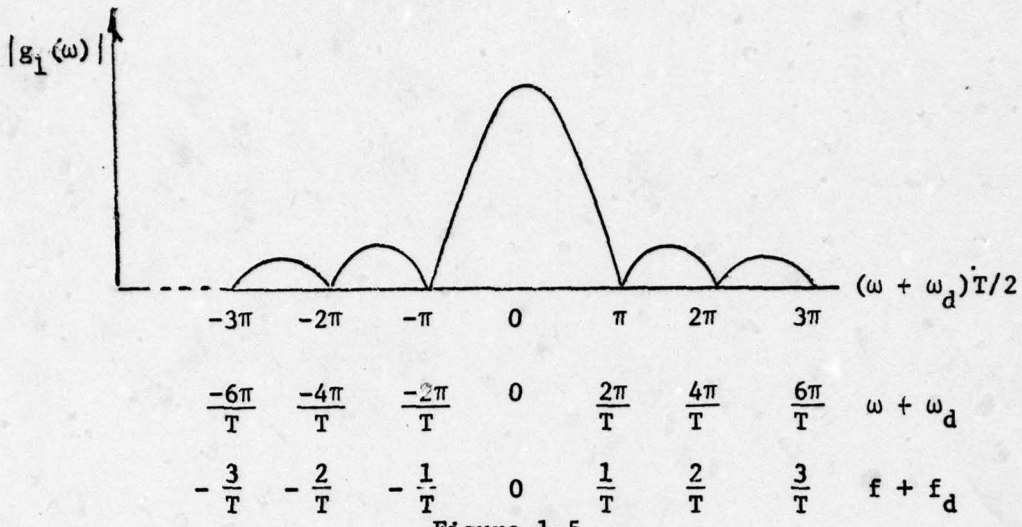

Figure 1-5

The classical sinx/x function peaks at x = 0 with a value of 1. Its first sidelobe has a value of 0.2122 (or is down 20 $\log_{10}(0.2122)$ = -13.45 dB from the peak). It is seen that the most important part of the frequency distribution lies in the range $0 \leq |(\omega + \omega_d)| \leq \frac{2\pi}{T}$, which defines the null-to-null width of the "main lobe" response as $\Delta\omega = \frac{4\pi}{T}$. This width increases as the duration, T, of the integration span is made shorter.

The real signal from a point scatterer before it is shifted to baseband, using (1-3), is

$$v_2(t) = \sqrt{\sigma}\, \mathrm{Re}(e^{-j2k(R_o + vt)}\, e^{j\omega_o t}) \qquad (1\text{-}41)$$
$$= \sqrt{\sigma}\cos[(\omega_o - \omega_d)t - 2kR_o]$$

where ω_o is the radian carrier frequency. Substituting (1-41) in (1-35) and integrating over a period of time, T, results in

$$g_2(\omega) = e^{-j[2kR_o + (\omega - \omega_o + \omega_d)T/2]}\sqrt{\sigma}\,(T/2)\,\frac{\sin[\omega - \omega_o + \omega_d)T/2]}{(\omega - \omega_o + \omega_d)T/2} \qquad (1\text{-}42)$$
$$+ e^{j[2kR_o - (\omega + \omega_o - \omega_d)T/2]}\sqrt{\sigma}\,(T/2)\,\frac{\sin[\omega + \omega_o - \omega_d)T/2]}{(\omega + \omega_o - \omega_d)T/2}$$

The magnitude of this frequency spectrum, $|g_2(\omega)|$, is sketched in Figure 1-6. It consists of two |sin x/x| functions whose peaks are at $\omega = \pm(\omega_o - \omega_d)$.

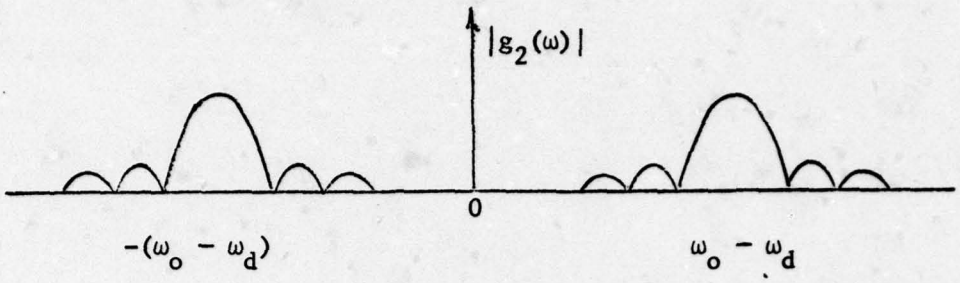

Figure 1-6

If the real radar signal from a point scatterer is sampled at a high enough rate, a double sided transform will be obtained as sketched in Figure 1-6. The sampling rate will be very high because of the presence of the carrier frequency, ω_o. Removing the carrier (shifting to baseband) will reduce the sampling requirement, but the two sides of the spectrum function can then overlap in an ambiguous manner, as might be sensed in shifting the two (sin x/x) functions in Figure 1-6 towards the origin. Having a number of points with positive and negative Doppler shifts will make the baseband frequency response function totally confusing. The problem can be resolved by adding a basebanded version of the signal shifted 90° to form the complex I and Q pair, as discussed in Section 1.1d. Then transforming the sum of I and Q will give the one-sided spectrum sketched in Figure 1-5 for a single point, and the sampling rate requirement will only be dependent on the frequency spread of a set of points. Use of direct amplitude and phase measurements to form the complex pair will have similar effects.

It should be noted in passing that in general, if a function is real, its Fourier transform has the property that $g(-\omega) = g^*(\omega)$. Hence, a plot of the magnitude of the spectrum has mirror symmetry about $\omega = 0$, that is, $|g(-\omega)| = |g(\omega)|$ as is shown in Figure 1-7.

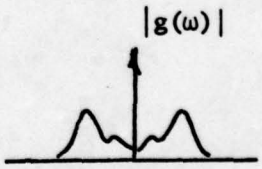

Figure 1-7

Equations (1-40) and (1-42) and Figures 1-5 and 1-6 illustrate that point scatterers

may be resolved and located on the basis of their radial velocities. That is, the radian frequency, ω_d, at which the peak of the sin x/x function occurs is determined by the target velocity. If more than one point scatterer is present each will have a frequency spectrum given by a sin x/x function. Equal amplitude scatterers may be separated if widths of mainlobes are sufficient, and resolution values are usually based on mainlobe separations of equal amplitude scatterers. However, in order to resolve scattering points with different amplitudes, their radial velocities must be separated enough so that the main peak of a low amplitude point is not overwhelmed by the sidelobes of a high amplitude point. Weighting functions are used to alleviate this sidelobe problem, as described in the following discussion.

1.2c Resolution Relationships with Weighting Function for Sidelobe Reduction

In resolving scatterers when more than one is present, it is helpful to include a weighting function which modifies the Fourier transform of the point target so that the spectrum of each target has lower sidelobes than that of the sin x/x function. In this way, the velocity of each target may be more clearly defined. This concept is commonly used in antenna array design (as well as in other forms of signal processing) to achieve low sidelobes. Common weighting functions for antenna purposes are Chebyshev and Taylor weights. In coherent signal processing a commonly used weighting function is the Hamming weight defined as

$$\begin{aligned} W_H(t - T/2) &= 0.54 + 0.46 \cos[2\pi(t - T/2)/T] \\ &= 0.54 - 0.46 \cos(2\pi\, t/T) \end{aligned} \qquad (1\text{-}43)$$

The Fourier transform of the complex signal from a point scatterer is now

$$g_H(\omega) = \int_o^T W_H(t - T/2)\, e^{-j2k[R_o + vt]}\, e^{-j\omega t}\, dt \qquad (1\text{-}44)$$

This is most easily evaluated by expanding $\cos(2\pi t/T)$ in terms of the exponential function given by (1-36) and then performing the integration using (1-38). The result is

$$g_H(\omega) = T\, e^{-j[2kR_o + (\omega + \omega_d)T/2]} \left[0.54 \frac{\sin[(\omega + \omega_d)T/2]}{[(\omega + \omega_d)T/2]} \right.$$

$$\left. + 0.23 \frac{\sin[(\omega + \omega_d)T/2 - \pi]}{[(\omega + \omega_d)T/2 - \pi]} + 0.23 \frac{\sin[\pi + (\omega + \omega_d)T/2}{[\pi + (\omega + \omega_d)T/2]} \right] \quad (1\text{-}45)$$

Thus, the spectrum of a Hamming weighted point target is composed of three sin x/x functions centered at $\omega = -\omega_d$, $-\omega_d - 2\pi/T$, $-\omega_d + 2\pi/T$. The resultant spectrum is compared with a sin x/x spectrum in Figure 1-8.

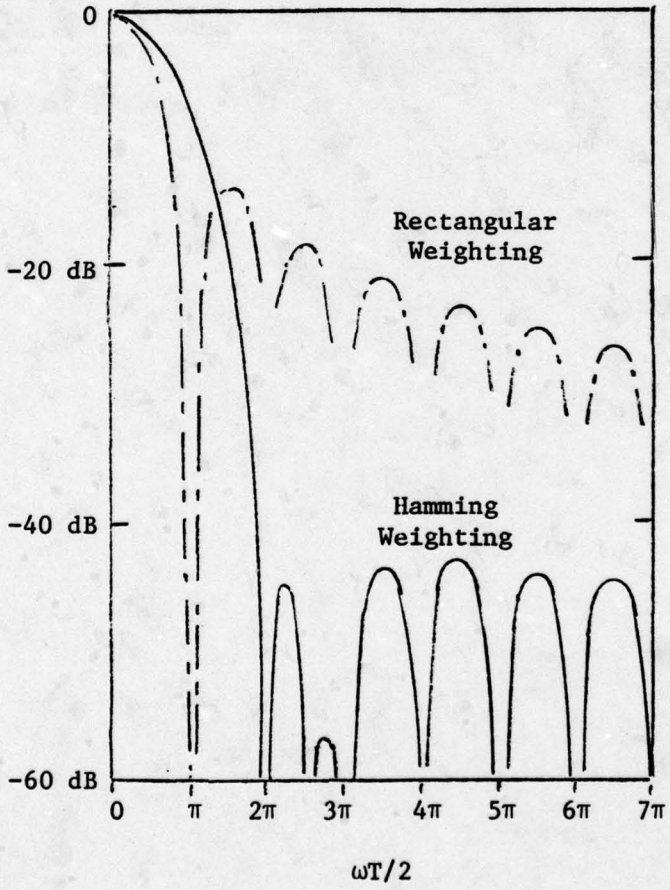

Figure 1-8

The mainlobe of the Hamming weighted signal has a null-to-null width twice as wide as the sin x/x response. This broadening can be considered the price paid in order to obtain the -42.8 dB peak sidelobe. The first null of the sin x/x response and the Hamming response coincide. All other peaks and nulls of the Hamming response do not coincide with those of the sin x/x responses.

In summary, using a weighting function such as a Hamming weight reduces the sidelobes of a moving point scatterer response. They, therefore, less significantly interfere with the lower responses of a smaller target moving at a different velocity. However, the weighted function resolution is not as good for equal amplitude scatterers due to the broadening of the main response. The Hamming weighted mainlobe width at the 3 dB (half-power) points is approximately 1.5 times that of the sin x/x response.

1.2d Effects of Using Sampled Data

The digital output from the circuitry of a narrowband radar is usually a time function which is sampled at fixed intervals in time, Δt, and recorded for subsequent analysis. The result of sampling a signal v(t) is illustrated in Figure 1-9. The sampled signal is denoted $v_s(t)$.

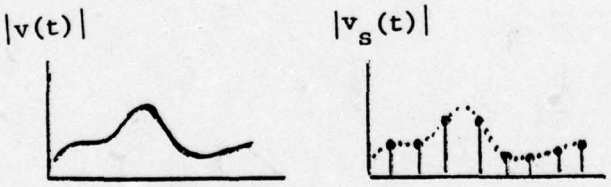

Figure 1-9

The sampling process can be conveniently explained if the concept of an impulse function is used. An impulse function, $\delta(t)$, can sample a signal instantaneously (in zero time). It is the limit of a pulse of length, a, and height 1/a. As the length, a, is shrunk to 0, the height, 1/a, is allowed to increase to infinity so that its area remains unity. This is illustrated in

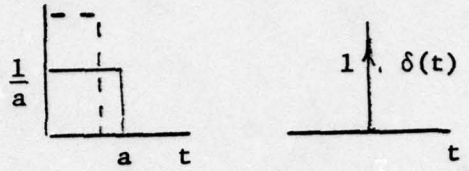

Figure 1-10

Figure 1-10. The impulse function, therefore, is defined to have infinite amplitude, zero duration, and finite area. A shifted unit impulse that occurs at $t = T$ can be represented by the function $\delta(t - T)$. The total area under the curve is unity, so that

$$\int_{-\infty}^{\infty} \delta(t - T)dt = 1 \qquad (1\text{-}46)$$

The integral has the same value for any limits which bound $t = T$. If $f(t)$ is a continuous function of t, then the product $f(t)\ \delta(t - T)$ will be zero everywhere except at $t = T$, where there will be an impulse function having strength equal to $f(T)$. This is illustrated in Figure 1-11.

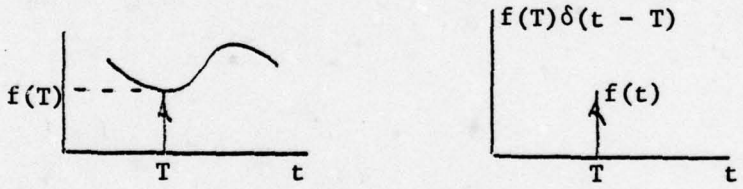

Figure 1-11

In view of (1-46) we have

$$\int_{-\infty}^{\infty} f(t)\ \delta(t - T)\ dt = f(T) \qquad (1\text{-}47)$$

Again, the integral has the same value for any limits of time which bound $t = T$.

We might also define the Fourier transform of an impulse function. From (1-35) we have

$$g_\delta(\omega) = \int_{-\infty}^{\infty} \delta(t - T)\, e^{-j\omega t}\, dt = 1e^{-j\omega T} \tag{1-48}$$

The spectrum of an impulse is therefore a constant. The relative frequency distribution of $\delta(t - T)$ is flat and the energy contained in an impulse function is uniformly distributed over all frequencies. This should be compared to the spectrum of a finite pulse length, which contains an infinite number of frequency components but whose amplitude distribution is of the sin x/x form.

We may write a sampled signal, $v_s(t)$, as the product of the continuous signal and a sum of impulses occurring at times $n\Delta t$ apart. That is,

$$v_s(t) = \sum_{n=0}^{\infty} v(t)\, \delta(t - n\Delta t) = \sum_{n=0}^{\infty} v(n\Delta t)\, \delta(t - n\Delta t) \tag{1-49}$$

which was illusrated in Figure 1-9.

In order to obtain the spectrum of the sampled signal, $v_s(t)$, we will use an identity which can be proven using the complex form of a Fourier series. The identity states that

$$\sum_{n=-\infty}^{\infty} \delta(t - n\Delta t) = \sum_{k=-\infty}^{\infty} e^{j2\pi kt/\Delta t} = \sum_{k=-\infty}^{\infty} e^{j\omega_s kt} \tag{1-50}$$

where

$$\omega_s = 2\pi/\Delta t \tag{1-51}$$

is the sampling frequency. Therefore,

$$v_s(t) = \sum_{k=-\infty}^{\infty} v(t)\, e^{j\omega_s kt} \tag{1-52}$$

The Fourier transform of $v_s(t)$ is then

$$V_s(\omega) = \sum_{k=-\infty}^{\infty} \int_{-\infty}^{\infty} v(t)\, e^{-j(\omega - k\omega_s)t}\, dt$$

$$= \sum_{k=-\infty}^{\infty} g(\omega - k\omega_s) \qquad (1\text{-}53)$$

Sampling thus produces an infinite number of spectra, each a replica in shape of the original signal spectrum. The spectra are separated by ω_s, the sampling frequency. A plot of the spectrum of sampled data is called a periodogram because of the repeating nature of the spectrum.

The sampled real signal representation of two unequal amplitude moving point scatterers shifted to baseband might have a spectrum as sketched in Figure 1-12 for k = 0, $\pm$ 1. In the plot both scatterers have a positive Doppler frequency shift.

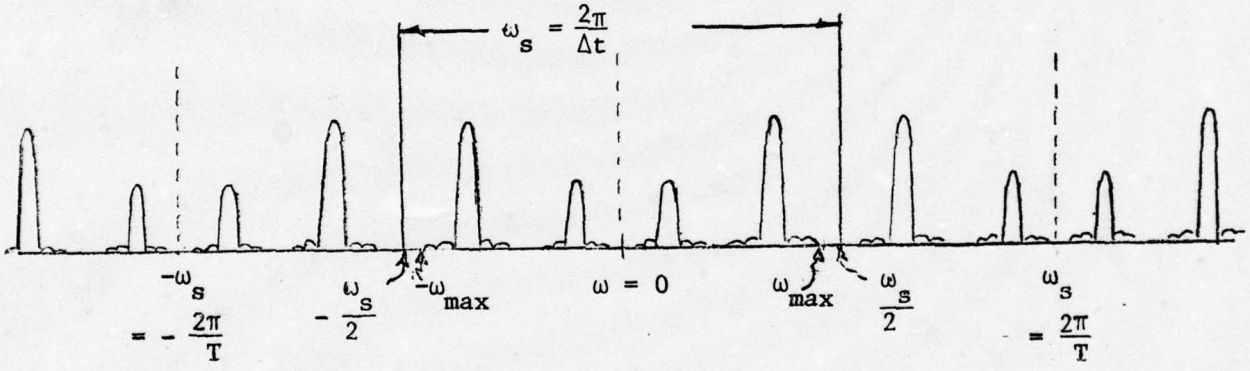

Figure 1-12

The central spectrum (k = 0) can be processed without undue concern provided that the input signal is band limited with negligible spectral components beyond ω_{max} where ω_{max} is the highest significant frequency component in the original time signal. If the signal is not sampled fast enough, ω_s and all its harmonics start closing in on one another. The spectral components in Figure 1-12 eventually overlap and merge. The components $g(\omega \pm \omega_s)$ centered about $\mp\, \omega_s$ merge with the unshifted $g(\omega)$ term centered at the origin. It is then

impossible to separate out $g(\omega)$ and, hence, $v(t)$ from $v_s(t)$. The limiting frequency at which $g(\omega)$ and $g(\omega - \omega_s)$ merge is, from Figure 1-12, given by $\omega_s - \omega_{max} = \omega_{max}$ so that for unambiguous reconstruction of a real time signal

$$\omega_s \geq 2\,\omega_{max} \tag{1-54}$$

It is because of this merging of the spectra that the sampling frequency, ω_s, is sometimes called the folding or aliasing frequency.

The positive half of the central spectrum of Figure 1-12 resolves the Doppler shift of each scatterer unambiguously because both points have well separated positive Doppler frequency shifts. If one scatterer had a negative Doppler frequency shift, the mirror image property of the spectrum of a real signal would make it more difficult to identify the point scatterers unambiguously. In this case the problems in resolving the targets stem from the form of the total signal even before it is sampled.

The periodogram of the sampled complex signal from the same two point targets is shown in Figure 1-13

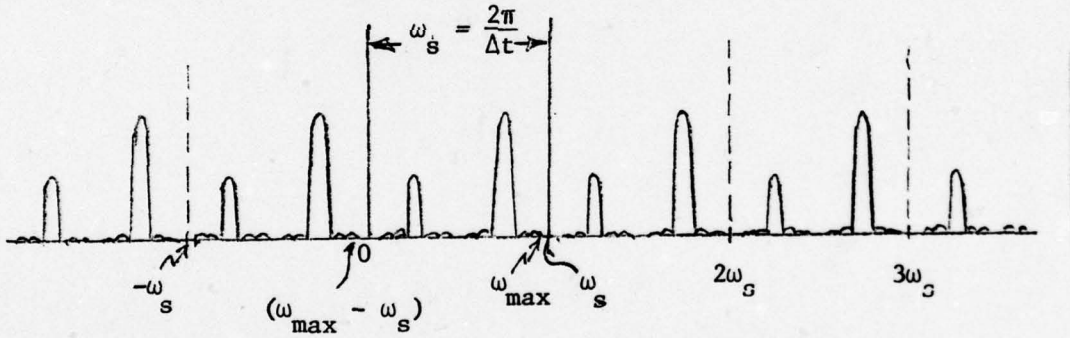

Figure 1-13

In this case, each sample in time gives one complex number which is equivalent to two samples of the highest frequency component of the time signal, so that for unambiguous reconstruction of a complex time signal $\omega_s \geq \omega_{max}$.

In a narrowband radar, each pulse transmitted and scattered from a target is converted to a complex number (I and Q or amplitude and phase). The same concept holds true for a wideband (short pulse) radar. In this case, the

target is divided up into range cells with one or more possible point targets in each range cell. Each returned pulse is represented by one complex number per range cell. The rate ($\omega_s/2\pi$) at which data are obtained (sampled) is equal to the pulse repetition frequency (PRF). An undersampled signal, such that $\omega_s < \omega_{max}$, results in overlap of the spectra and is said to be "PRF limited".

In summary, if complex time functions are sampled at equal spacings, Δt seconds apart, the unambiguous Fourier spectral response interval will be equal to $\frac{1}{\Delta t}$ Hz or $\frac{2\pi}{\Delta t}$ radians/seconds. If the functions are real and therefore have two-sided spectral responses, there is an equivalent folding effect which limits the unambiguous frequency interval to one-half the complex function values. If the spectra extend significantly beyond these ambiguity intervals, unresolvably ambiguous results can occur. A time function must be sampled at twice the rate given by the maximum frequency component (in Hz) of the true spectral response function for the continuous function to be exactly reconstructed from the sampled data (Shannon's theorem). If this maximum frequency component is f_{max}, the required sampling increment is $\Delta t = 1/f_{max}$ when the function is complex, since two function samples are given at each time sampling point. For real functions, the sampling time increment is half the complex function value. This is equivalent to saying that at least two samples per sinusoidal period are needed to reconstruct a real sinusoid in an unambiguous or "unaliased" manner.

1.2e THE FAST FOURIER TRANSFORM

Much of the work in coherent signal processing involves taking the Fourier transform of data which has been stored in discrete form on magnetic tape or in a digital computer. Therefore, it is especially useful to have a quick, efficient method for finding the spectrum of a signal stored as discrete data. The technique for doing this is called the Fast Fourier transform (FFT). Various versions of the FFT are available in subroutine form for most general-purpose digital computers. The mechanics of these algorithms will not be discussed here. However, there are certain limitations in these algorithms which might be better understood from a brief review of the numerical integrations that are represented.

The continuous integral of the Fourier transform given by (1-35) can be approximated by various numerical integration algorithms and spectral components may be calculated for all values of frequency. For equispaced data samples, a special form of numerical integration, sometimes called a discrete Fourier transform (DFT) leads to the FFT under certain restrictions. The DFT is presented in the following discussion.

In the case of sampled data, taken over a time interval, T, the continuous Fourier transform pair given by (1-34) and (1-35) can be rewritten in a series summation form by first making several substitutions. Select N data samples at times $t_m = m\Delta t$ where $\Delta t = T/N$ and let $f_n = n\Delta f$ where $\Delta f = 1/T$. Then using $\omega_s = 2\pi f_n$, (1-35) can be approximated by the summation which may be called a DFT

$$g(n) = \Delta t \sum_{m=0}^{N-1} f(m)\, e^{-j2\pi(nm)/N} \qquad (1\text{-}55)$$

$$n = 0, \pm 1, \ldots, \pm N/2$$

or

$$n = 0\ 1, \ldots, N - 1$$

Equation (1-55) gives output frequencies evaluated at evenly spaced frequency increments of Δf. This special form then allows an inverse discrete transform to reconstruct the f(m) set from the g(n) set according to

$$f(m) = \Delta f \sum_{n} g(n)\, e^{j2\pi(nm)/N} \qquad (1\text{-}56)$$

$$\text{for } m = 0, 1, \ldots, N - 1$$

where the summation is either from n = 0 to N - 1 or from n = -N/2 to N/2, if N is even. There are only N distinct values of g(n) computable by (1-55). If g(n) are calculated for n outside either range of values defined by (1-55), they will be repeated values of those within the series. We may think of (1-55) in two different ways. First, as a formula yielding N numbers which are samples of a frequency spectrum. Second, as a formula yielding a periodic sequence of numbers with period N.

In general, the evaluation of (1-55) or (1-56) requires N^2 multiplications and additions. The FFT is a method by which these multiplications and additions may be drastically reduced. Specifically, if the time function

consists of $N = 2^n$ samples then about $2nN = 2N \log_2 N$ arithmetic operations will be required to evaluate (1-55) or (1-56). For example, an $N = 2^{10}$ point transform can be computed with the FFT 100 times faster than with a direct approach. The output frequencies of the FFT algorithm are evenly spaced and cannot be picked at random, independently of the input data time sampling. This is the price paid for the rapid computation time.

With this background, consider the Fast Fourier transform of a point scatterer moving at a constant velocity v. The Fourier transform of its complex signal is given by (1-40) and its continuous spectrum is plotted in Figure 1-5. Assume the complex signal is sampled rapidly enough so that there is no overlap of the spectra. If the complex signal is sampled at N points over a time period, T, the time beween samples is $\Delta t = T/N$ and the output frequencies will be in steps of

$$\Delta\omega = 2\pi\Delta f = 2\pi/T \tag{1-57}$$

This is the same as the main lobe peak-to-null width of the $|\sin x/x|$ spectrum of Figure 1-5. We conclude that N samples of data from a moving point target will result in, at best, only two frequency samples within the mainlobe of the sin x/x spectrum of the scatterer. If an output frequency of the FFT is at the peak of the mainlobe, the other output frequency will be in a null of the mainlobe. Thus the mainlobe of the sin x/x function will be poorly defined. This is illustrated in Figure 1-14.

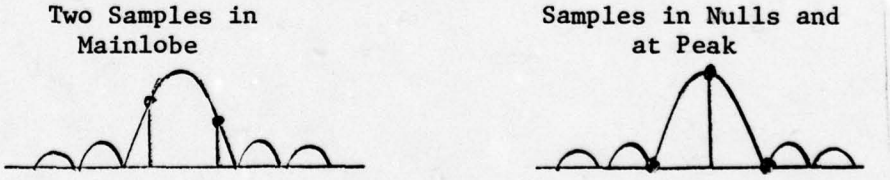

Figure 1-14

If we sample at a faster rate over the time, T, so that N is larger and Δt is smaller, we increase the highest output frequency given by

$$f_{max} = N/T = 1/\Delta t \tag{1-58}$$

but the number of samples in the mainlobe remain the same, independent of the number of actual samples of data used. A way around this problem is to add zeros to the string of input data so that the size of the N point transform is increased along with the apparent time span, T', of the data. The highest output frequency remains the same at $f_{max} = 1/\Delta t$, but more frequencies are in the output at a closer spacing $\Delta f = 1/T'$. The adding of zeros interpolates the output frequency points more closely. It does not mean we are Fourier transforming a longer time span of data. The output sin x/x distribution still has a mainlobe peak to null width of

$$\Delta\omega_{pn} = 2\pi/T \tag{1-59}$$

If as many zeros are added as there are real data points, T' = 2T so that output frequencies are in steps of $\Delta\omega = 2\pi\Delta f = \pi/T$. This improves the definition of the sin x/x mainlobe as shown in Figure 1-15. Now as many as four frequency

Increased Samples from FFT Interpolations

Figure 1-15

samples can occur within the null-to-null mainlobe width. In practical processing, adequate definition is usually obtained if the string of numbers put into the FFT contains at least one third zeros. An alternative explanation of the adding of zeros to an FFT is presented in Section 1.3b.

In summary, there are trade-offs to be made when using an FFT which depend on the size of transform that is practical, the closeness of the sampling of the data, the highest frequency component of interest, and the desired detail in the spectral function. If the number of input data samples is not a power of

two, then zeros must be added to the set to extend the series to the nearest power of two if all the input data are to be included in the transformation. If more output sample points in the frequency function are needed to better define the function, such as to better locate the peak of a mainlobe, then an interpolation can be effected by adding even more zeros to the original input data set. The number of output samples across an unambiguous spectral window will increase directly with the size of the total input data series with zeros added. The price for the interpolations will be increased computer operations.

Having too short an unambiguous frequency response interval because the time sampling increment is too long can be one problem in the FFT processing which might not be solvable once a radar PRF is fixed. An opposite problem, more readily solvable, could be having too fine a time sampling interval, in which case transforming all of the data in a series will give output samples over many frequencies at which the actual target spectrum does not practically exist. One solution would simply be to omit data samples until the sampling increment matches the desired frequency spectrum. If the signals are weak, the signal-to-noise ratio could be improved by averaging the groups of samples (sometimes called "presumming") instead of just omitting samples and then transforming the averaged data. The unambiguous FFT frequency interval is then determined by the time interval between the averaged groups.

1.3 CROSS RANGE FOR SIMPLY ROTATING POINTS

1.3a Angle Parameter Signal Representation for a Rotating Target Approximated by Points

The point target idealization is convenient in studying various processing methods producing one- or two-dimensional images of a target. The background for obtaining one-dimensional images based on point target Doppler responses for simplified motion conditions is the main concern in this section. Two-dimensional imaging is deferred to Section 1.4, although the Doppler response results of this section apply also to certain two-dimensional cases. Doppler frequency variations under more complex motion conditions are discussed in Section 3.

If there are Doppler differences between the scatterers, signal returns may be processed to resolve points in Doppler as discussed in Section 1.2. Knowledge of rotation rate and the assumption of approximately linear motion of points during a processing interval may allow the Doppler scale to be normalized to a cross-range dimension to give directly a measure of the target extent in a dimension orthogonal to the radar incidence direction. Images obtained under the assumption of linear motion of points during a processing interval will be called "first-order" images.

Let a target be a collection of rigidly connected points rotating about a fixed axis at a constant velocity, Ω. Each point, identified by the index i, has an amplitude, $v_i(t)$, a radial distance from the center of rotation, L_i, and an initial angular position, θ_{oi}, of the radial arm relative to the y-axis. Radar incidence direction defined by unit vector $\vec{r}$ is parallel to the y-axis with far-field plane wave conditions prevailing. The variables are illustrated in Figure 1-16. The rotation axis is parallel to the z-axis, which is perpendicular to the x-y plane. The points can extend in the z direction, maintaining the radial distance, L_i.

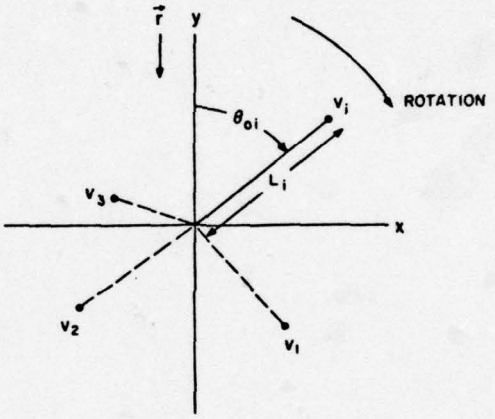

Figure 1-16

To simplify the analysis, a single point will be considered, as shown in the sketches of Figure 1-17 in which the parameters, θ_{oi} and L_i, can be considered unknown before signals are received.

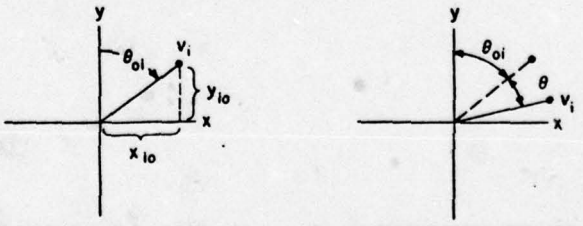

Figure 1-17

The point rotates through an angle, θ, at velocity Ω such that $\theta = \Omega t$. The position of this point in the slant-range direction parallel to the RLOS, referenced to the center of the x-y system defining the center of rotation, is

$$y_i = L_i \cos(\theta_{oi} + \Omega t) \tag{1-60}$$

and the cross-range position is

$$x_i = L_i \sin(\theta_{oi} + \Omega t) \tag{1-61}$$

Consider a simple transmitted pulse, A(y), modulating a carrier with wave number $k = 2\pi/\lambda$. The response from the target is a delayed pulse, $A(y - y_i)$, with its phase described by $2ky_i$. A simple pulse shape (like a Gaussian) for $A(y - y_i)$ locates the point in slant range by its peak position at $y = y_i$.

The complex signal from the ith point target rotating with angular velocity Ω is now given by

$$V_i = \sqrt{\sigma_i}\, e^{j2ky_i} = \sqrt{\sigma_i}\, e^{j2k\, L_i \cos(\theta_{oi} + \Omega t)} \tag{1-62}$$

(A real form of this signal with a carrier, ω_o, would be

$$V_r(t) = \mathrm{Re}(V_i\, e^{j\omega_o t}) \tag{1-63}$$

although this form will not be used in the analysis.) For short signal processing times such that the angle, θ, through which the point target rotates is small, we can expand y_i as

$$\begin{aligned} y_i &= L_i[\cos\theta_{oi} \cos \Omega t - \sin\theta_{oi} \sin \Omega t] \\ &= y_{io} \cos \Omega t - x_{io} \sin \Omega t \\ &\approx y_{io} - x_{io}(\Omega t) \end{aligned} \tag{1-64}$$

where the initial positions are given by x_{io} and y_{io}, and the approximations $\cos\theta \approx 1$ and $\sin\theta \approx \theta$ have been made. With these approximations, y_{io} becomes a constant and the second term is linear in Ωt.

The complex signal from a collection of point targets, all rotating at angular rate Ω, is now given by

$$V(t) \approx \sum A_i(y - y_i)e^{j2k(y_{io} - x_{io}(\Omega t))} \tag{1-65}$$

If the pulse envelope, $A(y - y_i)$, is considered to vary a negligible amount during a processing interval, $\Delta\theta_T$, the signal may be Fourier transformed along constant slant-range contours. Then, if only the points in one slant range resolution cell are considered, $A_i(y - y_i) \approx \sqrt{\sigma_i}$, and the index i may span only the points in that cell. With these single cell assumptions, substituting (1-65) in (1-34) gives

$$g_r(\omega) = \sum \sqrt{\sigma_i} Te^{j\left[2ky_{io} - (\omega + 2kx_{io}\Omega)\, T/2\right]} \left[\frac{\sin(\omega + 2kx_{io}\Omega)\, T/2}{(\omega + 2kx_{io})\, T/2}\right] \tag{1-66}$$

One term of (1-66) is the same as (1-40) for a linearly moving point, with cross range and Doppler frequency related by $\omega_d = 2kx_{io}\Omega$. This is not surprising because v in (1-39) is the time rate of change of the target along the direction of propagation (RLOS) which is given by

$$v = \dot{y}_i = x_{io}\,\Omega \tag{1-67}$$

We can also relate the cross range coordinate, x, to the rotation rate, Ω, as follows. For a point target as shown in Figure 1-18, we have $\Omega L = v'$ or $\Omega x = v$, and from (1-32), $v = f_d(\lambda/2)$ where $\omega_d = 2\pi f_d$. Thus,

$$x = \frac{v}{\Omega} = f_d\left(\frac{\lambda/2}{\Omega}\right) \tag{1-68}$$

This equation provides a means of scaling between the cross range position, x, and the Doppler frequency shift, f_d, of a target rotating at a rate, Ω.

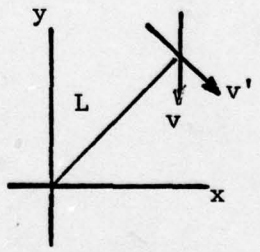

Figure 1-18

We could just as well have Fourier transformed with respect to angle rather than with respect to time. We can think of the variable t in (1-34) and (1-35) as representing the angle θ. We can then directly transform the signal

from a point target by writing θ instead of t and choosing $\omega = 2kx$. The integrand of (1-35) will peak at that value of x corresponding to the position of the point target. We may write

$$g_r(x) = \int_{-\Delta\theta_T/2}^{\Delta\theta_T/2} V(\theta)\, e^{-j2kx\theta}\, d\theta \qquad (1\text{-}69)$$

We now see that the relative aspect angle change during the integration span, not the integration time, is the parameter of interest. It does not matter how the aspect change is accomplished. Although much of the present section discussed a scatterer composed of rigidly connected point targets rotating at an angular rate Ω, any conditions which provide a relative aspect change between the rigidly connected points will suffice for (1-69) to hold.

This section has discussed the ideal condition where the RLOS is orthogonal to the axis of rotation of the point targets. The more general case where this is not necessarily true will be discussed in Sections 3 and 4.

1.3b First-Order Cross Range Resolution and Ambiguity *Relationships in Angular Units*

Let us examine more closely the details of the Fourier transform with respect to angle, θ, and cross-range coordinate, x. The equivalent of (1-55) and (1-56) become

$$g(n) = \Delta\theta_s \sum_{m=0}^{N-1} f(m)\, e^{-j2\pi(nm)/N} \qquad (1\text{-}70)$$

for $n = 0, \pm 1, \ldots, \pm N/2$

or $n = 0, 1, \ldots, N-1$

and

$$f(m) = \Delta x_s \sum_{n} g(n)\, e^{j2\pi(nm)/N} \qquad (1\text{-}72)$$

$m = 0, 1, \ldots, N-1$

n = either series in (1-70)

Let us now consider the implications of (1-70) and (1-71) where instead of t_m we have $\theta_m = m\Delta\theta_s$. The tranform uses a total of N points where $N = N_T + N_o$. Here, N_T is the number of actual data points associated with the integration span $\Delta\theta_T$ and N_o is the number of zeros added to the array to be transformed. In this case, $\Delta\theta_s = \Delta\theta_T/N_T$ and $x_n = n\Delta x_s$. Thus, the exponent in (1-69) becomes $2kn\Delta x_s m\Delta\theta_s$. Equating this to $2\pi nm/N$, we find the output samples from the FFT will be spaced in cross range units according to

$$\Delta x_s = (\lambda/2)/(N\Delta\theta_s) \tag{1-72}$$

We can write $N\Delta\theta_s = \Delta\theta_T + N_o\Delta\theta_s$ so that, by adding zeros to the FFT, we can make Δx_s smaller than the peak to null cross range width of the sin x/x function. The highest output frequency or x coordinate (cross range dimension) is at $f_{max} = 1/\Delta t$ which corresponds to a cross range dimension of $X_{cr} = N\Delta x_s$ or

$$X_{cr} = (\lambda/2)/\Delta\theta_s \tag{1-73}$$

Equation (1-73) defines the unambiguous cross range window. It is the largest cross range target dimension which can be spanned unambiguously when input samples are $\Delta\theta_s$ radians apart.

We can obtain the unambiguous cross range window by another means. The difference in phase of the exponent of (1-69) between adjacent data samples is $2kx\Delta\theta_s$. The integral will become ambiguous when x varies far enough to force this phase difference through 2π radians. The value of x for which this is true yields the unambiguous cross range window given by (1-73).

We can also easily work with the data as samples in time from a target rotating at angular rate, Ω. The data are sampled in intervals Δt apart over a time period T. The output from the transform can be mapped from the Doppler frequency domain to the cross range domain simply by scaling the abscissa of the FFT, which has samples spaced $\Delta f = 1/T$ apart, by the factor $(\lambda/2)/\Omega$ according to (1-68).

Weighting can be used again to reduce the cross range sidelobes. The Hamming weight of (1-43) becomes

$$W_H(\theta) = 0.54 + 0.46 \cos(2\pi\theta/\Delta\theta_T) \tag{1-74}$$

which gives an ideal 3-dB cross range pulse width of approximately

$$R_{cr} = 1.3\ (\lambda/2)/\Delta\theta_T \tag{1-75}$$

The ambiguity relationships can be summarized as follows. The time T over which data must be collected to obtain a given cross range resolution may be found by noting that for an integration time, T, the ensuing Doppler resolution (for Hamming weighted data) is about 1.3/T Hz, which is equivalent to cross range resolution $R_{cr} = 1.3\ \lambda/(2\Omega T)$, so that to achieve a given value of R_{cr},

$$T = \frac{0.65\lambda}{R_{cr}\Omega} \tag{1-76}$$

where R_{cr} and λ are in the same units, Ω is in rad/s, and T is in s.

To avoid aliasing due to an insufficient radar pulse repetition frequency (PRF), the PRF must be higher than $2\Omega/\lambda$ times the largest target dimension (normal to the RLOS). Taking the PRF as $1/\Delta t$ (Δt being the sampling increment) yields a minimum PRI (Δt) of

$$\Delta t = \frac{(\lambda/2)}{\Omega X_{cr}} = \frac{1}{\text{Doppler spread}} \tag{1-77}$$

where "Doppler spread" is the overall Doppler frequency bandwidth of all reflecting points on a target in units of Hz, and Δt is in s.

1.3c The Synthetic Aperture Principle and Its Relation to Cross Range Resolution

A slightly different approach can be taken in viewing the effect of processing data from rotating targets: the synthetic aperture approximation in which a rotating target illuminated by a fixed radar is replaced by an equivalent condition of the radar moving about the fixed target. In this approach, the data are assumed to be recorded at various radar positions and the signal is processed after a sequence of positions is completed as if an antenna aperture

had been created. The synthetic aperture relationships are summarized in Figure 1-19, based on common antenna formulas taking into account two-way transmissions. As may be noted from the sketch and the approximations, the same relationships may be derived from the antenna aperture viewpoint as were previously derived from Doppler frequency resolution relationships (or from aspect angle change relationships). Note that the factor of 1.3 has not been included in the Figure 1-19 result for cross range resolution because amplitude weighting was not considered.

ROTATION OF TARGET ABOUT POINT IS EQUIVALENT TO MOVING RADAR ALONG ARC CENTERED ON TARGET

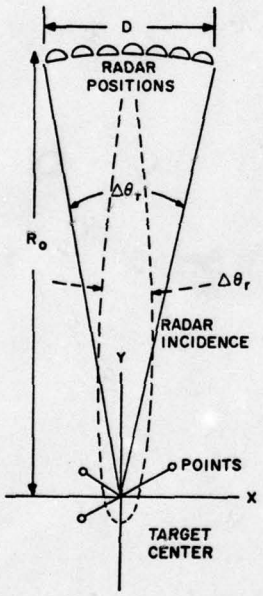

APPROXIMATE APERTURE WIDTH (D) FOR SMALL TOTAL SCAN ANGLE ($\Delta\theta_T$) AND LARGE RADIUS (R_o)

$$D \approx R_o \ \Delta\theta_T$$

FAR FIELD BEAMWIDTH ($\Delta\theta_r$) WITH RECTANGULAR APERTURE (D)

$$\Delta\theta_r \approx \frac{(\lambda/2)}{D} \approx \frac{(\lambda/2)}{R_o \Delta\theta_T}$$

CROSS RANGE (X) RESOLUTION AT TARGET CENTER

$$R_{cr} \approx R_o \Delta\theta_r \approx \frac{(\lambda/2)}{\Delta\theta_T}$$

SLANT RANGE (Y) LOCATIONS GIVEN BY PROCESSING LARGE BANDWIDTH SIGNALS

CROSS RANGE (X) BY SCANNING SYNTHETIC BEAM ACROSS TARGET

Figure 1-19

The synthetic aperture sense of high resolution processing has been used more widely in describing ground mapping techniques in which the radar is carried on an aircraft actually moving past ground area targets. Such ground mapping has been performed for several years and was the precedent of imaging of rotating space objects. (Two-dimensional synthetic aperture relationships are further discussed in Section 4.)

1.3d Doppler-Time-Intensity (DTI) Plots

Let the coherent data from a rotating target be Fourier transformed with suitable weighting for sidelobe reduction. Then a series of such spectral functions might be derived for changing integration center times and plotted in a three-dimensional sense with: (1) Doppler frequency (2) center time of integration, and (3) spectral intensity as the three axes. This may be called a Doppler-Time-Intensity (DTI) plot. (A DTI may be comparable to the common Range-Time-Intensity (RTI) plots from pulsed radar sytems, either in a three-dimensional projection sense or by using some version of a light or dark area true intensity modulation scheme.)

If the rotational motion is well-defined, the Doppler frequency axis may be scaled to become a cross range axis, x, from the conversion formulas of the previous discussions, and the time axis might be related to a target rotation angle, θ. The peaks of point responses may then trace out sinusoidal paths as idealized in Figure 1-20 for a simple rotating target. In Figure 1-20, the contour of a particular point is a sine wave with a maximum excursion, L_i, and an initial position, θ_{oi}.

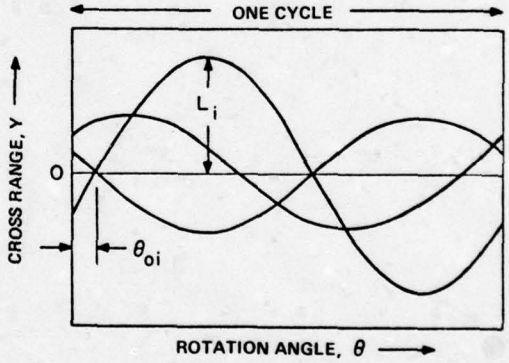

Figure 1-20

The total integration span $\Delta\theta_T$ need only be large enough to give sufficient cross range resolution (3 dB cross range resolution for a Hamming weight = $1.3\ \lambda/(2\ \Delta\theta_T)$ as derived previously). The sampling rate determines the unambiguous cross range window given by (1-73). As pointed out in Section 1.2d, the rate at which the data are sampled in real time is equal to the radar pulse repetition frequency (PRF). DTI plots are most useful in processing a narrowband signal which completely envelops the collection of point scatterers which compose the target.

Results of processing data from two model targets rotating about a fixed axis on a ground-based model measurements range will be presented to illustrate DTI plots with realistic signal reflections. The results were obtained in a study at SURC sponsored by the Rome Air Development Center. During this study, coherent processing of narrowband amplitude and phase data was accomplished with measurements obtained from General Dynamics of Fort Worth, Texas.

The simplest target was a right circular cylinder about 10.5 in long by 6.3 in diameter. Plots of the recorded amplitude and phase data from this cylinder are presented in Figure 1-21. These data were converted to complex pairs, Hamming weighted and Fourier transformed.

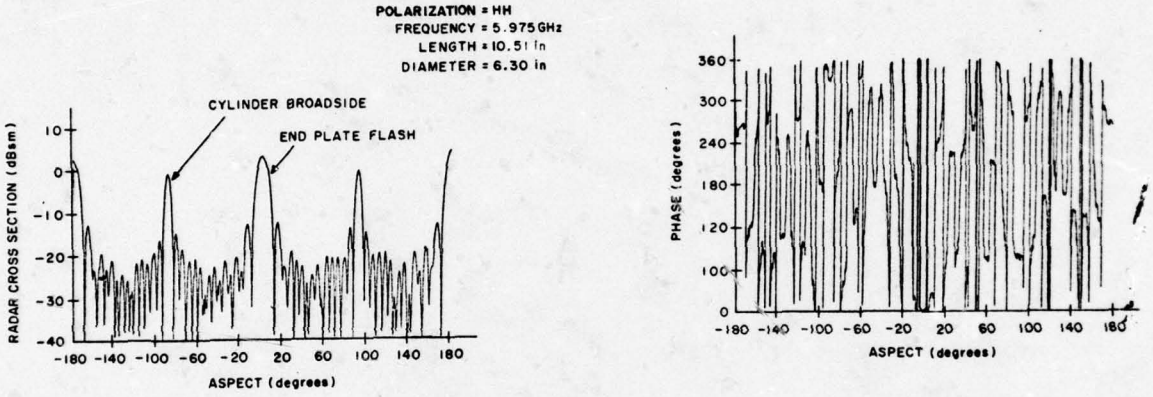

Figure 1-21

Results of the cylinder data processing are given in Figures 1-22, 1-23, and 1-24. The parameters of the processing were:

Integration Span	24°
Integration Increment	3°
Ideal Point Resolution with Hamming Weight	3 in

Figures 1-22 and 1-23 are in the form of true intensity modulation displays, while Figure 1-24 is a display in a three-dimensional projection format. The plot in Figure 1-22 was obtained by normalizing the intensities to the maximum of all the Fourier transforms. This maximum occurred in the integration which included the specular aspect to the round, flat end-plate. The plot in Figure 1-23 was obtained by normalizing each sweep to the maximum value in that sweep.

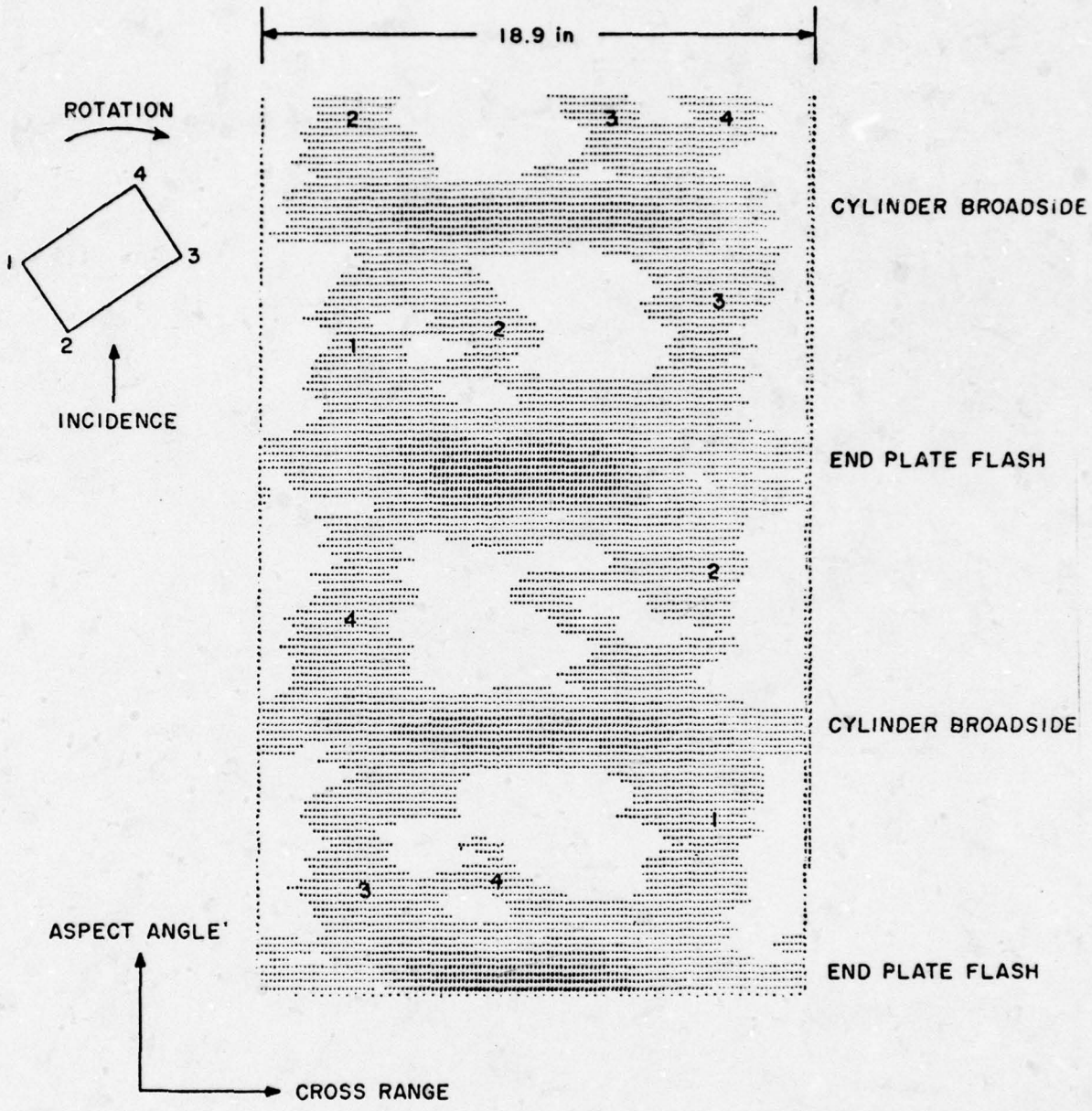
18.9 in
ROTATION
4
1
3
2
INCIDENCE
CYLINDER BROADSIDE
END PLATE FLASH
CYLINDER BROADSIDE
END PLATE FLASH
ASPECT ANGLE
CROSS RANGE

Figure 1-22

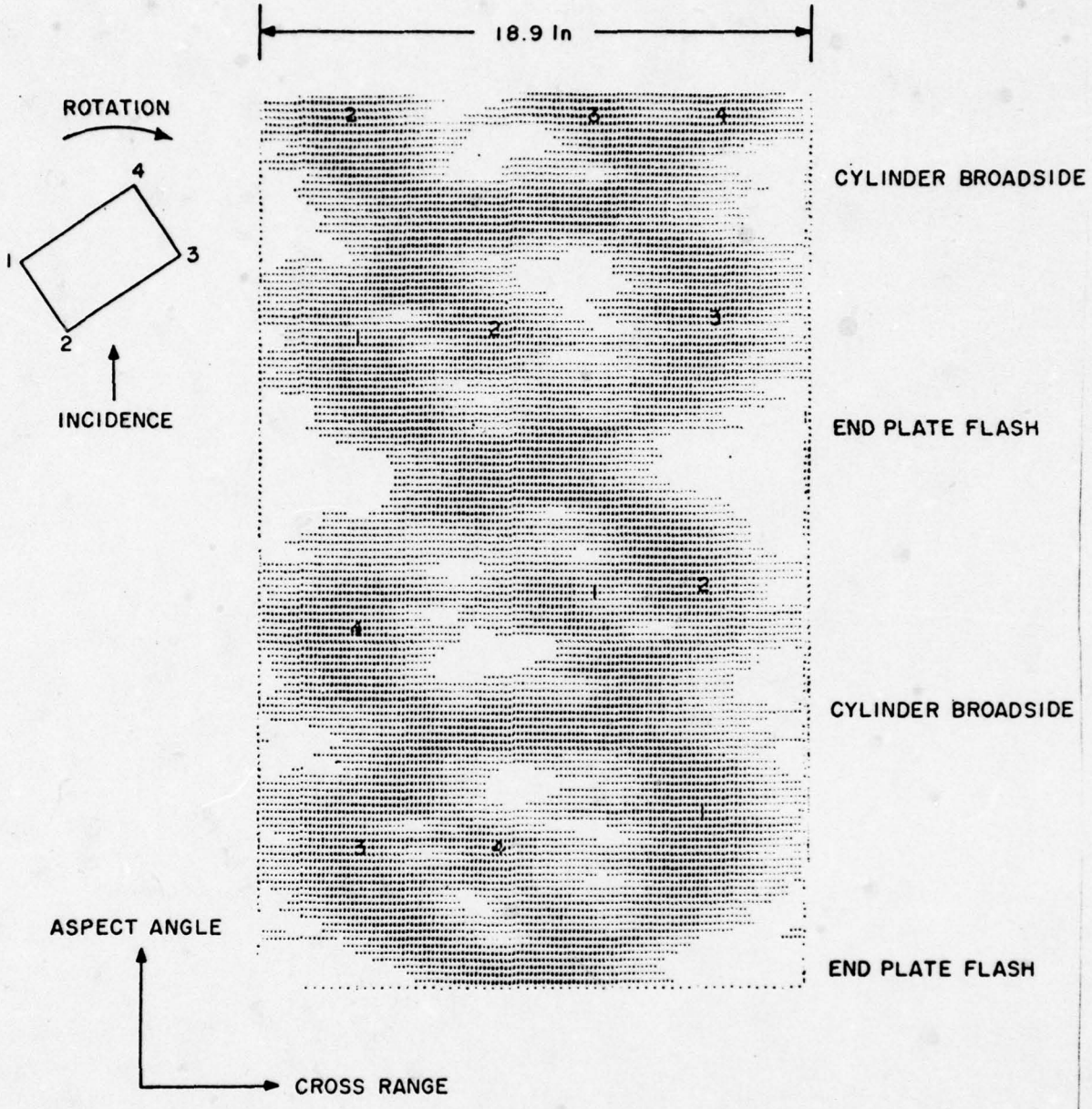
18.9 In
ROTATION
4
1
3
2
INCIDENCE
CYLINDER BROADSIDE
END PLATE FLASH
CYLINDER BROADSIDE
END PLATE FLASH
ASPECT ANGLE
CROSS RANGE

Figure 1-23

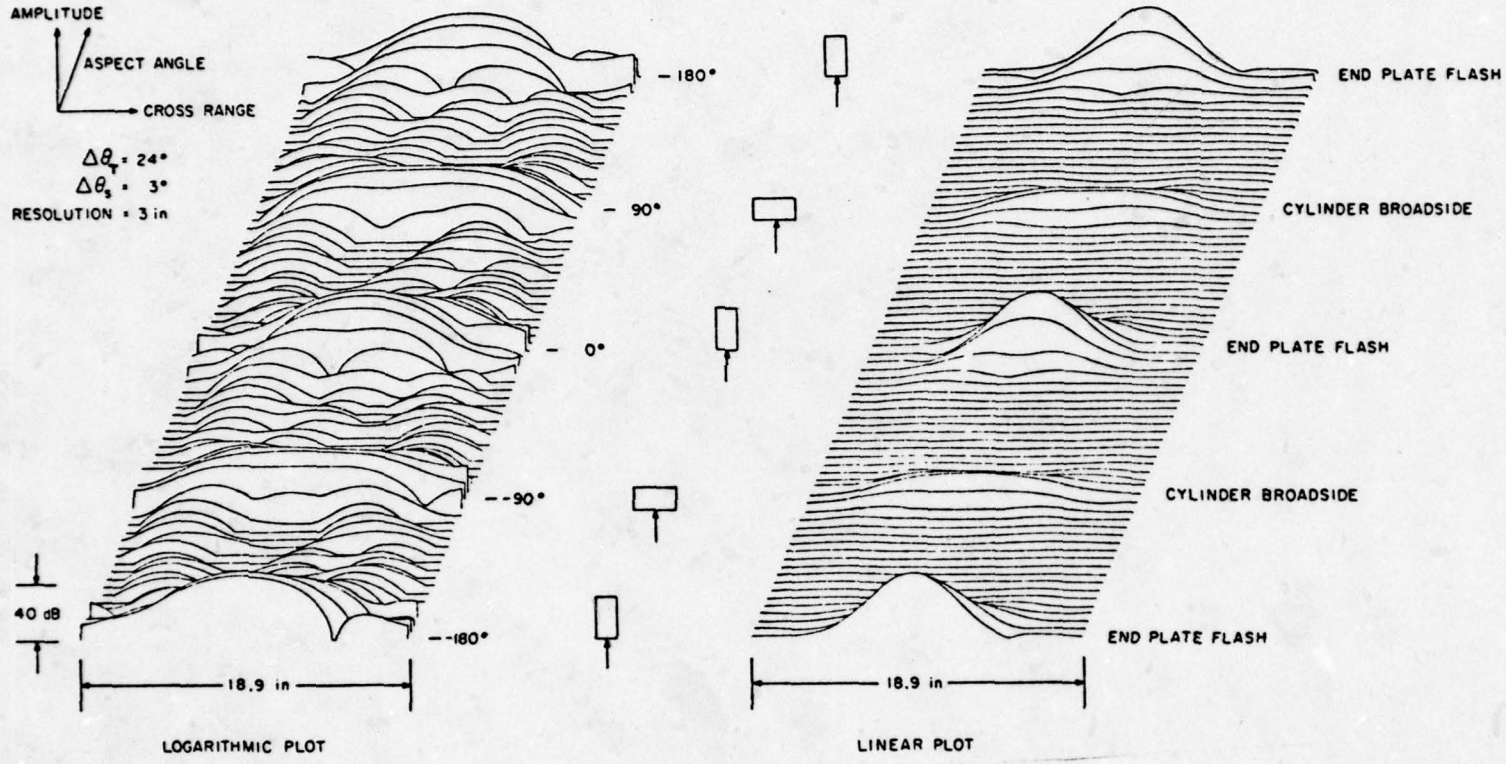
AMPLITUDE
ASPECT ANGLE
CROSS RANGE
$\Delta\theta_T$ = 24°
$\Delta\theta_s$ = 3°
RESOLUTION = 3 in
180°
90°
0°
-90°
-180°
40 dB
18.9 in
LOGARITHMIC PLOT
END PLATE FLASH
CYLINDER BROADSIDE
END PLATE FLASH
CYLINDER BROADSIDE
END PLATE FLASH
18.9 in
LINEAR PLOT

Figure 1-24

Figure 1-22 emphasizes the specular aspects, while Figure 1-23 emphasizes the low-level scattering from the cylinder edges. Figure 1-24 shows both linear and logarithmic plots of amplitude data in a three-dimensional presentation. The linear plot emphasizes specular aspects while the logarithmic plot shows edge scattering amplitudes. At non-specular aspects, three distinct returns can be noted. These returns are from the three illuminated edges of the cylinder. The cross range extents of the returns may be used to directly estimate dimensions, such as length and diameter.

Similar processing was performed on a second model which was a cone-cylinder-frustum combination. A plot of the recorded amplitude data is shown in Figure 1-25. The integration span in the Doppler processing was 24° and the sampling increment was 1°, which gave an unambiguous cross-range window of 56.576 in. An intensity modulation display of a resulting DTI is shown in Figure 1-26, with the amplitudes of each sweep normalized to the highest amplitude in that sweep. The displayed dynamic range of each sweep was 7.5 dB, which eliminated certain excessive background effects. The plot is overlaid with a series of sinusoids based on the location of various discontinuity points. The angles over which the different points persisted in scattering amplitude may be sensed with the aid of the sinusoid plots. The extreme corners of the frustum (points 1 and 7) are seen to persist over large ranges of aspect angle. The tip of the cone gives rise to significant scattering near grazing incidence over about 40° of aspect change.

In Figure 1-27, both linear and logarithmic plots of Fourier transformed amplitude data are given in a three-dimensional presentation for the cone-cylinder-frustum model. Again, the linear plot emphasizes the specular aspects while the logarithmic plot allows edge scattering amplitudes to be more prominent. In the linear plot, the conic flashes tend to have the shape of a conic. Data taken near specular flashes (such as a conic) can be used to form an approximate radius profile of the body by employing a special transform discussed further in Section 1.5.

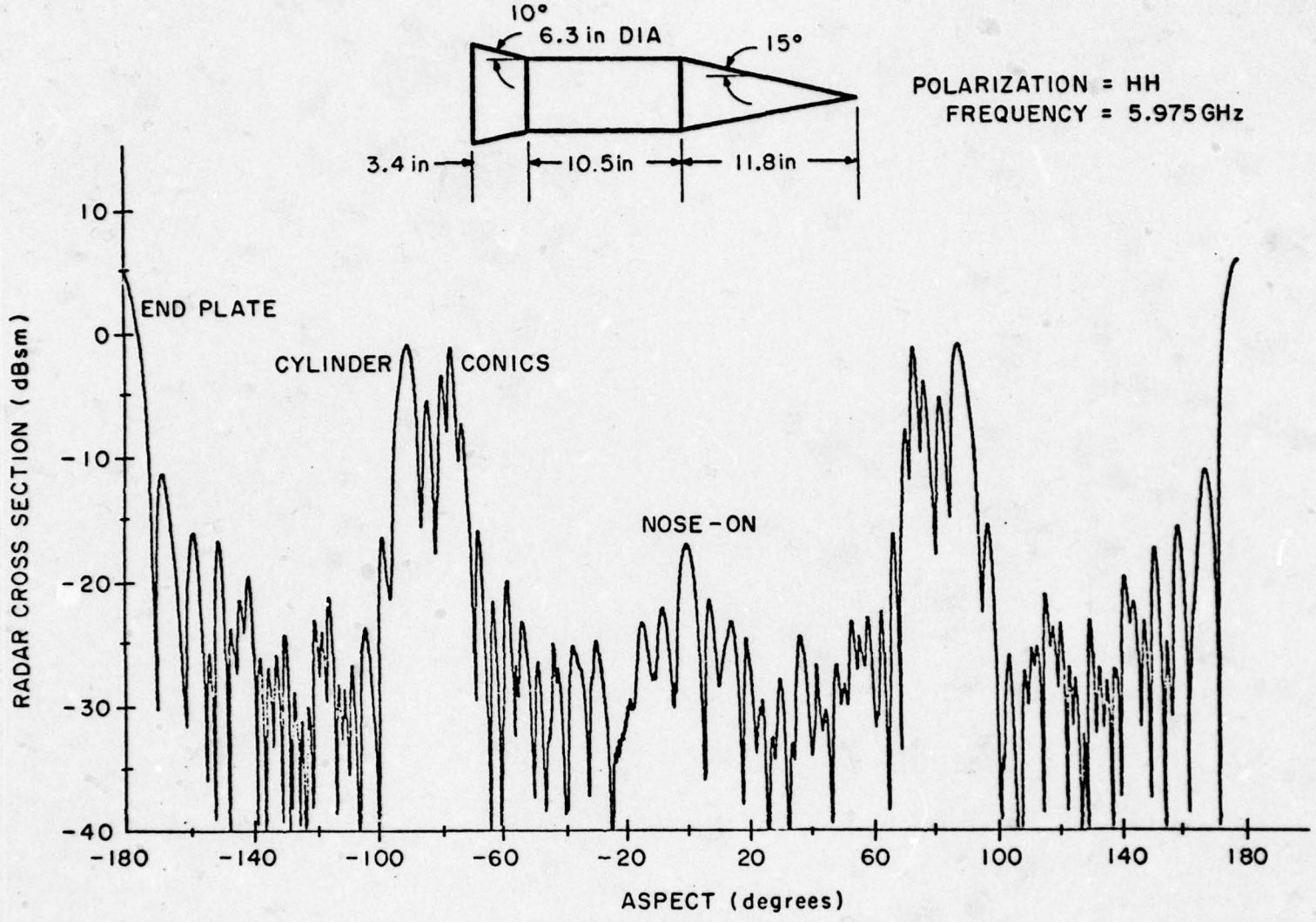
10°
6.3 in DIA
15°
3.4 in
10.5in
11.8in
POLARIZATION = HH
FREQUENCY = 5.975GHz
END PLATE
CYLINDER
CONICS
NOSE-ON
RADAR CROSS SECTION (dBsm)
10
0
-10
-20
-30
-40
-180
-140
-100
-60
-20
20
60
100
140
180
ASPECT (degrees)

Figure 1-25

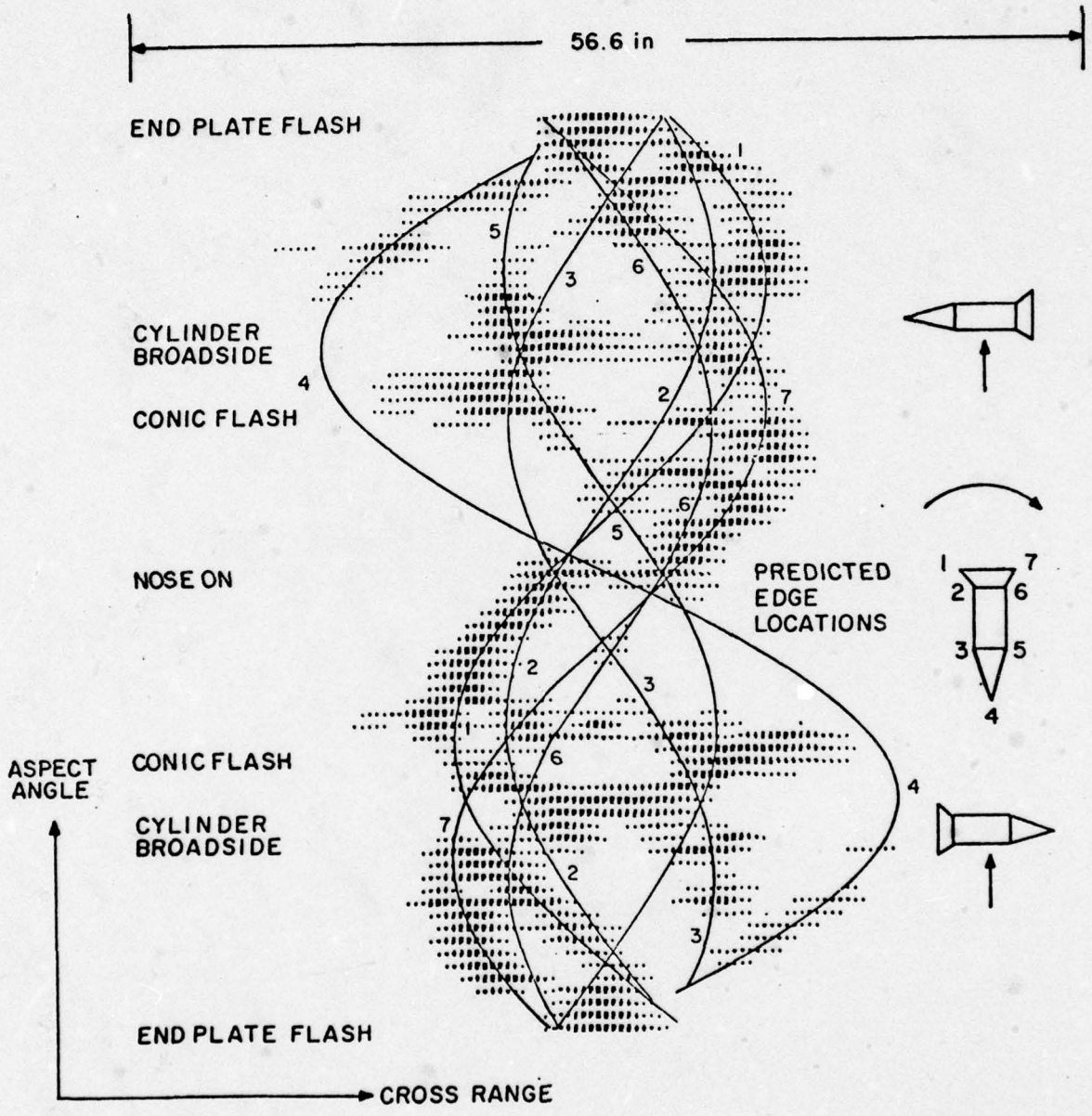
56.6 in
END PLATE FLASH
CYLINDER BROADSIDE
CONIC FLASH
NOSE ON
CONIC FLASH
CYLINDER BROADSIDE
END PLATE FLASH
ASPECT ANGLE
CROSS RANGE
PREDICTED EDGE LOCATIONS

Figure 1-26

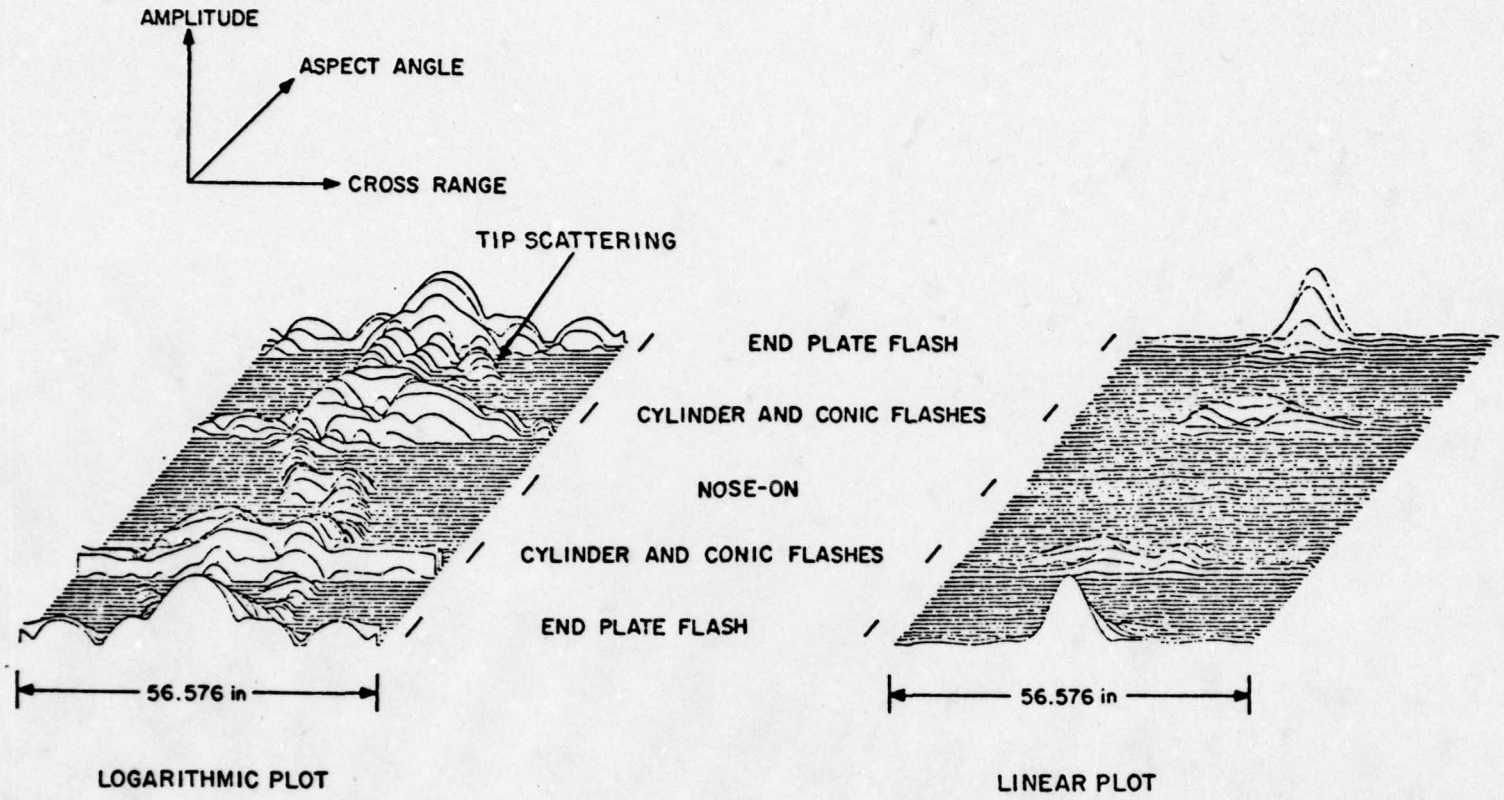
AMPLITUDE
ASPECT ANGLE
CROSS RANGE
TIP SCATTERING
END PLATE FLASH
CYLINDER AND CONIC FLASHES
NOSE-ON
CYLINDER AND CONIC FLASHES
END PLATE FLASH
56.576 in
56.576 in
LOGARITHMIC PLOT
LINEAR PLOT

Figure 1-27

These sample displays of cross-range versus aspect angle with amplitude plotted in an intensity form or in a three-dimensional projection form illustrate the information an SOI analyst can obtain by both using phase and amplitude information in processing coherent radar data. From Figure 1-26, one can obtain the diameter of the frustum and length of the cylinder as well as the overall length of the body, since the tip scattering has been identified. From the angular separation between specular flashes, one can determine the angle of the conic section and its unambiguous placement with respect to the cylinder. An SOI analyst, using amplitude data only, might have difficulty determining the cone and frustum components and their placement with respect to the cylinder. The specular response effects and the sorting of component sections may be clearer in the explanations of Section 1.5, which considers special versions of the DTI plots centered on specular aspects.

1.4 RADAR IMAGING THEORY FOR OBTAINING POINT TARGET MODELS WITH VARIOUS BANDWIDTH AND COHERENCE CONDITIONS

1.4a Range-Time-Intensity Plots and Two-Dimensional Images Using Wideband Data

With a monostatic tracking radar system, a transmitted signal may have a wide enough bandwidth to resolve reflection centers in slant range. Data may then be recorded and plotted in the form of range versus time (or aspect angle) with the amplitude of returned pulses used in a intensity modulation display of the signal. Such a plot is usually called a Range-Time-Intensity (RTI) plot. An RTI plot can be viewed in the same fashion as the DTI plot of Figure 1-20 with cross range replaced by slant range. Again, for simple rotation conditions a point scatterer will trace out a sinusoid with a maximum amplitude, L_i, and an initial position dependent on θ_{oi}. (If the point traces out sinusoids in an RTI plot, they are cosinusoids in a DTI plot.) A typical RTI plot for a model range target is shown in Figure 1, page 6 of the report reproduced in Appendix A. The peaks of pulses occur where discontinuites in the target are present.

A first-order, two-dimensional image may be readily formed when both amplitude and phase data are available at all the wideband signal slant range

sampling points. The slant range points are properly aligned and the signals are Fourier transformed along each slant range position in the manner described for DTI plots. Then these DTI plots are displayed in their corresponding slant range order. Thus, in unnormalized form, this image is an intensity modulation display of Doppler frequency shift versus slant range. If the Doppler scale is normalized to the cross range dimension, as discussed in the previous sections, the resultant radar image may approach a version of a rough optical image. This is termed "first-order" image processing. Further details of the first-order image formulation are given in Appendix A.

In simplest form, the plane of the first-order image is parallel to the radar line-of-sight and perpendicular to the axis of rotation. Determination of image scale factors and image plane orientations for more complex motion and tracking conditions are discussed in Section 4.

1.4b Distortion Effects in First Order Images

If an ideal point scatterer can appear anywhere within a first-order image frame, its response function will be narrowest in width and highest in amplitude when it is placed at the center of rotation. During an integration span, only the point at the center does not move, so that it will have a slant range lobewidth equal to that of the transmitted pulse and a Doppler frequency (or cross range) lobewidth equal to that of a linearly moving target point. A point placed at any other position will move, and the motion will result in some spreading of the response function and a reduction in peak amplitude relative to that of a point at the center.

In the Doppler response function analysis with narrowband data, the slant range pulsewidth is assumed very wide, such that the amplitude of any point reflection stays approximately constant during an integration span. Under these circumstances a Fourier transform of the signals gives an ideal response function if the point is assumed to move approximately linearly. Consider the slant range of any one point, which could be stated as

$$r = y_o \cos\theta + x_o \sin\theta \qquad (1\text{-}78)$$

where x_o is the mean cross range position and y_o is the mean slant range position of the point during the changing aspect variation ($\theta = 0°$ at the mean position). The linear variation implies that $\sin\theta \approx \theta$ and $\cos\theta \approx 1$. One can see from (1-78), that r is not linear in this sense unless $x_o = y_o = 0$. A second-order approximation to (1-78) would be to let $\cos\theta \approx 1 - \theta^2/2$. One may then see that the second-order Doppler frequency response function will deviate according to the mean slant range position, y_o, of a point. The distortion might be sensed qualitatively as a "Doppler walk" effect, which can be viewed in terms of the cross range motion of a point relative to the fixed point Doppler resolution function. A measure of cross range resolution was stated previously as $R_{cr} = 1.3\lambda/2\Delta\theta_T$, where $\Delta\theta_T$ is the total integration span. If a point scatterer appears to move more than a fraction of the R_{cr} value, that response point might be said to have significant Doppler walk. (Doppler frequency and cross range are assumed to be interchangeable quantities through the cross range scale conversion factors for rigidly connected points). An example of Doppler walk is illustrated in Figure 1-28, in which a point along the y-axis (for slant range) at some distance from the center has an equivalent Doppler pulse motion greater than that of the point at the center of rotation and would therefore be expected to have an image response function that spreads relative to that of the fixed point.

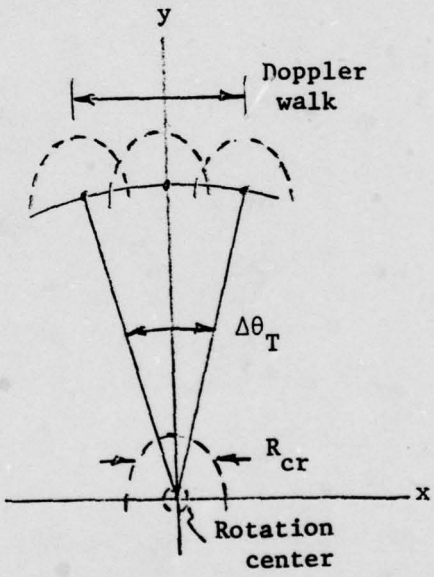

Figure 1-28

Even if the point motion is linear enough to satisfy a Doppler resolution criterion, there can be enough motion to spread the response function in a slant range sense, which could then be called "slant range walk", or simply "range walk". Slant range walk is illustrated in Figure 1-29, where a point some distance from the rotation center is shown with its pulse responses spreading out in slant range as the point moves. As a result of this motion,

the moving point slant range resolution will be wider than the R_{sr} illustrated for the fixed point. A less obvious effect is that there will also be a cross range spreading as a result of this range walk. This first order processing for any one image line in cross range is based on the data that appear at a particular slant range position. In the Figure 1-29 example, the correct point location after processing would be along the y = 0 line. For this line, the sampling of the range-walked pulse would be at different points on the slant range pulse amplitude function for different aspects, as might be sensed in the sketch. The result is that the point signals to be transformed would be weighted by the pulse shape, in addition to whatever weighting is used for sidelobe reduction. Thus, the amplitude data are not rectangular over the integration span even if sidelobe reduction weighting is not used; consequently, the integrated response function would be spread in Doppler frequency as well as slant range. The final result is that, even for linear motion, a range walk effect can spread the response function in both directions x and y, relative to the response function of a point at x = 0, y = 0.

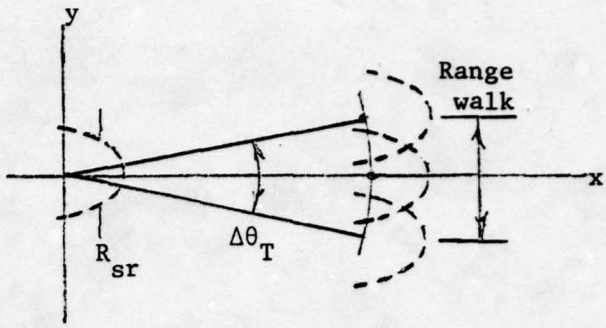

Figure 1-29

The combination of range and Doppler walk can be coupled in the resulting response function, and target reflection points in the general direction outward from the center of rotation will appear less focused than those near the center. A general expression for the distortion effect would be dependent on the target mean position (x_o, y_o), the integration span $(\Delta\theta_T)$, and the transmitted slant range pulse shape, and is not readily formulated with simplifications. Such expressions were approximately derived for the model range measurements image processing in the Addendum to Appendix A (see the second appendix of the Addendum).

In general, the rule for minimizing distortion or preserving first-order resolution can be simply stated: the integration span should be limited

so that slant range or cross range walk of extremely positioned points is limited to less than the fixed point resolution values R_{cr} and R_{sr}. Allowing greater motion of points does not necessarily make an image invalid, but analysts must keep the distortion effect in mind when studying the responses.

For very wide integration angles, not only can a distortion occur because of range and Doppler walk, but the realistic scattering amplitude of a localized region may change with rotation angle. The result is that the response function peak position might not occur at the mean location of the scattering center for the integration span. This mean location of a point, usually assumed in a first-order image analysis, is valid for a constant amplitude localized scattering, even if range and Doppler walk does occur.

1.4c Wide Angle Signal Integration Formulations (Higher Order Coherent Imaging)

The nonlinear motion of rotating points may be taken into account so that the first order distortion effects in two-dimensional images can be removed under simple rotation conditions. The resulting integrals are not simple Fourier transforms, however, and the efficient FFT algorithm cannot be simply applied. The terms "wide angle integration", "higher order coherent imaging", or "extended coherent processing" have been applied to this type of imaging.

Such an integration process may be visualized graphically in terms of first order images with limited data. Suppose we take the radar returns from a wideband system at one aspect angle θ_1, and store the signal numbers in an x-y grid with constant values of the signal along x lines, as illustrated for amplitude in Figure 1-30a. This would be equivalent to forming one first-order image frame with only one input data sweep, one sweep giving no cross range resolution after integration. A scattering point off the center of the x-y grid produces the pulse response. Now let the target rotate to a second aspect position and let a second set of data be obtained in the second grid, as illustrated in Figure 1-30b. One might readily see that if the second grid were rotated relative to the first grid through an angle $(\theta_2 - \theta_1)$ and then superposed, the position of the point in the second grid would coincide with that in the first grid.

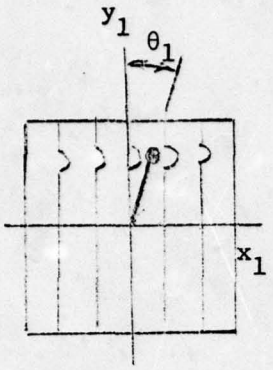

Figure 1-30a

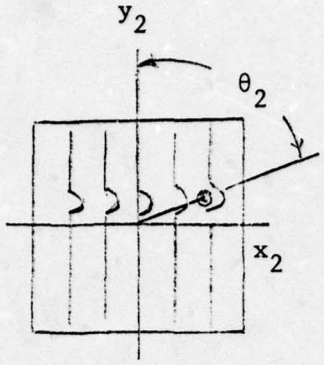

Figure 1-30b

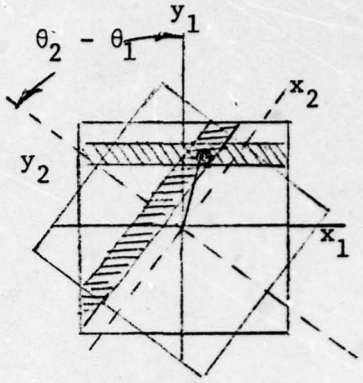

Figure 1-30c

The signal amplitudes might then be superposed, and the pulse peak bands, as illustrated in Figure 1-30c, would cross over at the location of the point. The point was arbitrarily located so one should see that this type of cross over would occur at the location of any other points. The rotation angle between frames is $(\theta_2 - \theta_1)$, which means only the relative rotation angle is important. The noncoherent integration of wideband signals in this manner produces poor response functions, which spread out with high amplitudes and are difficult to interpret if scattering point amplitudes differ significantly.

To coherently integrate the signals at the cross over point of the bands, the phases of the signals within the bands at the cross over point should be equal, maximizing the resulting function at that point. This is readily possible when we remember that the phase shift of any one point return at one aspect angle is dependent on 2ky. Consequently, if the phase 2ky is subtracted (with the proper sign) from all the signals in each grid position, the phase directly under the peak of the pulse from a point will be set to zero for each aspect angle. Therefore, the summed signals in the superposition (Figure 1-30c) will necessarily add with the same phase angle. There will then be a build-up of a true peak response in two dimensions at the true peak location, as several sweeps are superimposed. Point responses will then have resolution functions independent of their location relative to the center of rotation. Because of the sampled nature of the data, one can see that this type of integration requires

interpolation of practical signals to make the rotated points coincide from one frame to next, unlike the first-order processing which required no interpolation for equispaced data samples.

For this type of rotating point matched signal integration, the limiting response function from a point scatterer may be written in continuous integral form as

$$F(x, y) = \int_{-\Delta\theta_T/2}^{\Delta\theta_T/2} A(y - y_i) e^{j2k(y_i - y)} d\theta \qquad (1\text{-}79)$$

For a complex signal from a sum of point targets all rigidly connected of the form

$$V(\theta, y_i) = \sqrt{\sigma(\theta)}\, e^{j\phi(\theta)} = \sum A(y - y_i) e^{j2ky_i} \qquad (1\text{-}80)$$

the integral becomes after using (1-64)

$$F(x, y) = \int_{-\Delta\theta_T/2}^{\Delta\theta_T/2} \sqrt{\sigma(0)}\, e^{j\phi(\theta)}\, e^{-2jk(y\cos\theta - x\sin\theta)} d\theta \qquad (1\text{-}81)$$

From the previous definitions in the first-order processing description, we have

$$\begin{aligned} y_i - y &= (y_{io}\cos\theta - x_{io}\sin\theta) - (y\cos\theta - x\sin\theta) \\ &= \Delta y\cos\theta - \Delta x\sin\theta \end{aligned} \qquad (1\text{-}82)$$

where Δy and Δx are now the differences in position in the composite frame from the location of the particular scattering center associated with index i. Using polar coordinates as defined in Figure 1-31, with the point scatterer at the center, the response integral becomes

$$F(r, \alpha) = \int_{\frac{-\Delta\theta_T}{2}}^{\frac{+\Delta\theta_T}{2}} A(r\cos(\alpha - \theta))\; e^{j2kr\cos(\alpha - \theta)} d\theta \qquad (1\text{-}83)$$

since $y_i - y = r[\cos\alpha\cos\theta + \sin\alpha\sin\theta]$. A classical result of this integral occurs when the pulse function is unity, signifying a CW signal (may be approximated by a long pulse with small bandwidth). Integration is over a full cycle; i.e., $\Delta\theta_T = 2\pi$. Then the integral is

$$F(r, \alpha) = \int_{-\pi}^{+\pi} e^{j2kr\cos(\alpha - \theta)} d\theta$$

$$= 2\pi J_o(2kr) \qquad (1\text{-}84)$$

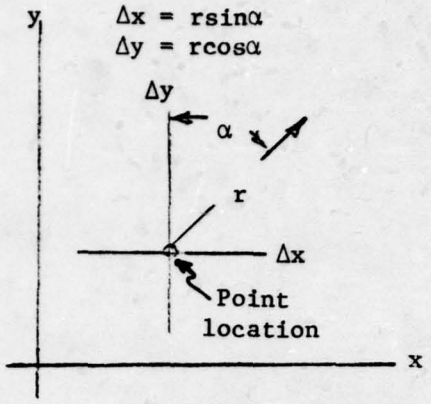

Figure 1-31

For (1-84) to apply, a point scatterer must persist with a constant amplitude for the full cycle of rotation. This will not be achieved for practical targets made of extended surfaces where point-scattering effects are due to discontinuities in surfaces, since amplitudes of such points will vary and disappear in shadow regions as the target rotates. However, the result is useful to establish limiting values of point resolution. The J_o function has a first zero at an argument of 2.405, so that the representative pulse width between nulls is about $0.8(\lambda/2)$ and between 3-dB points the total width is about $0.36(\lambda/2)$.

Wide angle imaging with wideband data theoretically allows an interesting possibility of resolving ambiguity effects due to sampled data. The plot at the top of Figure 1-32 represents first-order image amplitudes of a single point scatterer at the center of rotation. The cross range display is extended beyond the unambiguous cross range interval of the data, so the first ambiguities of the center point response can be seen in this plot. The ambiguous responses are identical to the unambiguous response, as expected from first order imaging theory. Therefore, whether the point is truly located at the center, or is at either of the ambiguous positions, cannot be determined from this one image. The bottom plot in Figure 1-32 shows the results of using a wide angle integral like (1-79) and spanning a greater angle (60° compared to 10°). The wide angle

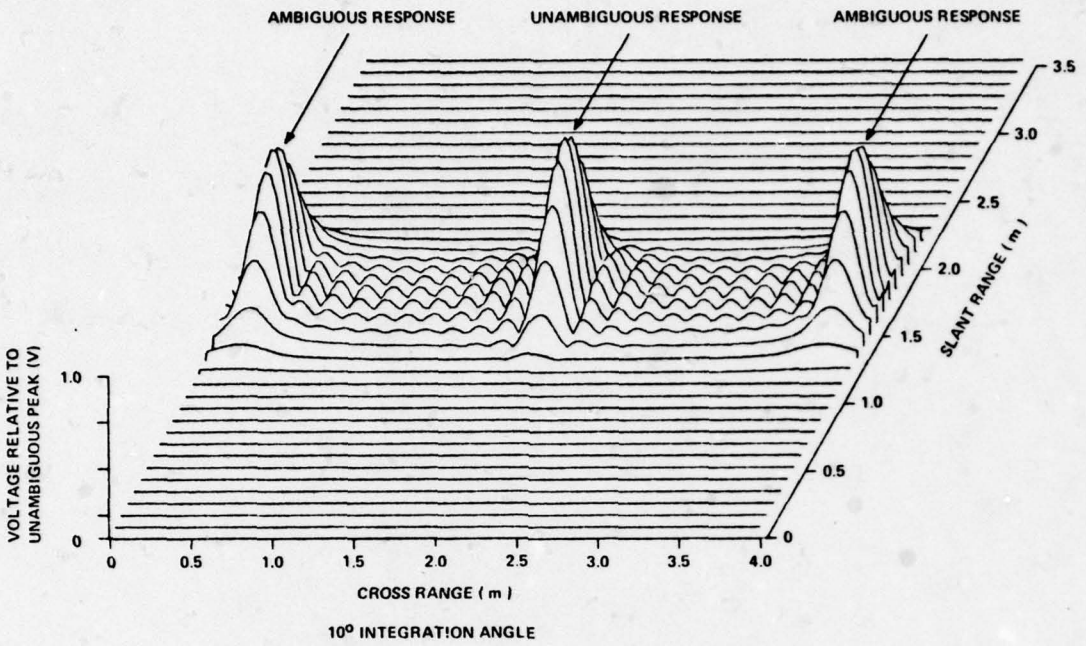
AMBIGUOUS RESPONSE
UNAMBIGUOUS RESPONSE
AMBIGUOUS RESPONSE
VOLTAGE RELATIVE TO UNAMBIGUOUS PEAK (V)
1.0
0
0
0.5
1.0
1.5
2.0
2.5
3.0
3.5
4.0
CROSS RANGE (m)
SLANT RANGE (m)
0
0.5
1.0
1.5
2.0
2.5
3.0
3.5
10° INTEGRATION ANGLE

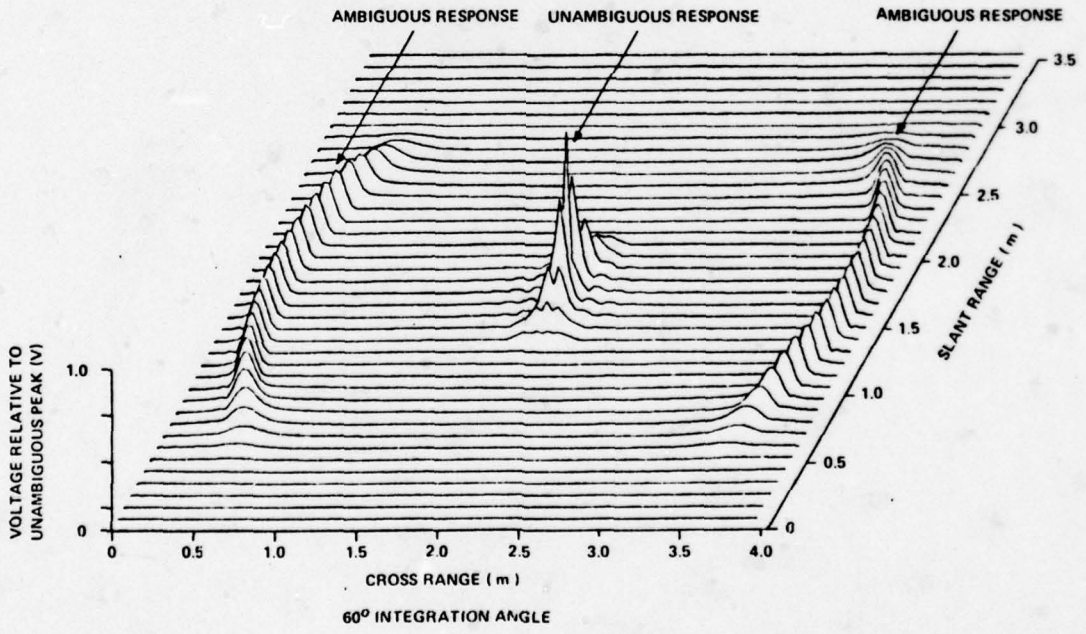
AMBIGUOUS RESPONSE
UNAMBIGUOUS RESPONSE
AMBIGUOUS RESPONSE
VOLTAGE RELATIVE TO UNAMBIGUOUS PEAK (V)
1.0
0
0
0.5
1.0
1.5
2.0
2.5
3.0
3.5
4.0
CROSS RANGE (m)
SLANT RANGE (m)
0
0.5
1.0
1.5
2.0
2.5
3.0
3.5
60° INTEGRATION ANGLE

Figure 1-32

ambiguous responses appear spread out in circular arcs with considerably lower amplitudes relative to the unambiguous response. Thus, there is little doubt about the correct location of the point in the second image. A similar effect would occur if the point were located at other positions. Arcs are formed about the true point locations with radii nX_{cr}, where X_{cr} is the unambiguous interval and n is a series of positive integers. In practical data, this effect is not as prominent because localized scattering tends not to persist over full integration spans, and the ambiguous responses become more like the unambiguous responses as the effective integration angle decreases. Sometimes an examination of just the values of the peak amplitudes in the wide angle integration may be useful in resolving the ambiguities, even though the ambiguous pulse spreading is not readily detectable. The problems become more difficult or impossible to solve as the target size extends across more than about two unambiguous intervals if the target has practical scatterers at several locations.

It is of interest to note the character of the unambiguous response in the bottom plot of Figure 1-32. The wide angle mainlobe takes on a distinctly different shape off the peak than obtained in the small angle integration images.

1.4d Narrowband Wide Angle Imaging

There is obvious appeal in the idea of obtaining two-dimensional images from narrowband signals, particularly because of the possibility of avoiding costs and problems of wideband systems. However, even in the most ideal circumstances, narrowband images tend to be of very limited quality in practical target cases, as will be discussed.

Based on an integral of the form (1-81), narrowband (no true range resolution) ideal-point response functions along a mean slant range direction are plotted in Figure 1-33a for three different integration spans, and a mean cross range plot is shown in Figure 1-33b for one integration span. A sample of a two-dimensional ideal point response function is shown in Figure 1-33c in intensity modulation form. A Hamming weighting function was included in these integrations. The terms slant range and cross range lose some of their meaning in

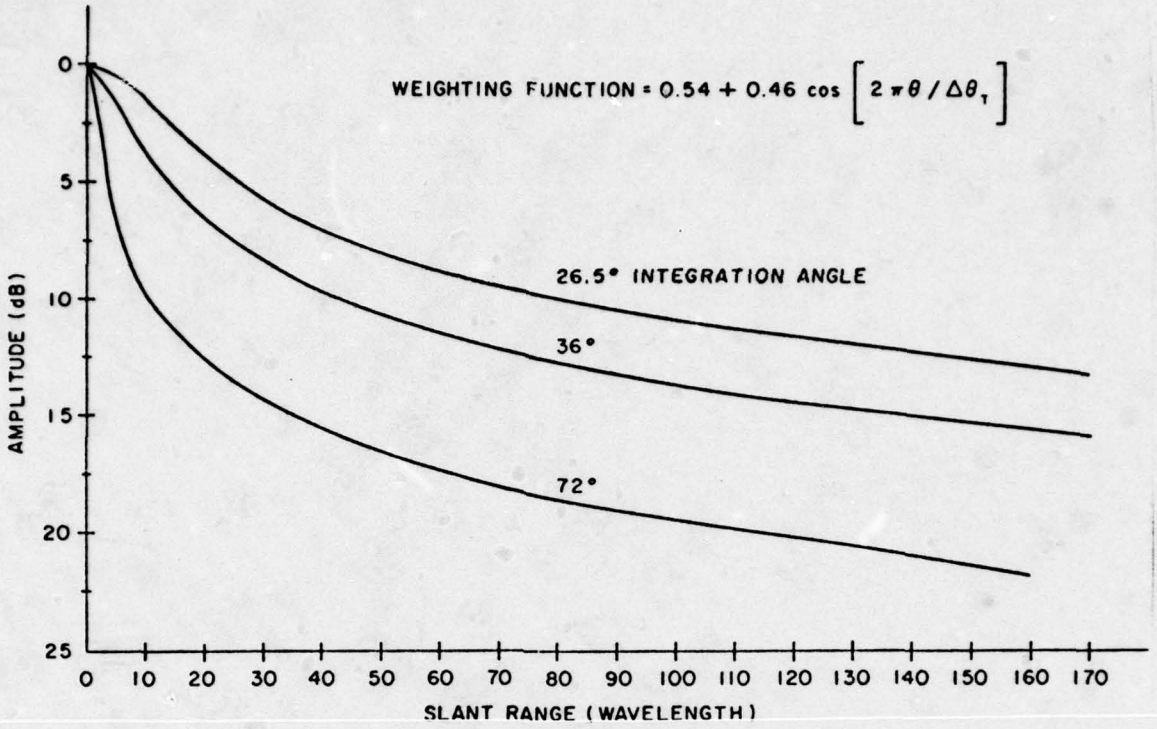

(a)

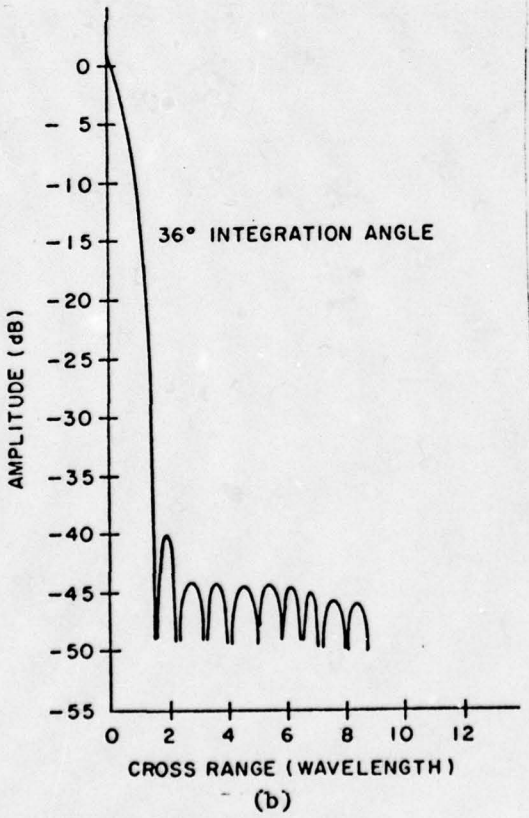

(b)

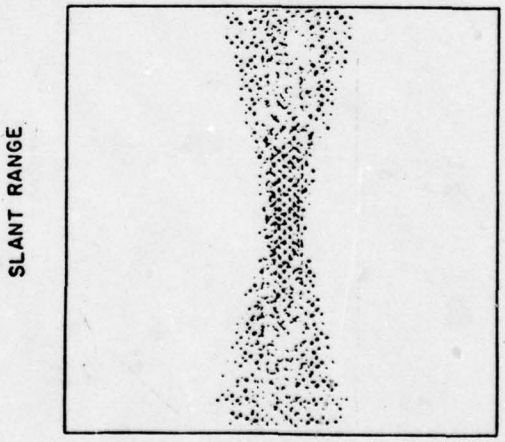

(c)

Figure 1-33

the wide angle integration case, compared to the more correct application in the case of first order imaging using wide band data. In these wide angle problems, the terms refer the mean target position during the integration span.

The slant range cuts in the response functions of Figure 1-33a drop-off very slowly compared to the cross range response of Figure 1-33b. The slow drop-off might be viewed as a high sidelobe effect, even though a first null is not shown in the Figure 1-33a plot. In this sense, even higher sidelobe levels appear at other cut lines away from the mean slant range diretion, as might be sensed from the Figure 1-33c plot. Different weighting functions, other than the Hamming weight, can be used to redistribute the response function amplitudes but an adequate weighting function has not been found that makes narrowband imaging of general practical use. Real target response functions will be used to illustrate some of the difficulties.

A set of two-dimensional narrowband images was obtained using General Dynamics data on the small cone-cylinder frustum discussed in Section 1.3d. The images were formed by evaluating the matched filter integral of (1-81) to obtain sets of $|F(x, y)|$ values which were then plotted in intensity modulation form. A Hamming weight was incorporated to suppress cross-range sidelobes.

Examples of the cone-cylinder frustum images are shown in Figure 1-34. Dimensions of the target were shown in Figure 1-25. The parameters of the processing were, λ = 1.975 in., $\Delta\theta_T$ = 69°, $\Delta\theta_S$ = 1°. Images are presented for six different average aspect angles. The Figure 1-34 images have a 7.5 dB dynamic range, which was found to yield good clarity without too much background. Care was taken to avoid integrating through specular aspects, since it was expected that this would cause the glint edge responses to be suppressed. The images are in agreement with the DTI plot of Figures 1-26 and 1-27. The extreme edges of the frustum show the largest amplitude scattering and persist in most views. The tip scattering is evident in views where the average direction of incidence is near grazing on the tip. In some views, extreme range sidelobes appear. It was usually determined that these were sidelobes by observing their change when a different weight was used. The appearance of some scattering

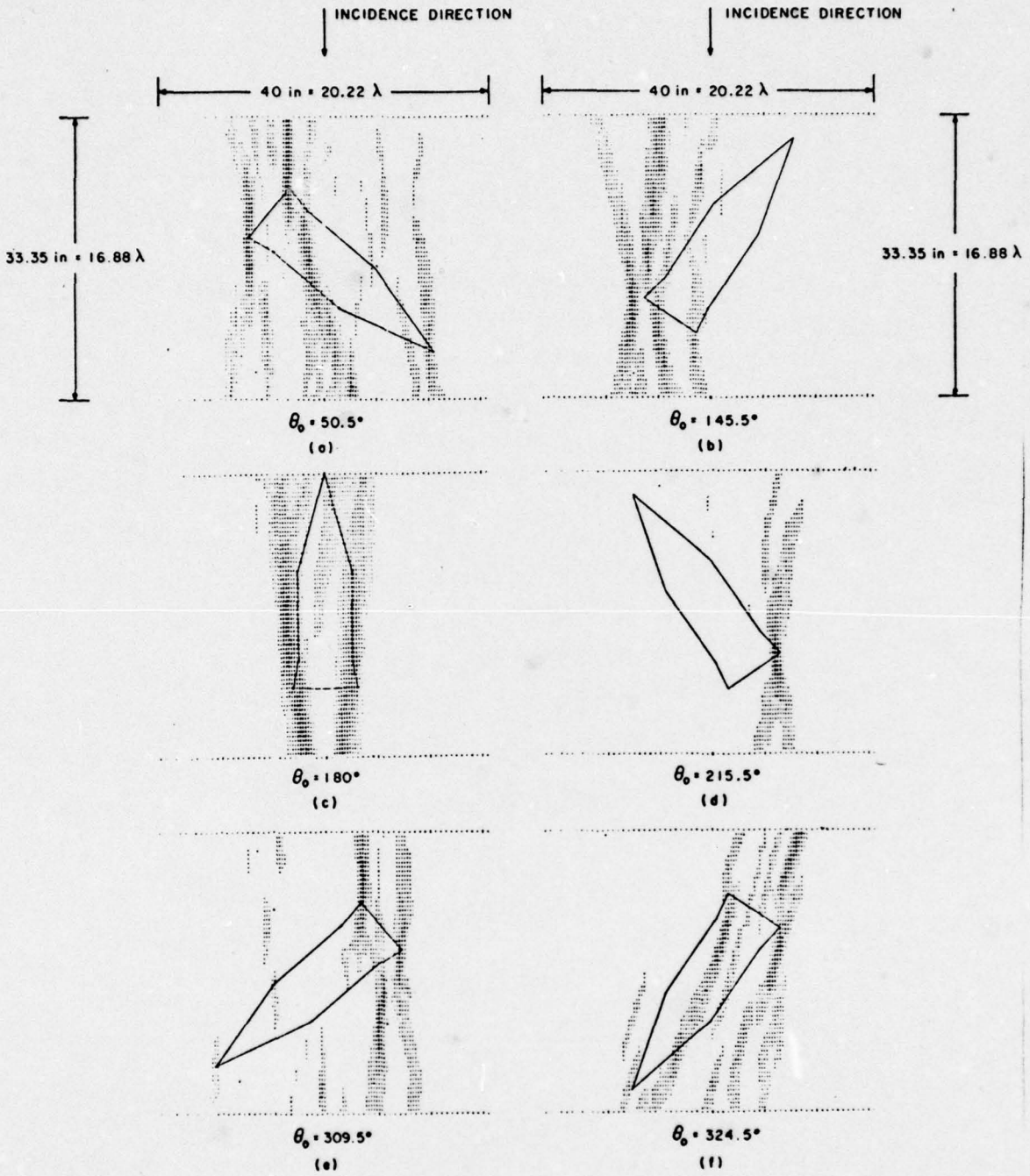

θ_0 - AVERAGE ASPECT ANGLE IN INTEGRATION SPAN

Figure 1-34

centers away from corners or edges was due to interference between range sidelobes created by nearby scatterers. The small size of the target permitted a finely sampled grid so that there were no sampling problems in the image plane. In addition, the scattering from edges, including the tip, persisted for long enough periods so that their response built up in the image plane. The scatterers were all approximately of the same magnitude so a dynamic range of only 7.5 dB gave clear images. However, in these narrowband images the target response points could not generally be unambiguously defined in the sense of the wideband images shown in Appendix A. It was concluded that the two-dimensional image processing of the narrowband signals would not significantly improve analysis results relative to the one-dimensional processing discussed in Section 1.3d. However, because some special cases may occur where this type of processing could be useful, the method should not be entirely discounted.

The main difficulties in wide angle narrowband imaging are: (1) localized scattering effects do not persist long enough in the constant amplitude point scatterer sense to allow sufficient resolution in the mean slant range direction, (2) the response function sidelobes are very high, which limits the dynamic range of scatterers that can be observed, (3) the condition of having a simple relative rotation of the target, with the axis of rotation perpendicular to the rotation axis, may not be present in realistic tracking geometries. In addition, for slow rotation rates, there is the translational motion compensation problem, as discussed in Sectin 1.6.

1.4e Noncoherent Narrowband and Wideband Imaging (Ambiguous Imaging)

An ambiguous version of the images described above can be created if amplitude versus aspect-angle data are available from rotating points and there is more than one point in the collection of point scatterers representing the target model. This can be demonstrated by considering the total narrowband reflection, V_T, as the complex summation

$$V_T = \sqrt{\sigma_T}\, e^{j\phi} = \sum_i V_i e^{j2ky_i} \qquad (1\text{-}85)$$

The magnitude squared of this summation can be obtained by multiplying the function by its complex conjugate, or

$$|V_T|^2 = \sum_i V_i e^{j2ky_i} \sum_i V_i e^{-j2ky_i} \tag{1-86}$$

$$= \sum_i (V_i)^2 + \sum_{i,j} 2V_iV_j\cos(2ky_{i,j})$$

where $y_{i,j} = y_i - y_j$ and $\sum_{ij}$ is on all combinations of i and j except i = j. In the last part of this development, the first term on the right is a mean value which is the summation of all the amplitudes squared and is equivalent to summing all the radar cross-section values of the points. The second summation is over all possible combinations of scatterers taken two at a time, resulting in a cosine function for each pair of scatterers with amplitude proportional to the product of the two amplitudes and an argument dependent on the instantanous phase, $2ky_{i,j}$, between the pair of scatterers. The absolute value, $|V_T|^2$, is proportional to the total RCS of the collection of points which will vary in a complex manner with rotation angle. The summations in the first part of the (1-86) derivation can be rewritten in the form

$$|(V_T)|^2 = \sum_k V_k e^{-j2ky_k} \sum_i V_i e^{+j2ky_i} \tag{1-87}$$

in which the index of one series in the product has been changed to k but still represents the same set of values as the i index.

First consider the narrow angle processing response, which would be obtained for a DTI type of display. If each term in the sum over i is Fourier transformed, the spectrum of the result would contain responses in frequency or, equivalently, cross range. Let us rewrite (1-87) as

$$|V_T|^2 = \sum_k V_k \sum_i V_i e^{j2k(y_i - y_k)} \tag{1-88}$$

The spectrum of each term can be considered as repeating for each kth term in the multiplying series. Each repeating spectrum of the i series is weighted in amplitude by the V_k term, and at the same time, the phase of the kth scatterer is subtracted from the phases in all the i terms. This has the effect of putting the point associated with the kth term at the point of zero Doppler

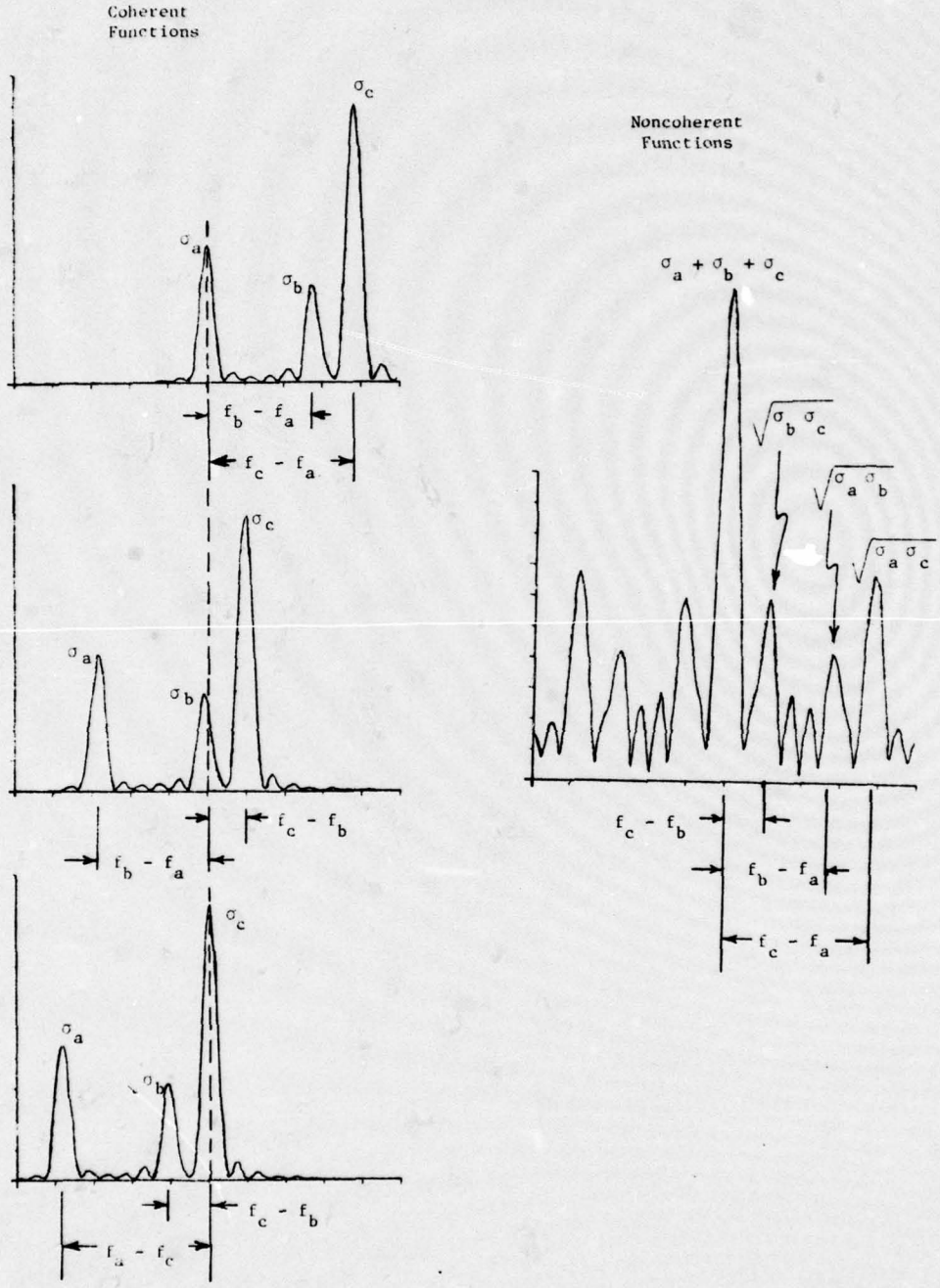
Coherent
Functions
Noncoherent
Functions
σ_a
σ_b
σ_c
$f_b - f_a$
$f_c - f_a$
$f_c - f_b$
$f_a - f_c$
$\sigma_a + \sigma_b + \sigma_c$
$\sqrt{\sigma_b \sigma_c}$
$\sqrt{\sigma_a \sigma_b}$
$\sqrt{\sigma_a \sigma_c}$

Figure 1-35

frequency or cross range. Since the Fourier transform of a sum of terms is equal to the sum of the Fourier transforms of the individual terms, the complete spectrum is then a complex superposition of all the spectra, as shown for the three point targets in Figure 1-35. The resulting summation gives a zero Doppler or cross range peak proportional to total radar cross section, and a symmetrical distribution of other points about the zero point as expected for a real function transform.

From the three-point scatterer illustration of Figure 1-35, one might see the significant difference between coherent (amplitude and phase) and noncoherent (amplitude only) data in terms of coherent responses. The noncoherent response function for N points can be seen as the sum of N coherent response functions which combine in such a way that they cannot be unambiguously sorted if there are more than two points.

This concept can be extended to a wide-angle, narrowband, two-dimensional image. In an x-y grid, the coherent image of three points might appear as shown in Figure 1-36a, where a point response has been idealized in a simple approximation.

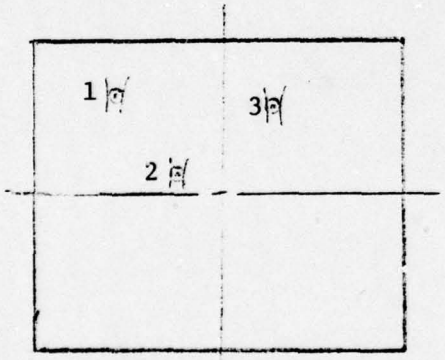

Figure 1-36a

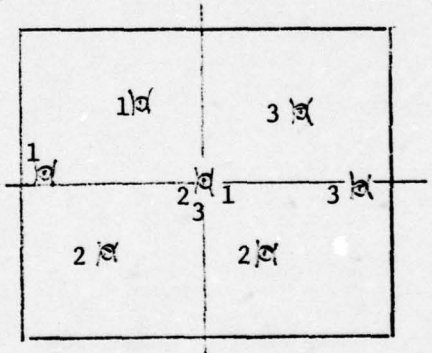

Figure 1-36b

If the same RCS data versus aspect angle is treated as an amplitude function without phase terms, but processed in the same manner as the coherent data, that is using (1-81), the resulting image will contain ambiguous responses. To see this, we note that each sum over i in (1-88) has the same form as (1-79) but with the center of rotation (point of zero phase in the body) shifted to y_k. Thus, the

two-dimensional, ambiguous images will also be repeated a number of times equal to the number of individual scatterers. This total set will be superimposed in the reference x-y plane with each independent scatterer taking its turn as the center of an individual, unambiguous image and weighting its own image set by its own amplitude. The resultant center of the composite image builds up to the highest amplitude since all of the points are coincident there as a result of this superposition. The resulting ambiguous image based on the unambiguous image of Figure 1-36a is shown Figure 1-36b.

Except for some very special cases that arise, the narrowband two-dimensional noncoherent imaging is not proposed as especially useful, particularly in light of the difficulties with coherent signals described in Section 1.4d. However, the concept should give a pictorial sense of the ambiguities that arise in the radar data when phase information is ignored.

For the sake of completeness, one might also consider the possibility of noncoherent wideband imaging. If bandwidth is added to the transmitted signal, giving a pulse shape, A(y), of unit amplitude, then the summation in the narrowband case just discussed for the total signal could be changed to

$$V_T(y) = \sum_i A(y - y_i)\, V_i e^{j2ky_i} \qquad (1\text{-}89)$$

The short pulse provides resolution of point scatterers in slant range. We can Fourier transform slant range cells of aspect data, using a short integration span as if forming a coherent image but using amplitude only data. The result will be a two-dimensional display showing the presence of more than one point in a slant-range resolution cell. For short spans, if more than one point exists in a resolution cell, then an amplitude modulation results. The narrowband results of (1-85) to (1-88) apply, but only to the points unresolved in an effective slant-range resolution cell. A slant range cell could then contain responses as were shown in Figure 1-35.

1.5 EXTENDED SURFACE RESPONSES

1.5a Representation of Continuous Surface Effects by Line Arrays of Points

When radar data are from aspect angles near the normal to a smooth surface of a target, a DTI plot or two-dimensional image tends to paint out a high amplitude specular response which extends the length of the surface in cross range. At these aspects, the current on the illuminated surface can be approximated by two times the value of the tangential incident magnetic field (physical optics). We can think of the smoothly varying current as a series of discrete but contiguous currents, as if they were from a line array of point targets. As the aspect angle of the surface changes, each of the point targets gives rise to a response in Doppler or cross range, and if the data are wideband the slant range to each point changes. For data near the normal, the Doppler response functions of each point overlap and the effect is to paint out the overall extent of the surface as shown in Figure 1-37. The resolution of the surface in slant-range is given approximately by the pulse width. Illustrations of two-dimensional wideband imaging of smooth surfaces are shown in Section 4.3a.

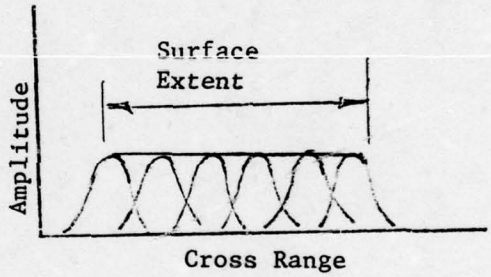

Figure 1-37

1.5b Integral Technique for Obtaining Radius Profile Estimates from Cross Range Responses at Specular Flash Aspects

Coherent processing of narrowband radar data has sometimes been based on an integral technique for estimating the radius of curvature of an axially symmetric target. The method is valid at specular aspects near the perpendicular to the symmetry axis and requires physical optics approximations to hold. Under these conditions, a Fourier transform of the amplitude and phase at specular aspects may give an estimate of radius profile. The processing is similar to that of a DTI plot except for minor modifications.

Under the limiting conditions stated, the physical optics formula for radar scattering approaches a Fourier transform integral form with a complex radius profile function as the main argument of the integral. From the inverse relationship, an approximate formula for the radius of curvature R(z) can be obtained as given in (1-90) where (z) is the position along the symmetry line:

$$R(z) \approx \frac{2}{\pi\lambda} \left| \int_{\theta} A(\theta)\, e^{j2k\theta z}\, d\theta \right|^2 \qquad (1\text{-}90)$$

The target response in (1-90) is given by

$$A(\theta) = \sqrt{\sigma(\theta)}\, e^{j\phi(\theta)} \qquad (1\text{-}91)$$

where σ is the radar cross section and $\phi(\theta)$ its phase.

For simply shaped smooth bodies obeying physical optics, the formula theoretically predicts body dimensions and unambiguously displays location and separation of major body features. For complicated bodies which are not rotationally symmetric and do not obey physical optics, the length and radius estimates obtained from the transform will be in error. The technique is sensitive to small changes in the RCS measurement such as calibration errors.

Plots of radius profile estimates are shown in Figures 1-38 and 1-39 for a small right circular cylinder and a cone-cylinder frustum. The data processed were from the General Dynamics narrowband model range discussed in Section 1.3d, where DTI plots for these models are shown. The profile estimates were made with and without a Hamming weight multiplying A(θ). The radius profiles which result from using unweighted data show considerable oscillation, whereas the use of a Hamming weight on the RCS data smooths the radius profile.

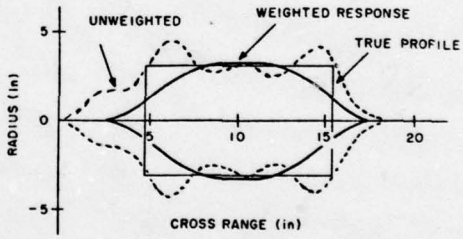

Figure 1-38

With or without weighting, the profiles are not exact because of the limiting approximations required to form the integral. The short conic section weighted response in the bottom of Figure 1-39 is low because the angle

integration span was reduced by the weighting, and the mainlobe of the RCS pattern of that section was not fully included in the integration. Inclusion of mainlobes can be considered a condition on the integration span. This inverse transform relationship has sometimes been called the "Blasberg approximation".

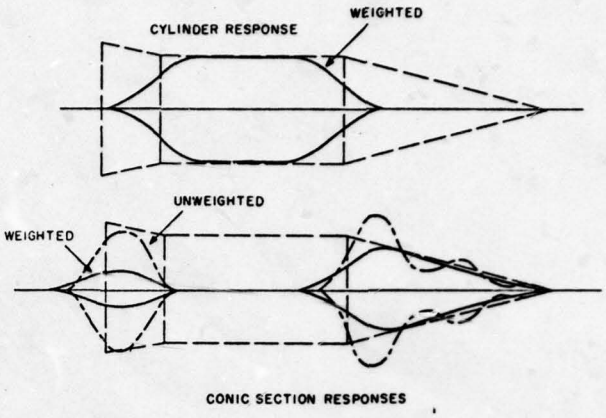

Figure 1-39

1.6 TRANSLATIONAL MOTION COMPENSATION

1.6a Range Smoothing

In the preceding discussions and those that follow, the important assumption is generally made that translational motion effects on the radar data have been removed in such a way that the data have become like those that would have been received from a target rotating about an axis passing through one target point fixed in slant range. This compensation is often made in space object tracking signals by using slant range from a metric data recording. The metric data are assumed to be a noisy representation of the distance to the target center of mass and are smoothed over significantly long averaging times relative to signal integration times. Compensation values are calculated from time delays corresponding to the smoothed range data. If the smoothed range to the target is R at some given time, and R was determined from an assumed propagation velocity c, then the corresponding time delay is $t_r = 2R/c$ (t_r may be given directly in some recordings). Then a phase compensation value may simply be given by $\phi_r = 2\pi f_o t_r$, where f_o is carrier frequency and ϕ_r may be subtracted from all the phase samples recorded for a set of data from one pulse transmission. Wideband amplitude-range sweeps may be aligned to follow the smooth range curve (if the real time tracking is not smooth enough) by calculating the residuals between smoothed and unsmoothed data and realigning the sweeps accordingly in a new data array.

Metric range data usually are measures of range tracking gate positions, the gates being positioned by attempts to follow either some reflection point on the target or some version of a centroid of the radar returns. Since an actual reflection center cannot generally be expected to exist at a mass center, nor can reflection effects across a target necessarily average out to make a mean position of the radar returns coincide with the mass center, metric range data can only approximate the path length to the mass center.

Smoothing of the range data may be accomplished by using restrictive parameter models, like a six-parameter Kepler orbit for a spherical earth, or other free-flight models with higher order perturbation effects taken into account. Range and angle data may be used together in available orbit or trajectory parameter estimation routines, giving heavier weights to the range data for best results. Increasing accuracy in the center of mass motion model will not necessarily remove the translational motion effects more accurately. There is the fundamental limitation, mentioned previously, that the original data are not necessarily based on an exact tracking of the center of mass. Thus smoothing may sometimes be accomplished well enough with simpler models, like fitting of a polynomial to the range data alone.

The range values that are used in the final compensation calculations should represent the true propagation path time delay, which does not necessarily correspond to the straight-line path between radar and target. Also, attention must be given to the number of significant digits used in range or time delay recordings and in the smoothing routines. It should be ensured that the smoothed range data will have a least significant digit equal to a small fraction of a half-wavelength, or finer.

Refractive bending in the troposphere will give errors in the true slant range if a straight-line distance is desired for true target position information, but for the one or two-dimensional image processing the refraction errored range, or true propagation path length, is the required value. For the troposphere, the time delay based on pulse position delays is applicable to calculate phase time delays. However, some difficulty may be encountered if

there is significant ionospheric refraction. The pulse delay (which is dependent on the group velocity) is different from the phase delay (which is dependent on the phase velocity) because of interactions within the ionospheric plasma. The difference between group time delay and phase time delay is dependent on an integrated electron density factor, which may be obtained from knowledge of the ionospheric profile along the propagation path. This is difficult to obtain accurately from models or sounding data. Alternately, if measurements of the differences in group time delay are made between two significantly different center frequencies reflected from the same target, then estimates of this integrated electron density factor may be made which can be used to calculate the phase and group delay differences at other frequencies. However calculated, an exact phase compensation for ionospheric delays requires data not directly obtainable from single frequency radar measurements. The ionospheric compensation may not always be necessary, but ignoring the effects may lead to Doppler frequency biases in the processed data or, in worst cases, to distortions causing loss of resolution in Doppler frequency.

In linear F-M pulse compression systems there is a range-Doppler ambiguity in pulse envelope positions which may require special handling, depending on the degree of the ambiguity. The pulse envelope returns in wideband systems should be aligned on the basis of the ambiguous total range-Doppler time delay positions, i.e., on the slant range which has not been compensated for the velocity error in the time delay. The phase compensation should be based on a velocity compensated time delay, i.e., the true time delay path length to the target.

1.6b Doppler Smoothing

Another means of phase compensation may be obtained with narrowband data if the sampling rate, as determined by the pulse repetition frequency (PRF), is high enough so that a gross Doppler frequency variation of the target may be estimated directly. Signals could be Fourier transformed without any phase compensation over time spans short enough to allow linear approximations for the gross translational motion, implying that the Doppler resolution cell would be wider than the relative Doppler spread between scattering points. The gross

velocity would be expected to change from one integration span to the next, and even move through the Doppler ambiguity intervals dependent on the PRF. However, if the variation is slow enough and the PRF is constant, the ambiguity may be readily resolvable through an obvious unfolding of the response functions in a series of DTI plots. If the PRF changes, then a range rate from the metric slant range curve may be useful in resolving the ambiguities. Also, a logic of correct positioning of smoothly changing responses may be invoked across PRF changes.

With the ambiguity resolved, the gross Doppler frequency data as a function of time may be smoothed in the manners suggested for slant range data, and an integration of the smoothed Doppler frequency function may be used for a phase compensation (the lack of an integration constant would not be significant). This integration could be easily accomplished if a polynomial model is used in the data smoother. The compensation from the Doppler data would give a true phase time delay correction rather than a group time delay.

1.6c Error Effects from Range or Doppler Smoothing

Minor errors in the estimate of a smoothed translational motion compensation from gross slant range or Doppler frequency data may result in little more than a slow bias drift in the overall image function across a series of integration spans during a track. A DTI display for narrowband data may have the responses drifting to one side or the other of an ambiguity window, with similar drifting effects of an RTI display of wideband data. Two-dimensional images may appear to drift in both directions.

More serious errors in the compensation would occur if the residual between the smoothed phase time delay estimate and the true value has significant quadratic or higher order coefficients. Then resolution will become poor in the Doppler response functions, which can be considered to be defocused. If other means of obtaining a better estimate are not possible, then an additional quadratic compensation term might be added to the first estimated function. The coefficient of the quadratic can be varied in a series of response calculations with the same data until the responses appear focused. If there are point

scatterers, this focused condition occurs at the coefficient value for which the point responses are highest in amplitude as well as narrowest. A similar tuning may be effected if just the carrier frequency term is slightly varied across some range of frequency deviation values. Corrections using more than one polynomial term would require searches in more than one dimension and could become quite time consuming.

With wideband data, a linear error term in the compensation residual function can cause defocusing in a two-dimensional image. However, this type of variation should be fairly obvious in an RTI plot, which can then be used to make additional corrections (for linear or higher order terms).

1.6d Point Scatterer Compensation

In wideband data, the most direct means of removing translational motion is to track an isolated point scatterer as a function of time in some version of an RTI display and align all sweeps on the peak of this point response. The phase measured under the peak of the pulse from this point in any one sweep can be subtracted from all the phases in that sweep. Thus, the reference point will be forced to have a zero phase angle, independent of target rotation angle, and that point will be the effective center of rotation in any imaging results. For a rotating set of points, the point with zero phase angle may be defined as the center of rotation from the previous analyses.

The point reference technique is not considered as general as the data smoothing technique because a truly isolated reference point cannot be guaranteed to be always present on various types of targets. If an isolated reference point is present at some aspect angles, such a point may not be seen at other aspect angles. If different points do seem to appear isolated at different aspects, then the different points may be made to become the centers of rotation in turn, and sets of images might be suitably adjusted through a visual correlation.

Section 2 — Review of Mathematics

SECTION 2

REVIEW OF MATHEMATICS

2.1 VECTOR COMPONENTS

A vector may be defined as a quantity that can be represented by a directed line segment. In this discussion, vector quantities will be denoted by a letter symbol capped with a mark, such as $\vec{U}$. In the Cartesian coordinates of Figure 2-1, the vector $\vec{U}$ is specified by components X_u, Y_u, Z_u, along the orthogonal X, Y, and Z axes.

The magnitude of a vector is a scalar quantity and will be represented by the same symbol as the vector, but without the cap ($|\vec{U}| = U$). The magnitude of $\vec{U}$ in Figure 2-1 can be expressed as

$$|\vec{U}| = U = \sqrt{X_u^2 + Y_u^2 + Z_u^2} \qquad (2\text{-}1)$$

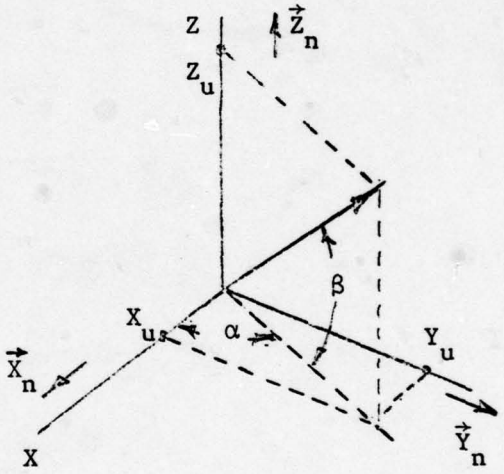

Figure 2-1

The unit direction vector will specify only the direction of a vector and not its length (assuming it is not unity). It may be considered a normalized version of the original vector. Unit direction vectors may be used to specify the directions of coordinate axes, such as the orthogonal vectors $\vec{X}_n$, $\vec{Y}_n$, $\vec{Z}_n$, in Figure 2-1. The vector $\vec{U}$ may then be described by

$$\vec{U} = \vec{X}_n X_u + \vec{Y}_n Y_u + \vec{Z}_n Z_u \qquad (2\text{-}2)$$

The unit vector direction of $\vec{U}$ may be expressed as

$$\vec{U}_n = \frac{\vec{U}}{U} = \vec{X}_n \frac{X_u}{U} + \vec{Y}_n \frac{Y_u}{U} + \vec{Z}_n \frac{Z_u}{U} \qquad (2\text{-}3)$$

where U was given in (2-1).

A vector may be specified in another form by the magnitude plus two angles, such as the azimuthal angle, α, and elevation angle, β, in Figure 2-1. With these coordinates, the vector components in (2-2) become

$$\begin{aligned} X_u &= U\cos\beta\ \cos\alpha \\ Y_u &= U\cos\beta\ \sin\alpha \\ Z_u &= U\sin\beta \end{aligned} \tag{2-4}$$

2.2 COORDINATE ROTATIONS

Vectors may be specified in one coordinate system which, itself, is rotated relative to another coordinate system, and the relationships between the two systems in terms of vector components may be required. A completely arbitrary relative orientation of coordinate systems may be specified through three rotation angles, sometimes called Eulerian angles. These rotations will be illustrated one step at a time. First, let the X-Y-Z system of Figure 2-1 be rotated through an angle ϕ about the Z-axis so that X and Y have new positions at X_1 and Y_1, as shown in Figure 2-2. Then it may be seen that the projections of a vector onto the new axes, such as may be specified by a new set for $\vec{U}$, X_{1u}, Y_{1u}, Z_{1u}, can be used to determine the corresponding X_u, Y_u, Z_u components by combining the component projections of X_{1u} and Y_{1u}. The equations that result for these relationships are the following, where the subscript u is omitted to simplify the notations,

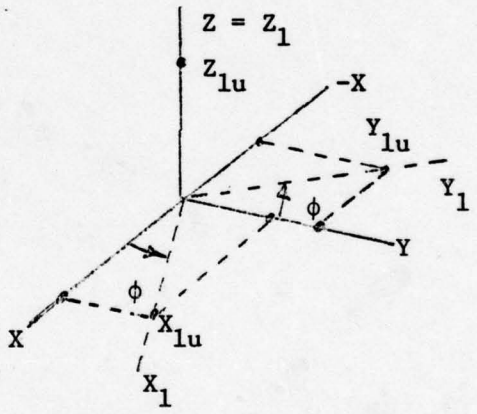

Figure 2-2

$$\begin{aligned} X &= X_1\cos\phi - Y_1\sin\phi \\ Y &= X_1\sin\phi + Y_1\cos\phi \\ Z &= Z_1 \end{aligned} \tag{2-5}$$

The set of equations in (2-6) may be expressed in matrix notation as

$$\begin{bmatrix} X \\ Y \\ Z \end{bmatrix} = \begin{bmatrix} \cos\phi & -\sin\phi & 0 \\ \sin\phi & \cos\phi & 0 \\ 0 & 0 & 1 \end{bmatrix} \begin{bmatrix} X_1 \\ Y_1 \\ Z_1 \end{bmatrix} \tag{2-6}$$

The second rotation will be through an angle θ about the Y_1 axis to give a second new set of axes, X_2, Y_2, Z_2, as illustrated in Figure 2-3. The relationships between set 1 and set 2 can then be derived in a manner similar to that for the first rotation to give

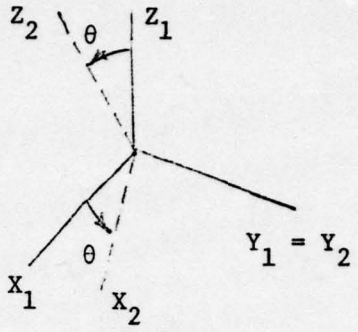

Figure 2-3

$$\begin{bmatrix} X_1 \\ Y_1 \\ Z_1 \end{bmatrix} = \begin{bmatrix} \cos\theta & 0 & \sin\theta \\ 0 & 1 & 0 \\ -\sin\theta & 0 & \cos\theta \end{bmatrix} \begin{bmatrix} X_2 \\ Y_2 \\ Z_2 \end{bmatrix} \tag{2-7}$$

The final rotation will be through an angle ψ about the Z_2 axis as shown in Figure 2-4. The resulting third new coordinate system is related to the second new system through

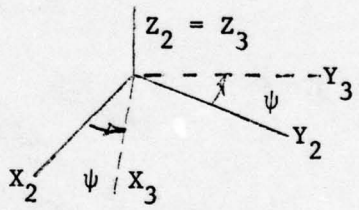

Figure 2-4

$$\begin{bmatrix} X_2 \\ Y_2 \\ Z_2 \end{bmatrix} = \begin{bmatrix} \cos\psi & -\sin\psi & 0 \\ \sin\psi & \cos\psi & 0 \\ 0 & 0 & 1 \end{bmatrix} \begin{bmatrix} X_3 \\ Y_3 \\ Z_3 \end{bmatrix} \tag{2-8}$$

The relationship between the original X-Y-Z system and the final X_3-Y_3-Z_3 system is obtained by substituting (2-8) into the right hand side of (2-7) and (2-7) into (2-6) to give

$$\begin{bmatrix} X \\ Y \\ Z \end{bmatrix} = \begin{bmatrix} \cos\phi & -\sin\phi & 0 \\ \sin\phi & \cos\phi & 0 \\ 0 & 0 & 1 \end{bmatrix} \begin{bmatrix} \cos\theta & 0 & \sin\theta \\ 0 & 1 & 0 \\ -\sin\theta & 0 & \cos\theta \end{bmatrix} \begin{bmatrix} \cos\psi & -\sin\psi & 0 \\ \sin\psi & \cos\psi & 0 \\ 0 & 0 & 1 \end{bmatrix} \begin{bmatrix} X_3 \\ Y_3 \\ Z_3 \end{bmatrix} \tag{2-9a}$$

and completing the matrix multiplications

$$\begin{bmatrix} X \\ Y \\ Z \end{bmatrix} = \begin{bmatrix} (\cos\phi\cos\theta\cos\psi - \sin\phi\sin\psi) & (-\cos\phi\cos\theta\sin\psi - \sin\phi\cos\psi) & (\cos\phi\sin\theta) \\ (\sin\phi\cos\theta\cos\psi + \cos\phi\sin\psi) & (-\sin\phi\cos\theta\sin\psi + \cos\phi\cos\psi) & (\sin\phi\sin\theta) \\ (-\sin\theta\cos\psi) & (\sin\theta\sin\psi) & (\cos\theta) \end{bmatrix} \begin{bmatrix} X_3 \\ Y_3 \\ Z_3 \end{bmatrix} \tag{2-9b}$$

Thus, a rotation transformation matrix has been derived which relates two arbitrarily oriented coordinate sets. In more compact forms,

$$[U] = \begin{bmatrix} X \\ Y \\ Z \end{bmatrix} = \begin{bmatrix} a_{11} & a_{12} & a_{13} \\ a_{21} & a_{22} & a_{23} \\ a_{31} & a_{32} & a_{33} \end{bmatrix} \begin{bmatrix} X_3 \\ Y_3 \\ Z_3 \end{bmatrix} = [A]\,[U_3] \tag{2-10}$$

where the column matrix [U] represents the vector $\vec{U}$ in the original coordinate system and $[U_3]$ represents $\vec{U}$ in the final system after three rotations. The components of the square matrix A, a_{11}, a_{12}, etc., are specified by the corresponding terms in (2-9b).

An important property of a rotation transformation matrix such as [A] is that the final system may be obtained from the first system through a transpose of the transformation matrix, i.e., the inverse of A is equal to the transpose of A. Thus,

$$[U_3] = [A]^T[U] \tag{2-11}$$

or

$$\begin{bmatrix} X_3 \\ Y_3 \\ Z_3 \end{bmatrix} = \begin{bmatrix} a_{11} & a_{21} & a_{31} \\ a_{12} & a_{22} & a_{32} \\ a_{13} & a_{23} & a_{33} \end{bmatrix} \begin{bmatrix} X \\ Y \\ Z \end{bmatrix} \qquad (2\text{-}12)$$

This rule applies to a transformation matrix for any one rotation, such as the matrices of (2-6), (2-7), and (2-8), as well as to matrices representing second and third rotations.

2.3 MULTIPLE VECTOR ALGEBRA

2.3a Addition and Subtraction

Multiple vectors may be summed in any order or combination:

$$\vec{A} + \vec{B} + \vec{C} = \vec{A} + (\vec{B}+\vec{C}) = (\vec{A}+\vec{B}) + \vec{C} = \vec{C} + \vec{B} + \vec{A} \qquad (2\text{-}13)$$

The summations imply that the corresponding components are added. Using the notation of Figure 2-1,

$$\vec{A} + \vec{B} + \vec{C} = \vec{X}_n\,(A_x + B_x + C_x) + \vec{Y}_n(A_y + B_y + C_y) + \vec{Z}_n(A_z + B_z + C_z) \qquad (2\text{-}14)$$

A mean vector, $\vec{V}_m$, can be obtained by averaging components, which may be represented in terms of a vector series $\vec{U}_i$ as

$$\vec{V}_m = \sum_{i=1}^{N} \frac{\vec{U}_i}{N} \qquad (2\text{-}15)$$

A sometimes useful relation is the mean direction between unit vectors, such as a set $\vec{U}_{ni}$. In this case, the resultant average vector must be normalized to give another unit vector, $\vec{V}_{mn}$, which will represent the mean direction, such as in

$$\vec{V}_m = \frac{1}{N} \sum_{i=1}^{N} \vec{U}_{ni}$$

$$\vec{V}_{mn} = \frac{\vec{V}_m}{|\vec{V}_m|} \qquad (2\text{-}16)$$

2.3b Dot Products

A scalar or dot product of two vectors is specified by the notation $\vec{A}\cdot\vec{B}$ and represents the operation

$$\vec{A}\cdot\vec{B} = \vec{B}\cdot\vec{A} = A_xB_x + A_yB_y + A_zB_z = AB\cos\theta \qquad (2\text{-}17)$$

According to (2-17), the dot product is equal to the sum of the products of components and is equal to the product of the two magnitudes and the cosine of the angle, θ, between the two vectors.

As an example of one application, the angle between the radar line-of-sight as specified by unit vector $\vec{R}$, and a body symmetry axis, as specified by unit vector $\vec{S}$ illustrated in Figure 2-5, may be obtained through a dot product as

$$\theta = \arccos\ (\vec{R}\cdot\vec{S}) \qquad (2\text{-}18)$$

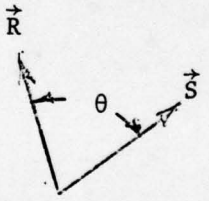

Figure 2-5

In other applications, the dot product may be useful to obtain the projection of one vector onto another. For example, the relative slant range, ΔR, between a pair of target points separated by vector distance $\vec{L}$ may be obtained as

$$\Delta R = L\cos\theta = \vec{R}\cdot\vec{L} \qquad (2\text{-}19)$$

where $\vec{R}$ is a unit vector, as sketched in Figure 2-6.

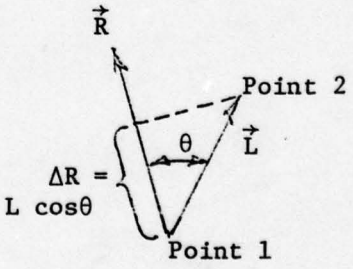

Figure 2-6

If one of the two vectors in a dot product is the sum of vectors, then component dot products may be summed, for example

$$\vec{A}\cdot(\vec{B} + \vec{C}) = \vec{A}\cdot\vec{B} + \vec{A}\cdot\vec{C} \tag{2-20}$$

2.3c Cross Products

A cross product results in another vector and is specified through the notation

$$\vec{A} \times \vec{B} = \vec{M} \tag{2-21}$$

where

$$|\vec{M}| = AB\sin\theta \tag{2-22}$$

The direction of $\vec{M}$ is orthogonal to $\vec{A}$ and $\vec{B}$, and θ is the angle between $\vec{A}$ and $\vec{B}$, as sketched in Figure 2-7. Changing the order of the multiplication changes the sign of the resultant

$$\vec{A} \times \vec{B} = -\vec{B} \times \vec{A} \tag{2-23}$$

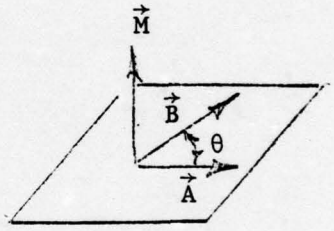

Figure 2-7

In terms of its components, the cross product may be specified by the determinant formed from the axis unit direction vectors $\vec{X}_n$, $\vec{Y}_n$, $\vec{Z}_n$ and the components according to

$$\vec{A} \times \vec{B} = \begin{vmatrix} \vec{X}_n & \vec{Y}_n & \vec{Z}_n \\ A_x & A_y & A_z \\ B_x & B_y & B_z \end{vmatrix} \tag{2-24}$$

or

$$\vec{A} \times \vec{B} = \vec{X}_n(A_yB_z - B_yA_z) + \vec{Y}_n(A_zB_x - A_xB_z) + \vec{Z}_n(A_xB_y - A_yB_x) \tag{2-25}$$

A plane surface orientation may be defined by two lines in the plane, which may be specified by vector directions $\vec{A}$ and $\vec{B}$, as was illustrated in Figure 2-7. Then, the normal unit vector, $\vec{P}_n$, to the plane will be a more compact definition of the plane orientation and may be obtained from a normalized cross product

$$\vec{P}_n = \frac{\vec{A} \times \vec{B}}{|\vec{A} \times \vec{B}|} \tag{2-26}$$

Other rules sometimes useful for multiple vectors are

$$\vec{A} \times (\vec{B} + \vec{C}) = \vec{A} \times \vec{B} + \vec{A} \times \vec{C} \tag{2-27}$$

$$\vec{A} \cdot (B \times C) = (\vec{A} \times \vec{B}) \cdot \vec{C} = \vec{C} \cdot (\vec{A} \times \vec{B}) = \vec{B} \cdot (\vec{C} \times \vec{A}) \tag{2-28}$$

$$\vec{A} \times (\vec{B} \times \vec{C}) = (\vec{A} \cdot \vec{C})\vec{B} - (\vec{A} \cdot \vec{B})\vec{C} \tag{2-29}$$

$$(\vec{A} \times \vec{B}) \cdot (\vec{C} \times \vec{D}) = (\vec{A} \cdot \vec{C})\ (\vec{B} \cdot \vec{D}) - (\vec{A} \cdot \vec{D})\ (\vec{B} \cdot \vec{C}) \tag{2-30}$$

2.3d Time Derivatives of Vectors

If the components of a vector are time varying, then the derivative of the vector may be obtained from the derivatives of the components. If

$$\vec{U} = \vec{X}_n X_u + \vec{Y}_n Y_u + \vec{Z}_n Z_u$$

then

$$\dot{\vec{U}} = \frac{d\vec{U}}{dt} = \vec{X}_n \frac{dX_u}{dt} + \vec{Y}_n \frac{dY_u}{dt} + \vec{Z}_n \frac{dZ_u}{dt} \tag{2-31}$$

The derivative of a dot product may be obtained by

$$\frac{d}{dt}(\vec{A} \cdot \vec{B}) = \vec{A} \cdot \frac{d\vec{B}}{dt} + \vec{B} \cdot \frac{d\vec{A}}{dt} \tag{2-32}$$

The derivative of a cross product can be obtained as

$$\frac{d}{dt}(\vec{A} \times \vec{B}) = \vec{A} \times \frac{d\vec{B}}{dt} + \frac{d\vec{A}}{dt} \times \vec{B} \tag{2-33}$$

If a vector is changing with time, the derivative of its unit direction vector can be used to determine a rotation vector. For instance, if radar line-of-sight unit direction vector $\vec{R}$ is changing, then $\frac{d\vec{R}}{dt}$ will be a vector orthogonal to $\vec{R}$ with a magnitude equal to the instantaneous rotation rate. This may be seen from the sketch in Figure 2-8, where a differential change moves $\vec{R}$ from $\vec{R}_1$ to $\vec{R}_2$ through an angle $\Delta\phi$. Since the magnitude of $|\Delta\vec{R}| \approx R\Delta\phi$, the approximate derivative is $|\frac{\Delta\vec{R}}{\Delta t}| \simeq R\,\frac{\Delta\phi}{\Delta t}$, and since R = 1,

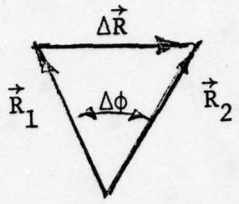

Figure 2-8

$|\frac{\Delta R}{\Delta t}| \approx \frac{\Delta\phi}{\Delta t}$, or in the limit, $|\frac{d\vec{R}}{dt}| = \frac{d\phi}{dt}$. The direction of $\frac{d\vec{R}}{dt}$ is orthogonal to $\vec{R}$ since $\frac{d}{dt}(\vec{R}\cdot\vec{R}) = 0 = 2\vec{R}\cdot\frac{d\vec{R}}{dt}$, from the rule (2-32), which cannot be true unless $\frac{d\vec{R}}{dt}$ is orthogonal to $\vec{R}$. An instantaneous rotation vector, $\vec{\Omega}_R$, for the changing $\vec{R}$ may then be obtained using a cross product

$$\vec{\Omega}_R = \vec{R} \times \frac{d\vec{R}}{dt} \tag{2-34}$$

where $\vec{\Omega}_R$ is parallel to the instantaneous axis of rotation of $\vec{R}$ and has a magnitude equal to the rate of rotation.

2.4 MATRIX OPERATIONS

Matrix formulations were involved in the previous sections on vector computations, which indicated some of the associations and interchanges of the two types of notations. A few elementary matrix rules will be briefly explained. An N-dimensional vector may be specified by a column matrix, such as

$$A = \begin{bmatrix} a_1 \\ a_2 \\ a_3 \\ \cdot \\ \cdot \\ \cdot \end{bmatrix} \tag{2-35}$$

The transpose of this matrix is a row matrix

$$A^T = [a_1 \quad a_2 \quad a_3 \quad . \; . \; .]$$

The equivalent of a vector dot product of two column matrixes, A and B, is the operation

$$B^T A = A^T B = a_1 b_1 + a_2 b_2 + a_3 b_3 \; . \; . \; . \tag{2-36}$$

or

$$B^T A = \sum_i a_i b_i$$

The sum of the square of a series may thus be stated in matrix notation as

$$\sum_i (a_i)^2 = A^T A \tag{2-37}$$

From (2-37), the multiplication of a column matrix that is M units long by a row matrix M units long results in a single matrix that consists of one unit. The rule for multiplying multidimensional pairs of matrices is that the rows of the first matrix are multiplied by the columns of the second matrix to form a third matrix. Thus, for a matrix multiplication to be valid, there must be as many elements in the rows of the first matrix as there are elements in the columns of the second matrix. If the first matrix has M rows and the second matrix as N columns, then the final matrix will have M rows and N columns, regardless of the number of columns in the first matrix or rows in the second matrix. As an example, let

$$A = \begin{bmatrix} a_{11} & a_{12} & a_{13} \\ a_{21} & a_{22} & a_{23} \end{bmatrix} = \begin{bmatrix} A_1 \\ A_2 \end{bmatrix}$$

$$B = \begin{bmatrix} b_{11} & b_{12} & b_{13} \\ b_{21} & b_{22} & b_{23} \\ b_{31} & b_{32} & b_{33} \end{bmatrix} = [B_1 \quad B_2 \quad B_3] \tag{2-38}$$

where A_1 represents the row $[a_{11} \quad a_{12} \quad a_{13}]$ and B_1 represents the column $[b_{11} \quad b_{21} \quad b_{31}]^T$, etc. Then, multiplying rows of A times columns of B gives the following

$$AB = \begin{bmatrix} A_1B_1 & A_1B_2 & A_1B_3 \\ A_2B_1 & A_2B_2 & A_2B_3 \end{bmatrix} \tag{2-39}$$

where $A_1B_1 = a_{11}b_{11} + a_{12}b_{21} + a_{13}b_{31}$ in the dot product sense of (2-36) and other terms of AB are formed from corresponding summations. In the previous derivation of vector rotation relationships, (2-9a) shows a multiplication of three 3 x 3 matrices in the form ABC. The products may be taken in any combination, but the order must be maintained according to

$$ABC = [AB][C] = A[BC] \tag{2-40}$$

Each combination in (2-40) results in a 3 x 3 matrix, so the resultant ABC is a 3 x 3 matrix as shown in (2-9b).

A transpose of a general matrix implies that rows and columns are interchanged, as in

$$\begin{bmatrix} a_{11} & a_{12} & a_{13} \\ a_{21} & a_{22} & a_{23} \end{bmatrix}^T = \begin{bmatrix} a_{11} & a_{21} \\ a_{12} & a_{22} \\ a_{13} & a_{23} \end{bmatrix} \tag{2-41}$$

A square matrix, A, may have an inverse designated, A^{-1}, such that the product

$$A^{-1}A = [I] \tag{2-42}$$

where I is a diagonal matrix with unity elements along the diagonal and zeroes everywhere else. An example of a 3 x 3 unit matrix (or identity matrix) is

$$[I]_3 = \begin{bmatrix} 1 & 0 & 0 \\ 0 & 1 & 0 \\ 0 & 0 & 1 \end{bmatrix} \tag{2-43}$$

A square matrix times a unit matrix is equal to the square matrix

$$[A]\,[I] = [I]\,[A] = [A] \tag{2-44}$$

In general, a square matrix is called diagonal if all of its elements except those along the diagonal are zero, and the diagonal elements are not necessarily equal in this definition.

A three-variable set of independent linear algebraic equations may be stated as

$$c_1 X_{1i} + c_2 X_{2i} + c_3 X_{3i} = b_i \tag{2-45}$$

where the index will run from i = 1 to 3, and if c_1, c_2, c_3 are unknown constants based on measured or known values of X_{1i}, X_{2i}, X_{3i}, and b_i, then the unknown values could be solved from three equations represented in (2-45). The matrix form of (2-45) would be

$$\begin{bmatrix} X_{11} & X_{21} & X_{31} \\ X_{12} & X_{22} & X_{32} \\ X_{13} & X_{23} & X_{33} \end{bmatrix} \quad \begin{bmatrix} c_1 \\ c_2 \\ c_3 \end{bmatrix} = \begin{bmatrix} b_1 \\ b_2 \\ b_3 \end{bmatrix} \tag{2-46}$$

which could be represented by a compact form

$$[X]\,[C] = [b] \tag{2-47}$$

where the terms in (2-47) should be readily identifiable with those in (2-46). There is no process for the equivalent of algebraic division with matrices; however, the inverse may be used in a somewhat similar fashion, although the operation is still a multiplication. Thus, the solution for [C] is obtained by using the matrix inverse of [X], observing the rules of multiplying in the proper order, and noting that $[X]^{-1}[X] = [X][X]^{-1} = [I]$. Therefore,

$$[X]^{-1}\,[X]\,[C] = [X]^{-1}\,[b] \tag{2-47}$$

or

$$[C] = [X]^{-1}\,[b]$$

There are several methods for inverting a matrix to obtain $[X]^{-1}$ which are described in a variety of matrix algebra textbooks. Most computer libraries have matrix inversion algorithms which can be used by the more practical analyst without concern for the details of operation. The greater concern is whether the matrix inverse exists (i.e., is not singular), and this depends on the nature of the data set used to form the matrix. In practical computations, although a matrix may theoretically have an inverse, the quantities may be of such a form that computer round-off limitations may make the matrix inverse meaningless. Standard computer algorithms usually have tests for such singularity conditions.

In the very special case of rotation matrices, such as those of (2-9a) and (2-9b), the inverse was equal to the transpose, and these are called orthogonal matrices, i.e., if $A^{-1} = A^T$ then $AA^T = [I]$.

Other matrix operations which may be useful, where A and B are matrices of the proper orders, are

$$A + B = B + A \tag{2-48}$$

If m is a constant or scalar quantity,

$$m \begin{bmatrix} a_{11} & a_{12} \\ a_{21} & a_{22} \end{bmatrix} = \begin{bmatrix} ma_{11} & ma_{12} \\ ma_{21} & ma_{22} \end{bmatrix} \tag{2-49}$$

$$m[A + B] = mA + mB \tag{2-50}$$

$$[mA]^{-1} = \frac{1}{m} [A]^{-1} \tag{2-51}$$

$$[A]\ [B + C] = AB + AC \tag{2-52}$$

$$\frac{dA}{dt} = \frac{d}{dt} \begin{bmatrix} a_{11} & a_{12} \\ a_{21} & a_{22} \end{bmatrix} = \begin{bmatrix} \frac{da_{11}}{dt} & \frac{da_{12}}{dt} \\ \frac{da_{21}}{dt} & \frac{da_{22}}{dt} \end{bmatrix} \tag{2-53}$$

$$\frac{d}{dt}[AB] = \left[\frac{dA}{dt}\right][B] + [A]\left[\frac{dB}{dt}\right] \tag{2-54}$$

If A = B, then, in general,

$$\frac{dAA}{dt} \neq 2A\frac{dA}{dt} \tag{2-55}$$

since the order of multiplications is not preserved.

$$[AB]^{-1} = B^{-1}A^{-1} \tag{2-56}$$

$$[AB]^{T} = B^{T}A^{T} \tag{2-57}$$

Section 3 — Range and Range Rate Relationships for Complex Motion

SECTION 3

RANGE AND RANGE RATE RELATIONSHIPS FOR COMPLEX MOTION

3.1 REVIEW OF FREE RIGID BODY DYNAMICS

If no torques act on a rigid-body target, its angular momentum will remain constant according to the principle of conservation of angular momentum. Angular motion about the center of mass will be constrained to certain modes dependent on the target's moments of inertia and the conditions when torques stopped acting.

Assuming an x-y-z coordinate system with an origin at the mass center, the moment of inertia about the x-axis through the center of mass may be defined by the volume integral

$$I_{xx} = \int_v r^2 \rho \, dx \, dy \, dz \tag{3-1}$$

where $r^2 = y^2 + z^2$ and ρ is the mass density function. For I_{yy}, (3-1) may be modified with $r^2 = z^2 + x^2$, and I_{zz}, $r^2 = x^2 + y^2$. A cross moment or product of inertia between the x and y axes may be defined as

$$I_{xy} = \int_v (xy) \rho \, dx \, dy \, dz \tag{3-2}$$

For I_{yz} and I_{zx} the product in parenthesis is correspondingly changed. The total angular momentum, $\vec{H}$, of the body may be obtained in terms of rotational velocity components, ω_x, ω_y, ω_z, about the three axes and the moments and products of inertia as defined in (3-1) and (3-2) according to

$$\begin{bmatrix} H_x \\ H_y \\ H_z \end{bmatrix} = \begin{bmatrix} I_{xx} & -I_{xy} & -I_{xz} \\ -I_{yx} & I_{yy} & -I_{yz} \\ -I_{zx} & -I_{zy} & I_{zz} \end{bmatrix} \begin{bmatrix} \omega_x \\ \omega_y \\ \omega_z \end{bmatrix} \tag{3-3}$$

where H_x, H_y, and H_z are the angular momentum components. The moment of inertia matrix is square as can be seen in (3-3), and is symmetrical as may be inferred from (3-2), for example $I_{xy} = I_{yx}$.

It can be shown that in any rigid body a set of axis orientations can be found in which the products of inertia are zero, i.e., the inertia matrix may be diagonalized, and the moments of inertia about these axes are called the <u>principal moments</u>. If x-y-z are principal axes (3-3) becomes

$$\begin{bmatrix} H_x \\ H_y \\ H_z \end{bmatrix} = \begin{bmatrix} I_{xx} & 0 & 0 \\ 0 & I_{yy} & 0 \\ 0 & 0 & I_{zz} \end{bmatrix} \begin{bmatrix} \omega_x \\ \omega_y \\ \omega_z \end{bmatrix} \qquad (3\text{-}4)$$

The simplest mode of target rotation is a simple rotation about one of the principal axes, implying a single rotation rate. A torque free target cannot simply rotate about an axis other than one of the principal moment axes. Objects that have more complex modes of rotational motion in an initial state but lose energy through various means tend to approach a state of simple rotation about the axis having the greatest moment of inertia.

The principal moment axes of a body with an axially symmetrical mass distribution, like a solid cylinder, include the axis of symmetry. The other two principal axes are then orthogonal to the symmetry axis but their locations are ambiguous and the moments of inertia about these two axes are equal. The sphere is a special case for which all three principal axis locations are ambiguous and the three principal moments of inertia are equal.

Let the principal moment of inertia about an axial symmetry axis be labeled I_S, and the principal moment about an axis orthogonal to the symmetry axis be I_T. An example of such as object which may be of interest is a solid circular cylinder of radius r, length L and total mass M for which the principal moments and their ratio may be shown to be

$$I_S = M\, r^2/2 \qquad (3\text{-}5)$$

(cylinder)

$$I_T = M(3\, r^2 + L^2)/12$$

$$I_S/I_T = 6\, r^2/(3\, r^2 + L^2)$$

A second object of interest might be a singly truncated, right circular, solid cone, with base radius r and altitude or length along the symmetry axis equal to L, for which

$$I_S = 3\,M\,r^2/10$$

$$\text{(cone)} \qquad I_T = 3\,M(L^2 + 4\,r^2)/80 \qquad (3\text{-}6)$$

$$I_S/I_T = 8\,r^2/(L^2 + 4\,r^2)$$

Relative rotation rates of axially symmetrical bodies are dependent on the ratios of the moments of inertia, as will be shown.

A freely rotating symmetrical body has a general mode of motion which can be described as a "spin" of the body at a rate ω_S about the symmetry axis and a rotation or "precession" of the symmetry axis about the total angular momentum vector with a precession rate ω_p while a constant precession angle, θ, is maintained by the spin axis with respect to the total angular momentum vector. Thus, the spin axis sweeps out a cone about the momentum vector. The relationship between these three variables and the moments of inertia will be derived in the following analysis.

Assume that two principal moments of the body are equal to I_T which may be unequal to the third principal moment I_S, as sketched in Figure 3-1, where the symmetry or "spin" axis direction is defined by $\vec{S}$, and the I_T axis might be called the "tumble" axis. If this body is in a steady state of motion, then its total angular momentum, $\vec{H}$, does not change; i.e., $d\vec{H}/dt = 0$. At some instant in time, let the body be simply rotating about its symmetry axis with a rate ω_S at an arbitrary angle, θ, with respect to a z-axis, as sketched in Figure 3-2.

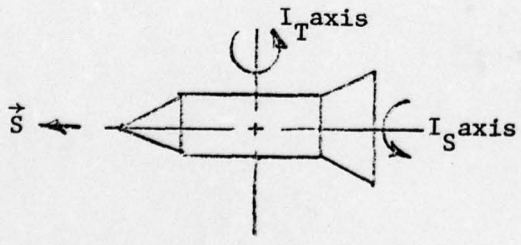

Figure 3-1

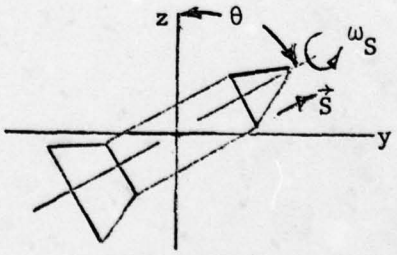

Figure 3-2

Then this body will have angular momentum $\vec{H}_S$ with components along the z- and y-axis as sketched in Figure 3-3, where

$$|\vec{H}_{Sz}| = I_S\omega_S \cos\theta$$
$$|\vec{H}_{Sy}| = I_S\omega_S \sin\theta \qquad (3\text{-}7)$$

The Figure 3-3 conditions are steady-state since $\vec{H}_S$, the total angular momentum, is not changing.

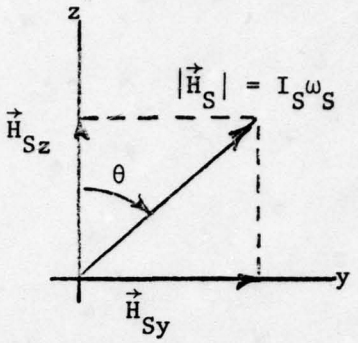

Figure 3-3

As a different condition, let the symmetry axis, $\vec{S}$, rotate about the z-axis at a constant rate, ω_p, while maintaining a constant angle, θ, and letting ω_S be zero. Then $\vec{\omega}_p$ has components along the I_S and I_T axes as shown in Figure 3-4. The angular momentum due to ω_p can be determined for one instant in time, as shown in Figure 3-5, by using the components along the body principal axes as formed in Figure 3-4. The magnitudes of the resulting compnents are

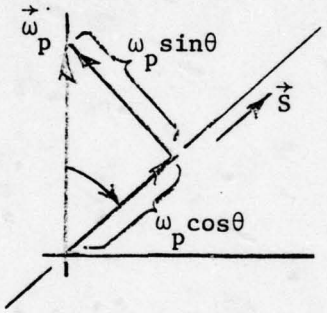

Figure 3-4

$$|\vec{H}_{Sp}| = I_S\omega_p\cos\theta$$
$$|\vec{H}_{Tp}| = I_T\omega_p\sin\theta \qquad (3\text{-}8)$$

which then give components along the y-axis, which are opposite in sign, and which have magnitudes

$$|\vec{H}_{Tpy}| = I_T\omega_p\sin\theta\cos\theta$$
$$|\vec{H}_{Spy}| = I_S\omega_p\sin\theta\cos\theta \qquad (3\text{-}9)$$

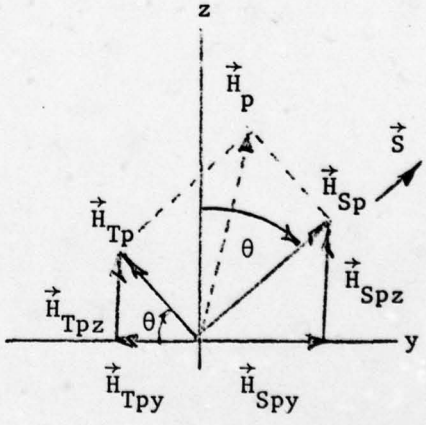

Figure 3-5

Now the total angular momentum, $\vec{H}_p$, due to $\vec{\omega}_p$ is the sum of $\vec{H}_{Sp}$ and $\vec{H}_{Tp}$ and is not, in the general case, parallel to the z-axis, as illustrated in Figure 3-5. Stated in another way, the two components in (3-9) are not equal in the general case. Consequently, $\vec{H}_p$ must change with time if a constant rate of ω_p is maintained, which requires a torque. However, if the spin about $\vec{S}$ is reintroduced, then the angular momentum, $\vec{H}_{Sy}$, from Figure 3-3 might be added to cancel out the y-axis components due to ω_p. Thus the resultant total angular momentum would appear only along the z-axis which would not require a change in total angular momentum with time. This cancellation of y-axis components can be obtained if

$$\vec{H}_{Tpy} + \vec{H}_{Spy} + \vec{H}_{Sy} = 0 \tag{3-10}$$

From Figures 3-3 and 3-5 and corresponding quantities in (3-7) and (3-9), (3-10) leads to

$$-I_T\omega_p \sin\theta \cos\theta + I_S\omega_p \sin\theta \cos\theta + I_S\omega_S \sin\theta = 0 \tag{3-11}$$

Combining terms yields

$$I_T\omega_p \cos\theta = I_S(\omega_p \cos\theta + \omega_S) \tag{3-12}$$

or

$$\frac{\omega_S}{\omega_p} = \cos\theta \left[\frac{I_T}{I_S} - 1\right] \tag{3-13}$$

Equation (3-13) gives the general conditions required for free rotation of an axially symmetrical body (or any body with two, equal, principal moments). As can be seen, the relationships between the two angular rates and the precession angle are dependent on the ratio of moments of inertia, for which cylinder and cone examples have been given in (3-5) and (3-6).

The spin rate, ω_S, in (3-13) is not the instantaneous total rotation rate about the symmetry axis. The total instantaneous rotation vector is determined, by the sum of $\vec{\omega}_p$ and $\vec{\omega}_S$. The component of this total rotation vector along the symmetry axis can be seen to have a magnitude

$$\omega_{ST} = \omega_S + \omega_p \cos\theta \tag{3-14}$$

In terms of this total spin rate, by substituting (3-14) in the right hand side of (3-12), the equations become

$$I_T \omega_p \cos\theta = I_S \omega_{ST} \tag{3-15}$$

or

$$\frac{\omega_{ST}}{\omega_p} = \frac{I_T}{I_S} \cos\theta \tag{3-16}$$

One can see from (3-15) that, for smaller θ angles, the ratio of total spin rate to precession rate will tend to be high if the moment of inertia about the tumble axis is much greater than that about the spin axis, as might be expected for an elongated object. For objects with squatter shapes, the spin rate may approach the precession rate. If $I_T/I_S = 1$, ω_S is zero from (3-13) or $\omega_{ST} = \omega_p \cos\theta$ from (3-16), which means that the body is simply rotating with a total rotation rate ω_p, as would be the case with a sphere.

If all three principal moments of inertia are unequal, then the possible modes of motion are considerably more complex, and parameters cannot be as simply related as in the symmetrical body case. Derivations of relationships may be found in various mechanics texts* and will not be attempted here. However, the Poinsot construction, described in these texts, may be very useful in envisioning this general complex motion and is briefly discussed here.

The Poinsot construction can be used to describe the relative positions of a body's principal axes by the use of an "inertia ellipsoid" that has its three semi-axes parallel to the principal moment of inertia axes of an actual body. The ellipsoid semi-axes are given lengths proportional inversely with the square root of the corresponding principal moments of inertia. For example, an elongated, symmetrical object would be represented by an elongated ellipsoid, or prolate spheroid, with the semi-major axis parallel to the body symmetry axis. As indicated in the sketch of Figure 3-6, the Poinsot construction consists

*Such as Goldstein, Classical Mechanics (Addison-Wesley, 1950) and Arnold and Maunder, Gyrodynamics and Its Engineering Applications (Academic Press, 1961).

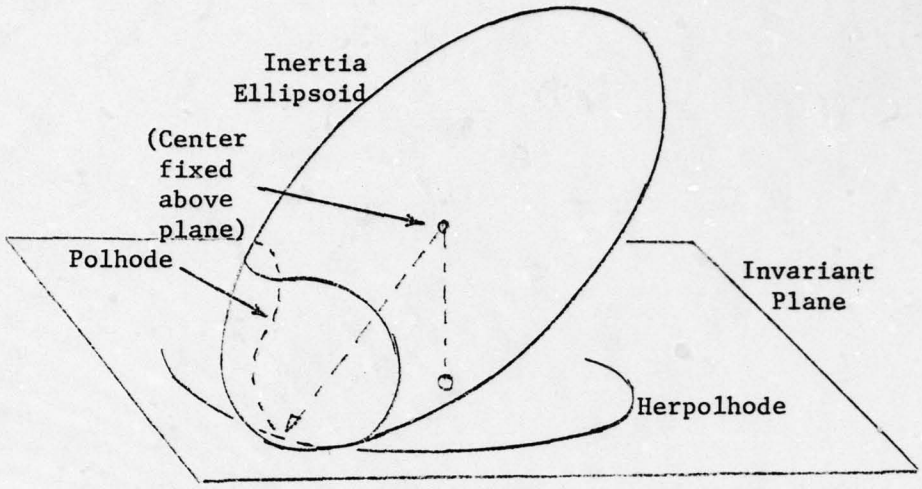

Figure 3-6

of positioning the center of the inertia elliposid at a fixed position above an "invariant plane" and allowing the inertia ellipsoid to roll on the invariant plane without slipping. The point of contact on the invariant plane traces out a path on the plane called the "herpolhode", and the trace of the contact point on the elliposid is the "polhode". In the general case, the polhode will close on itself, but the herpolhode does not necessarily close on itself. One should see from this construction that a symmetrical body with a large tumble axis moment of inertia will produce many revolutions of the body about the spin axis for one complete cycle of the spin axis attitude, or one precession cycle, in agreement with the previously-derived relationships. However, if this elongated body is made slightly unsymmetrical, so that the inertia ellipsoid does not have a circular cross section in cuts orthogonal to the original symmetry axis, then the rolling of the ellipsoid is "bumpy" and the spin axis will have a varying precession angle, θ, which may be termed a "nutation" of the spin axis. What has been called the precession angle, θ, in the previous discussion may more properly be called a "nutation angle", which is stated to be constant in the special case of bodies with two equal moments of inertia, but more generally would be time varying. As the inertia ellipsoid takes on various ratios of semi-axes and positions of its center relative to the invariant plane, one can see that the concept of a simple nutation effect of a spin axis can become

meaningless, since different spin, precesion, and nutation rates may couple to form complex rotational motion patterns. However, the possible modes of motion are constrained by the ratios of moments of inertia, and the Poinsot construction describes exactly the relative positions of body axes once initial conditions are established.

3.2 RANGE AND RANGE RATE OF SIMPLE ROTATING POINTS

If it is assumed that reflections from a target tend to arise in localized regions, a radar target might be represented by a first-order model which is a collection of rigidly connected points, each point centered on a scattering region. The reflected pulses from a wideband radar transmission may be displayed in some form of an intensity modulated raster or Range-Time-Intensity (RTI) plot, and the relative slant range positions of various points relative to each other may be traced as they vary with time. If narrowband data are coherently processed long enough to produce resolution of points in the Doppler dimension, then a similar display of Doppler response functions for different integration intervals may be obtained. Such a Doppler-Time-Intensity (DTI) display may allow the reflection center paths in the Doppler dimension to be traced, and these paths would be related to, but differ from, slant range traces. (DTI and RTI plots are illustrated and discussed in Section 1.)

An understanding of the forms these range and Doppler traces should take for various point locations and motion conditions may be obtained by examining the theoretical range and Doppler functions for ideal points, which will be derived in the following analysis. The range rate function will generally be used to represent the Doppler function to simplify notations, Doppler frequency then being obtainable from range rate by a simple conversion constant (as discussed in Section 1).

The analysis will proceed with the derivation of the relative range, ΔR, and range rate, $\Delta \dot{R}$, between a pair of idealized points on a target. The same results could be used to represent the function of a single point scatterer relative to the center of mass if one of the two points is placed at the mass

center. In the single-point case, the assumption is made that all translational motion effects of the center-of-mass have been removed by some form of compensation. The resulting signals are equivalent to those from a rotating target with a stationary center. Tracking one of two points and aligning the returns on the tracked point would have a similar effect.

Far-field approximations will be used in which the lines-of-sight from the radar to different points on the target are assumed parallel. The radar incidence direction, therefore, will be defined by a single unit vector, $\vec{R}$. For such far-field conditions, the relative range and range rate between a pair of points will not depend on the location of the points relative to the center of mass, but will depend only on the vector distance, $\vec{D}$, between the points as defined in a body-fixed coordinate system. The range and range rate functions for a multiplicity of scattering points may be obtained simply by adding new single-pair functions of the same form as that for the first pair but with new values of $\vec{D}$ for each new point relative to the reference point of the first pair.

The simplest form of free body rotation will be considered first. This is a simple rotation about one of the principal axes, as discussed in Section 3.1. Let two points on the body be located within a body-fixed coordinate system with axes X_b, Y_b, Z_b as sketched in Figure 3-7. Then the components of $\vec{D}$ may be designated by D_{Xb}, D_{Yb}, and D_{Zb}. If $\vec{D}$ is specified by angles α and β and length D, then

$$\begin{aligned} D_{Zb} &= D \sin\beta \\ D_{Xb} &= D \cos\beta \cos\alpha \\ D_{Yb} &= D \cos\beta \sin\alpha \end{aligned} \qquad (3\text{-}17)$$

Let the body rotate about the Z_b axis relative to an inertially fixed coordinate system having axes X, Y, Z, and let the rotation rate be Ω, giving a rotation

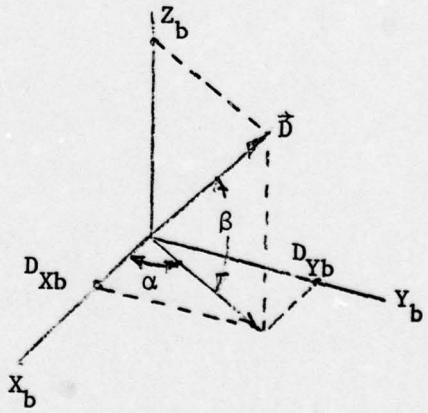

Figure 3-7

angle $\gamma = \Omega t$, as sketched in Figure 3-8. The coordinates of $\vec{D}$ in the X-Y-Z systems, D_X, D_Y, D_Z, are given by

$$\begin{aligned} D_X &= D_{Xb}\cos\gamma - D_{Yb}\sin\gamma \\ D_Y &= D_{Xb}\sin\gamma + D_{Yb}\cos\gamma \\ D_Z &= D_{Zb} \end{aligned} \qquad (3\text{-}18)$$

Now let the radar incidence direction vector, $\vec{R}$, be parallel to the X-Z plane and make an angle κ with respect to the z axis, as sketched in Figure 3-8 and redrawn in Figure 3-9.

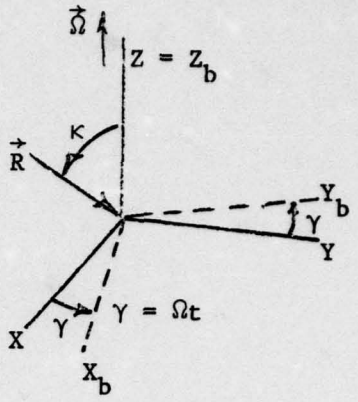

Figure 3-8

Then the components of $\vec{R}$ are

$$\begin{aligned} R_x &= -\sin\kappa \\ R_y &= 0 \\ R_z &= -\cos\kappa \end{aligned} \qquad (3\text{-}19)$$

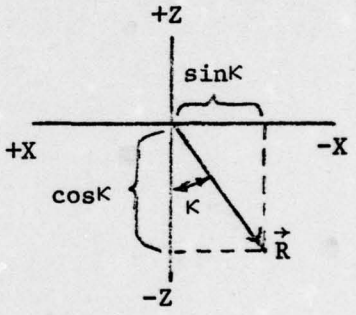

Figure 3-9

The projection of vector $\vec{D}$ onto $\vec{R}$, as sketched in Figure 3-10, can represent the slant range difference between the two points and may be obtained from the dot product of two vectors as

$$\Delta R = \vec{D} \cdot \vec{R}$$

$$\Delta R = -\sin\kappa\,(D_{Xb}\cos\gamma - D_{Yb}\sin\gamma) - \cos\kappa\, D_{Zb} \qquad (3\text{-}20)$$

Substituting (3-17) into (3-20) gives

$$\Delta R = -\sin\kappa(D\cos\beta\cos\alpha\cos\gamma - D\cos\beta\sin\alpha\sin\gamma) - D\cos\kappa\sin\beta$$

or

$$\Delta R = -D\sin\kappa\cos\beta(\cos\alpha\cos\gamma - \sin\alpha\sin\gamma) - D\cos\kappa\sin\beta \qquad (3\text{-}21)$$

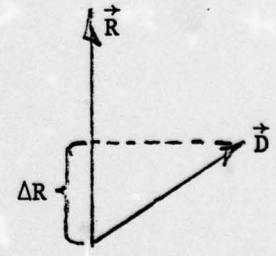

Figure 3-10

and since $\cos(\alpha + \gamma) = \cos\alpha\cos\gamma - \sin\alpha\sin\gamma$, and $\gamma = \Omega t$,

$$\Delta R = -(D \sin\kappa \cos\beta\cos(\Omega t + \alpha) + D \cos\kappa\sin\beta) \tag{3-22}$$

If $\kappa = 90°$, then (3-22) becomes

$$\Delta R = -D \cos\beta\cos(\Omega t + \alpha) \tag{3-23}$$

which is a simple cosinusoidal function. This might be expected for a rotation axis orthogonal to the incidence direction and a point extended orthogonally a distance $D\cos\beta$ from the rotation axis. For the more general case represented by (3-22), the mean of the cosine term is shifted by a constant, $D \cos\kappa\sin\beta$, if $|\kappa| \neq 90°$, and the magnitude of its variation is reduced in proportion to $\sin\kappa$. For $\kappa = 0°$ or $180°$, ΔR would be constant, as should also be obvious from a simple inspection of the geometry.

Relative Doppler frequency, then, is proportional to the time derivative of ΔR, $\Delta\dot{R}$, which is obtained from (3-22) as

$$\Delta\dot{R} = \Omega D\sin\kappa \cos\beta\sin(\Omega t + \alpha) \tag{3-24}$$

The sine variation of $\Delta\dot{R}$ in (3-24) may be seen as 90° out of phase with respect to the cosine variation in ΔR, and there is no constant bias value in $\Delta\dot{R}$. The effect of the change of angle κ is to reduce $\Delta\dot{R}$ to zero as $\vec{R}$ becomes parallel to the rotation axis.

The preceding formulation is not entirely general if the orientation of axes X, Y, Z, which may be considered inertially fixed, are to be specified with respect to a more universal system. Let X_I, Y_I, and Z_I be the celestial form of coordinates in which the common right ascension (RA) and declination (DEC) angles are used to define vector directions. Then, the X-Y-Z system of Figure 3-8 may be arbitrarily oriented with respect to the X_I-Y_I-Z_I system, and three angles would be required to specify this orientation, as discussed in Section 2.2 for a general coordinate rotation. Also in the more general case, $\vec{R}$ would not be constrained to the X-Z plane, but would be located within the X_I-Y_I-Z_I system according to various tracking conditions. If the rotations leading to the transformation matrix [A] of (2-9b) and (2-10) are also used

to locate the X-Y-Z system through the angles ϕ, θ, and ψ, substituting the X_I, Y_I, Z_I components in the left hand column matrix of (2-9b) and the X, Y, Z components in the right hand column matrix gives

$$\begin{bmatrix} D_{XI} \\ D_{YI} \\ D_{ZI} \end{bmatrix} = [A] \begin{bmatrix} D_X \\ D_Y \\ D_Z \end{bmatrix} \tag{3-25}$$

If the components of $\vec{R}$ in the celestial system are given by R_{XI}, R_{YI}, R_{ZI}, then

$$\Delta R = \vec{R} \cdot \vec{D} = R_{XI}\, D_{XI} + R_{YI}\, D_{YI} + R_{ZI}\, D_{ZI} \tag{3-26}$$

and

$$\Delta \dot{R} = \vec{R} \cdot \frac{\partial \vec{D}}{\partial t} + \vec{D} \cdot \frac{\partial \vec{R}}{\partial t} \tag{3-27}$$

where $\vec{D}$ is specified by (3-25) and a time-varying line-of-sight direction has been introduced, which must be calculated from the tracking data. Since transformation matrix [A] relates one inertially-fixed system relative to another inertially-fixed system, [A] is time invariant. Therefore,

$$\frac{\partial \vec{D}}{\partial t} = \begin{bmatrix} \dot{D}_{XI} \\ \dot{D}_{YI} \\ \dot{D}_{ZI} \end{bmatrix} = [A] \begin{bmatrix} \dot{D}_X \\ \dot{D}_Y \\ \dot{D}_Z \end{bmatrix} \tag{3-28}$$

and the right hand derivatives may be obtained from (3-17) and (3-18) as

$$\begin{aligned} \dot{D}_X &= -\Omega\, D \cos\beta \sin(\alpha + \Omega t) \\ \dot{D}_Y &= \Omega\, D \cos\beta \cos(\alpha + \Omega t) \\ \dot{D}_Z &= 0 \end{aligned} \tag{3-29}$$

If the rotations in Section 2.2 are carefully followed, it may be seen that the angle ϕ in [A] will be equal to the RA of the rotation axis and θ will be the complement of the declination of that axis (DEC = 90° - θ).

Thus, if an arbitrarily located pair of point scatterers is tracked and relative ranges or range rates, or both, are estimated from radar measurements, it should be seen that there are seven parameters which will determine

the functions of ΔR and $\dot{\Delta R}$. Those parameters are θ, ϕ, ψ, α, β, D, and Ω. However, since the X-Y-Z axes were allowed to be arbitrarily oriented through the angles θ, ϕ, ψ, then the angle α may be set to zero and the generalization is not impaired, so that there are truly only six independent parameters which will determine ΔR and $\dot{\Delta R}$. Various combinations of other parameters, such as rectangular components or other combinations of angles may be used to form an independent set to specify ΔR and $\dot{\Delta R}$, but whatever the form, six parameters will still be required. Conversely, six independent parameters may potentially be determined from ΔR and $\dot{\Delta R}$ functions. Whether these parameters will be practically determinable will depend on the accuracy and the degree of independence in the ΔR or $\dot{\Delta R}$ measurement.

If the line-of-sight ($\vec{R}$) does not change, then the resulting $\dot{\Delta R}$ sine function as given by (3-24) will be obtained, from which the rate Ω should be estimable if approximately a cycle of rotation is observed. Also, the peak of the variation in the sine wave will give Ω $D\cos\beta\sin\kappa$, so $A_1 = D\cos\beta\sin\kappa$ may be obtained, but this only puts certain constraints on the $\vec{D}$ vector and does not allow a solution of the full set of six parameters, or even of the true distance, D, which may be of most interest. Similarly, from a ΔR function for a fixed $\vec{R}$ as given by (3-22) the rate may be determined. The peak-to-peak variation of the cosine function would give $A_2 = D\cos\beta\sin\kappa$, and the bias value would give $A_3 = D\sin\beta\cos\kappa$. However, the isolated parameters could not be estimated from ΔR alone without a priori information on some of the parameters. If the combination of ΔR and $\dot{\Delta R}$ measurements are available, there still would not be sufficient information in the A_1, A_2, and A_3 quantities to solve for D, β, and κ, since $A_1 = A_2$. This indicates that for a solution of the motion and true point distance parameters to be obtainable from ΔR and $\dot{\Delta R}$ measurements, there must be a significant change in the line-of-sight direction during the measurements.

3.3 RANGE AND RANGE RATE OF SPINNING AND PRECESSING POINTS

Allowing a target to both precess and spin introduces more harmonic variations in the ΔR and $\dot{\Delta R}$ functions than a simple rotation, as should be expected from the additional frequency of rotation discussed in Section 3.1 The

derivations in this case will begin with the $\vec{D}$ vector between points specified in the body coordinate system X_b, Y_b, Z_b sketched in Figure 3-7 and components of $\vec{D}$ as specified in (3-17). Then let this system rotate with a rate ω_S, about an axis parallel to the Z_b axis and make an angle $\omega_S t$ with respect to a second system labeled X_S-Y_S-Z_S as sketched in Figure 3-11. The components of $\vec{D}$ in the second system are similar in form to (3-18) and, after substitution of components in the form of (3-17) and combining terms, become

$$\begin{aligned} D_{XS} &= D\cos\beta\cos(\omega_S t + \alpha) \\ D_{YS} &= D\cos\beta\sin(\omega_S t + \alpha) \\ D_{ZS} &= D\sin\beta \end{aligned} \qquad (3\text{-}30)$$

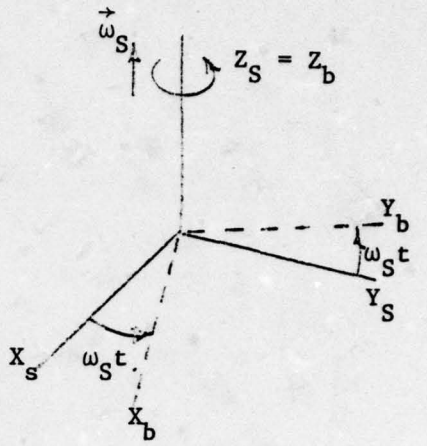

Figure 3-11

Let the spin axis be rotated about an axis parallel to Y_S, making an angle θ_P with respect to a third coordinate system labeled X_P-Y_P-Z_P as sketched in Figure 3-12. The components of $\vec{D}$ in the X_S-Y_S-Z_S system will have components in the Z_P-Y_P-Z_P system equal to the following in matrix form

$$\begin{bmatrix} D_{XP} \\ D_{YP} \\ D_{ZP} \end{bmatrix} = \begin{bmatrix} \cos\theta_P & 0 & \sin\theta_P \\ 0 & 1 & 0 \\ -\sin\theta_P & 0 & \cos\theta_P \end{bmatrix} \begin{bmatrix} D_{XS} \\ D_{YS} \\ D_{ZS} \end{bmatrix} \qquad (3\text{-}31)$$

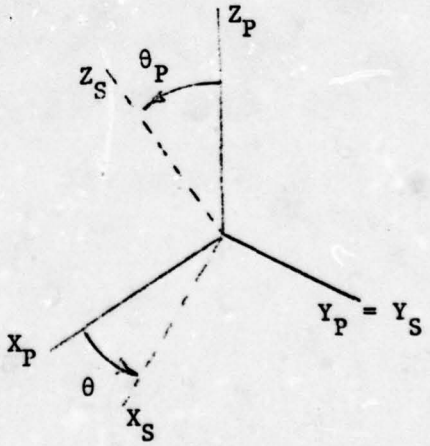

Figure 3-12

Let the X_P-Y_P-Z_P system rotate about an axis parallel to the Z_P axis at the precession rate ω_P, so that an angle $(\omega_P t + \phi_P)$

is made with respect to an inertially fixed X-Y-Z system as sketched in Figure 3-13. A bias angle, ϕ_P, has been added, which makes the starting angle arbitrary at t = 0. Components of $\vec{D}$ from X_P-Y_P-Z_P reflect into X-Y-Z as

$$\begin{bmatrix} D_X \\ D_Y \\ D_Z \end{bmatrix} = \begin{bmatrix} \cos(\omega_P t+\phi_P) & -\sin(\omega_P t+\phi_P) & 0 \\ \sin(\omega_P t+\phi_P) & \cos(\omega_P t+\phi_P) & 0 \\ 0 & 0 & 1 \end{bmatrix} \begin{bmatrix} D_{XP} \\ D_{YP} \\ D_{ZP} \end{bmatrix} \tag{3-32}$$

Substituting (3-30) into (3-31), (3-31) into (3-32), and performing the matrix multiplications gives the set

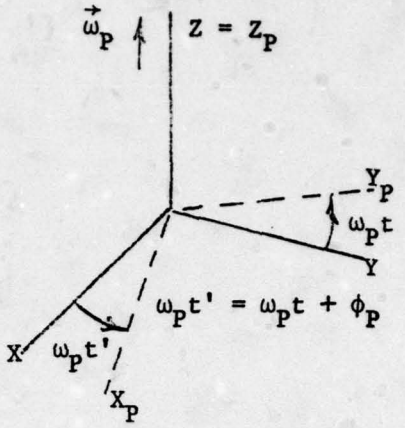

Figure 3-13

$$\begin{aligned} D_X &= [D\ \cos\beta\cos\theta_P\cos(\omega_P t + \phi_P)\ \cos(\omega_S t + \alpha) \\ &\quad - D\ \cos\beta\sin(\omega_P t + \phi_P)\ \sin(\omega_S t + \alpha) \\ &\quad + D\ \sin\beta\cos(\omega_P t + \phi_P)\ \sin\theta_P] \\ D_Y &= [D\ \cos\beta\cos\theta_P\sin(\omega_P t + \phi_P)\ \cos(\omega_S t + \alpha) \\ &\quad + D\ \cos\beta\cos(\omega_P t + \phi_P)\ \sin(\omega_S t + \alpha) \\ &\quad + D\ \sin\beta\sin\theta_P\ \sin(\omega_P t + \phi_P)] \\ D_Z &= -\ D\ \cos\beta\sin\theta_P\ \cos(\omega_S t + \alpha) + D\ \sin\beta\cos\theta_P \end{aligned} \tag{3-33}$$

If the radar line-of-sight is oriented parallel to the X-Z plane as shown previously in Figures 3-8 and 3-9, then $\vec{R}$ components given in (3-19) apply here, and the range difference function for the new case is obtained as

$$\Delta R = \vec{R} \cdot \vec{D} = -(\sin\kappa\ D_X + \cos\kappa\ D_Z) \tag{3-34}$$

where D_X and D_Z have been stated in (3-33). On making the substitution

$$\Delta R = -\Big\{ D\cos\beta\sin\kappa[\cos\theta_P\cos(\omega_P t + \phi_P)\cos(\omega_S t + \alpha) - \sin(\omega_P t + \phi_P)\sin(\omega_S t + \alpha)]$$
$$+ D\sin\beta\sin\kappa\sin\theta_P\cos(\omega_P t + \phi_P)$$
$$- D\cos\beta\cos\kappa\sin\theta_P\cos(\omega_S t + \alpha)$$
$$+ D\cos\kappa\sin\beta\cos\theta_P\Big\} \qquad (3\text{-}35)$$

The terms containing products of ω_P and ω_S functions have been combined in the brackets of the first term of (3-35). The other three terms are a constant plus two simple cosine functions of the two frequencies. The product functions can be transformed through the identity

$$\cos A\cos B\cos C - \sin B\sin C =$$
$$\frac{1}{2}[\cos(B + C)(\cos A + 1) + \cos(B - C)(\cos A - 1)] \qquad (3\text{-}36)$$

such that the product frequency factor in (3-35) can be expressed as

$$[\cos\theta_P\cos(\omega_P t + \phi_P)\cos(\omega_S t + \alpha) - \sin(\omega_P t + \phi_P)\sin(\omega_S t + \alpha)] =$$
$$\frac{1}{2}[\cos(\omega_P t + \phi_P + \omega_S t + \alpha)(\cos\theta_P + 1) + \cos(\omega_P t + \phi_P - \omega_S t - \alpha)(\cos\theta_P - 1)] \qquad (3\text{-}37)$$

Thus, it may be seen that if the line-of-sight vector ($\vec{R}$) does not vary in time, the ΔR function is the sum of a constant plus four simple cosine waves with frequencies ω_S, ω_P, $(\omega_P + \omega_S)$, and $(\omega_P - \omega_S)$.

The range rate function from the derivative of (3-35) becomes

$$\dot{\Delta R} = D\frac{\cos\beta}{2}\sin\kappa(\omega_P + \omega_S)(1 + \cos\theta_P)\sin[(\omega_P + \omega_S)t + \alpha + \phi_P]$$
$$- D\frac{\cos\beta}{2}\sin\kappa(\omega_P - \omega_S)(1 - \cos\theta_P)\sin[(\omega_P - \omega_S)t - \alpha + \phi_P]$$
$$+ \omega_P D\sin\beta\sin\kappa\sin\theta_P\sin(\omega_P t + \phi_P)$$
$$- \omega_S D\cos\beta\cos\kappa\sin\theta_P\sin(\omega_S t + \alpha) \qquad (3\text{-}38)$$

The ΔR and $\dot{\Delta R}$ functions for a fixed line-of-sight position can then be seen as dependent on eight variables: D, β, κ, θ_P, ω_S, ω_P, α, and ϕ_P. Unlike the case for simple rotation, the ΔR and $\dot{\Delta R}$ functions for the spinning and

precessing case do have the potential of allowing a solution for $\vec{D}$ for a fixed $\vec{R}$. However, simple rotation is a special case of the more complex motion, so as a simple rotation mode is approached, solutions for $\vec{D}$ and the other parameters of the complex motion formulation must also approach instability (where instability implies that small errors in measurements can cause large errors in parameter estimates).

One general method for solving for the parameters for the steady $\vec{R}$ case, if a complete measurement function could be specified, would be to take a Fourier transform of the function. For example, the $\Delta\dot{R}$ function of (3-38) can be summarized as

$$\Delta\dot{R} = \sum_{i=1}^{4} A_i \omega_i \sin(\omega_i t + \psi_i) \qquad (3\text{-}39)$$

A Fourier transform could be used to locate the ω_i from the resulting four peak responses in frequency. The complex functions at the times of the peaks should give the A_i and ψ_i values. Since the amplitude terms of the four frequencies contain the four unknown variables D, β, κ, θ_p (if ω_s and ω_p are determined), then estimates of the four amplitudes may be used to obtain estimates of those four parameters. However, care must be taken in considering possible ambiguities in these solutions.

The constant $\vec{R}$ case, even when it does give solutions for some of the parameters, cannot unambiguously provide an estimate of the precession vector direction, $\vec{\omega}_p$, which is also the total angular momentum vector direction. The angle κ locates $\vec{R}$ relative to $\vec{\omega}_p$ within a conical constraint. If the ω_s, ω_p rates are fast enough relative to the $\vec{R}$ rates, then different values of $\vec{R}$, denoted by $\vec{R}_i$, will give different κ values, κ_i. If $\vec{\omega}_{UP}$ is the unit vector direction of ω_p, then

$$\cos\kappa_i = \vec{R}_i \cdot \vec{\omega}_{UP} \qquad (3\text{-}40)$$

The direction $\vec{\omega}_{UP}$ can be considered to have three unknown components in rectangular coordinates, but these are combinable since the sum of their squares must be unity. Consequently, there are two completely unknown components in $\vec{\omega}_{UP}$ (which may be stated in RA and DEC angles), and two different $\vec{R}_i$ and κ_i sets are needed

to solve for these components, with a double ambiguity. A third set will resolve the ambiguity.

In the more general case, approximation of $\vec{R}_i$ as a constant as used in the preceding derivations will not hold and more general forms of solutions would be required. The formulations for ΔR and $\Delta\dot{R}$ should then follow the forms of (3-26) and (3-27), which are repeated here as

$$\Delta R = \vec{R} \cdot \vec{D} \tag{3-41}$$

and

$$\Delta\dot{R} = \vec{R} \cdot \frac{\partial\vec{D}}{\partial t} + \frac{\partial\vec{R}}{\partial t} \cdot \vec{D} \tag{3-42}$$

but with $\vec{D}$ components now given by (3-33) and $\frac{\partial\vec{D}}{\partial t}$ given by the derivatives of (3-33). The Euler transformation matrix [A] may be used to locate the X-Y-Z system relative to the inertial X_I-Y_I-Z_I system, in which case ϕ_P should be set to zero since the equivalent angle is absorbed in the Euler rotation angles. There then would be six variables (ω_S, ω_P, α, θ_P, D, and β) plus the three Euler angles (θ, ϕ, and ψ) for a total of nine independent parameters needed to specify ΔR and $\Delta\dot{R}$, assuming $\vec{R}$ and $\frac{d\vec{R}}{dt}$ have been estimated in the known X_I-Y_I-Z_I framework.

3.4 SLIPPING POINTS

The analysis in Sections 3.2 and 3.3 assumed that localized radar scattering persisted as if the centers of reflection were rigidly fixed to the target. Scattering related to smooth rings and curved surfaces may be treated as if localized to a particular specular point over small variations in aspect angles, but over larger angles this point location may appear to move in a slipping sense to different positions depending on the incidence direction. Consider a simple ring as sketched in Figure 3-14. Let $\vec{S}$ be the unit direction vector of the symmetry axis of the ring, which is normal to the plane of the ring. The main reflections from this ring will occur at the points where the incidence direction $\vec{R}$ is perpendicular to the tangent to the ring. Only one of these points will be treated here, as designated in Figure 3-14. In the edge-on view, $\vec{S}$ and $\vec{R}$ are in the projection plane, and the angle between the two vectors is ϕ_r. The vector distance from the ring center to the reflection point

is $\vec{P}$, which is given components $\vec{P}_A$ parallel to $\vec{R}$ and $\vec{P}_B$ orthogonal to $\vec{P}$. In the continuation of this analysis, the component $\vec{P}_A$ will be the more important. This component can be stated in terms of $\vec{R}$ as

$$\vec{P}_A = -\vec{R}a \sin \phi_r = -\vec{R}\, a \sqrt{1 - (\vec{R} \cdot \vec{S})^2} \qquad (3\text{-}43)$$

where a is the radius and $\sin^2 \phi_r = 1 - \cos^2 \phi_r$. The positive sign is taken for the radical after defining ϕ_r between 0° and 180°. The total vector $\vec{P}$ is

$$\vec{P} = \vec{P}_A + \vec{P}_B \qquad (3\text{-}44)$$

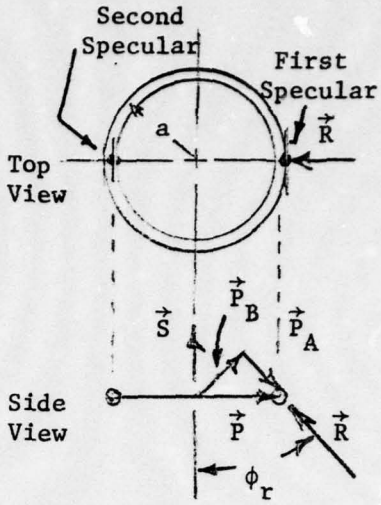

Figure 3-14

One should see that if $\vec{R}$ maintained a constant angle ϕ_r with respect to $\vec{S}$, but was otherwise allowed to move (i.e., roll about $\vec{S}$), the reflection point where $\vec{R}$ is perpendicular to the tangent to the ring will slip about the ring and appear at different ring positions. The reflection point locations given by $\vec{P}$ as stated in (3-43) and (3-44) include the slipping effect.

Now consider the case of a doubly trunacted cone with radii a_1 and a_2 at the truncations and vector positions of slipping reflection points given by $\vec{P}_1$ and $\vec{P}_2$, as sketched in Figure 3-15. Major reflections are expected to occur from the ring edges in the sense of Figure 3-14 at nonspecular aspects to the body surfaces. The scattering amplitudes may vary with aspect angle, but the specular point reflections from the edges are expected to occur in the ring sense. Then let a vector distance $\vec{H}$ define the length of the body along the symmetry axis. Two reflection points can be expected to occur at the ends of $\vec{P}_1$ and $\vec{P}_2$, and the distance, $\vec{D}$, between these points may be summed as

$$\vec{D} = -\vec{P}_2 + \vec{H} + \vec{P}_1 \qquad (3\text{-}45)$$

Using (3-43) and (3-44),

$$\vec{D} = -(-\vec{R}\, a_2 \sin\phi_r + \vec{P}_{B2}) + \vec{H} + (-\vec{R}\, a_1 \sin\phi_r + \vec{P}_{B1}) \qquad (3\text{-}46)$$

where

$$\sin\phi_r = \sqrt{1 - (\vec{R} \cdot \vec{S})^2}$$

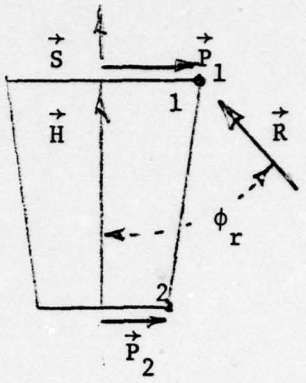

Figure 3-15

The slant range difference between points 1 and 2 is then given by $\Delta R = \vec{R} \cdot \vec{D}$, and since $\vec{P}_{B1}$ and $\vec{P}_{B2}$ are by definition orthogonal to $\vec{R}$, the result is

$$\Delta R = \vec{D} \cdot \vec{R} = (a_2 - a_1)\sqrt{1 - (\vec{R} \cdot \vec{S})^2} + \vec{H} \cdot \vec{R} \qquad (3\text{-}47)$$

Relationships for $\vec{H}$ can be derived from previous fixed-point analyses. Following the sketch in Figure 3-7, $\vec{H}$ may be derived from the $\vec{D}$ relationships by making $\beta = 90°$, which would be equivalent to placing two fixed points along the symmetry axis. The substitution of $\beta = 90°$ in (3-33) for the spinning and precessing points allows components for $\vec{H}$ to be derived as

$$\begin{aligned} H_X &= H \cos(\omega_p t + \phi_p) \sin\theta_p \\ H_Y &= H \sin\theta_p \sin(\omega_p t + \phi_p) \\ H_Z &= H \cos\theta_p \end{aligned} \qquad (3\text{-}48)$$

then $\vec{S} = \vec{H}/H$.

If a fixed line-of-sight $\vec{R}$ is specified according to (3-19) from Figures 3-8 and 3-9, as before, then

$$\vec{R} \cdot \vec{H} = -H[\sin\kappa \cos(\omega_p t + \phi_p) \sin\theta_p + \cos\kappa\cos\theta_p] \qquad (3\text{-}49)$$

and

$$\vec{R} \cdot \vec{S} = \vec{R} \cdot \vec{H}/H \qquad (3\text{-}50)$$

For a simple right circular cylinder $a_1 = a_2$, and ΔR reduces to

$$\Delta R = -H(\sin\kappa \cos(\omega_p t + \phi_p) \sin\theta_p + \cos\kappa\cos\theta_p) \tag{3-51}$$

and the range rate is

$$\dot{\Delta R} = H\, \omega_p \sin\kappa\sin(\omega_p t + \phi_p) \sin\theta_p \tag{3-52}$$

For simple cylinder edges, the variations in ΔR and $\dot{\Delta R}$ are then simple sine or cosine functions with frequency, ω_p. For $a_1 \neq a_2$, the added term $(a_1 - a_2)\sqrt{1 - (\vec{R} \cdot \vec{S})^2}$ complicates the patterns, so that a more complex variation must occur.

A doubly curved reflecting element could represent a slipping point which can move with two degrees of freedom to any point on that element instead of just being constrained to a ring. A sphere would be the simplest form of such a surface. The specular reflection point for any orientation of $\vec{R}$ can be specified by the vector distance $\vec{P}_S$ from the center of curvature to the specular point sketched in Figure 3-16. Since this specular reflection is centered on the point where $\vec{R}$ is perpendicular to the plane tangent to the surface, it occurs at the point of intersection of a line parallel to $\vec{R}$ passing through the center of curvature. Therefore,

$$\vec{P}_S = -a_s \vec{R} \tag{3-53}$$

where a_s is the radius of curvature. Next, consider a body formed from a cone with a truncation forming a ring edge of radius a_1, and having a spherical shape on the other end, instead of another sharp truncation. Let the vector distance between the sphere center of curvature and the back plane of the ring, parallel to the symmetry axis, be specified by $\vec{H}$, as sketched in Figure 3-17. Then the distance $\vec{D}_{S1}$ between the ring edge at point 1, and the specular point at point s may be given by

$$\vec{D}_{S1} = -\vec{P}_S + \vec{H} + \vec{P}_1 \tag{3-54}$$

or from (3-44) and (3-53),

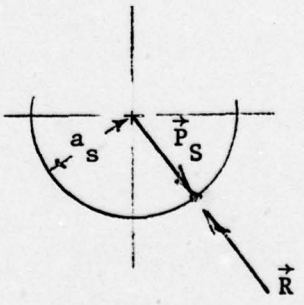

Figure 3-16

$$\vec{D}_{S1} = -a_s\vec{R} + \vec{H} - a_1\vec{R}\sqrt{1 - (\vec{R} \cdot \vec{S})^2} + \vec{P}_{B1} \qquad (3\text{-}55)$$

where $\vec{S}$ and $\vec{H}$ are defined as before. Then $\Delta R = \vec{R} \cdot \vec{D}$ gives

$$\Delta R = -a_s + \vec{R} \cdot \vec{H} - a_1\sqrt{1 - \frac{(\vec{R} \cdot \vec{H})^2}{H^2}} \qquad (3\text{-}56)$$

For a fixed $\vec{R}$, the variation in ΔR will then have a simple variation according to $\cos\omega_p t$ from the $\vec{R} \cdot \vec{H}$ term, but the term under the radical in (3-56) will make the variation more complex, with similar effects in $\dot{\Delta R}$.

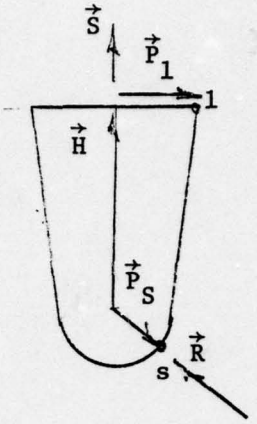

Figure 3-17

As a third case, consider the geometry of Figure 3-17, but with a truly fixed point on the edge of the ring where the reflection from this point does not slip but occurs at the same point on the ring as in the analysis of points in Sections 3.2 and 3.4. Figure 3-18 illustrates this new case. Then let the vector distance from the center of the spherical section to the fixed point be given by the vector $\vec{D}_f$. In this case, the full set of terms used in (3-33) may be applied, with definitions of $\vec{D}_f$ according to the original $\vec{D}$ specification in Figure 3-7. The total distance, $\vec{D}_T$, between the sphere specular point at s and the fixed point at 1 could be given by

Fixed point at 1

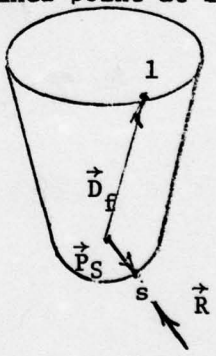

Figure 3-18

$$\vec{D}_T = -\vec{P}_S + \vec{D}_f = a_s\vec{R} + \vec{D}_f \qquad (3\text{-}57)$$

such that the relative range can be given by

$$\Delta R = \vec{R} \cdot \vec{D}_T = a_s + \vec{D}_f \cdot \vec{R} \qquad (3\text{-}58)$$

Now all of the analysis used in Section 3.3 for the spinning and precessing cases applies if the constant term a_s is simply added to the ΔR term in (3-35). The $\Delta\dot{R}$ term in (3-38) would not be affected by this addition since a_s is a constant. The difference is that the variations in the functions will not depend on the total distance vector between reflection points, but will depend on the distance of the fixed point on the flat surface edge and the center of curvature at the opposite end. For small radii of curvature, a_s, it may be seen that the approximation can be made that the spherical specular is equivalent to a fixed point near the center and an analysis may proceed as if from a pair of fixed points.

3.5 RELATING RANGE AND RANGE RATE FUNCTIONS TO TARGET PARAMETERS

3.5a Noniteractive Methods

Since the ΔR or $\Delta\dot{R}$ functions derived in Sections 3.2, 3.3, and 3.4 are dependent on certain target parameters, measurements of ΔR and $\Delta\dot{R}$ are potentially usable in estimating those parameters, as has been discussed to some extent. Determination of periodicities from inspection of ΔR and $\Delta\dot{R}$ functions may obviously be used to determine certain rotation rates. This would be easiest in the case of a target simply rotating at a high rate relative to the $\vec{R}$ rate. In the case of spinning and precessing bodies, the mixture of periodicities may be more difficult to determine unless the spin rate is much higher than the precession rate (or vice versa). However, Fourier analysis of the ΔR or $\Delta\dot{R}$ function may give the periodicities when $\vec{R}$ rates are slow, as was discussed in Section 3.3.

Overall target dimensions may be inferred from the maximum excursions in ΔR or $\Delta\dot{R}$ if estimates of rotation periods are apparent. A maximum excursion in ΔR can give a length measurement directly. For simple rotation, particularly if there are a number of reflection points at different extremes of the target, an estimate of target extent, L_e, may be obtained from a maximum range rate difference, ΔR_{max}, according to

$$L_e = \frac{\Delta\dot{R}_{max}}{\omega} \tag{3-59}$$

where ω is an estimated rotation rate from pattern periodicity. Unless a priori information about the rotation axis can be established, these estimates from ΔR and $\Delta\dot{R}$ must be considered as lower limits of true overall dimensions. For example, the maximum amplitude for $\Delta\dot{R}$ in (3-24) is

$$\Delta\dot{R}_{max} = \Omega D \sin\kappa \cos\beta$$

so

$$L_e = \frac{\Delta\dot{R}_{max}}{\Omega} = D \sin\kappa \cos\beta \tag{3-60}$$

Thus, the true length, D, cannot be estimated except within the factor $\sin\kappa \cos\beta$.

A special case of interest might be a cone-sphere, rapidly spinning and slowly precessing, with a number of discontinuities on the back edge, as sketched in Figure 3-19. The maximum range rate between extreme scattering points on the edge might approximately give an apparent diameter

$$D_e' = D \sin\kappa \tag{3-61}$$

based on the Section 3.2 results, letting $\beta = 0$. Slow precession may then have the effect of a varying κ. If the translational velocity direction might approximately represent the direction of the precession axis at some time during a flight, to allow a mean value of κ, κ_m, then an estimate might be made according to

$$D_e' = \frac{\Delta\dot{R}_{max}}{\Omega \sin\kappa_m} \tag{3-62}$$

and the average value of D_e', if observed over a precession cycle, might give an acceptably accurate base diameter.

3.5b Nonlinear Least Squares

The general anticipation in analysis of measurements of quantities like ΔR and $\Delta\dot{R}$ is that the data will allow a unique determination of the target

parameters governing the functions. Even if unique solutions are not possible, the ambiguous solutions may be limited to a small number. Since practical data measurements may be generally considered errored, more independent data sets than required for the number of parameters to be estimated are desirable so that there may be some smoothing of the errors. A common data smoothing technique with redundant data is the method of least squares, which will be described in a general form in the following discussion.

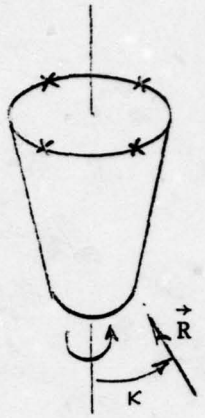

Figure 3-19

Quantities like ΔR and $\Delta \dot{R}$ are functions of a number of variables that are independent of time. For example, $\Delta R_i = f_i(X_k)$ could be used to describe the ΔR function at some instant in time designated by the index i, and $f_i(X_k)$ indicates that f_i is a function of a number of parameters X_k, with an identifying index k, varying from 1 to K_{max}. Variables X_k might represent $X_1 = \omega_S$, $X_2 = \omega_P$, etc., from the equations of Sections 3.3 and 3.4. The number of time samples in a measurement set could be IMAX so the index i would run from 1 to IMAX in the data measurements series.

Let a measurement of f_i be represented by f_{mi}. This measurement may be in error relative to the true value, f_i. The residual error may then be designated, E_i, and given by

$$E_i = (f_{mi} - f_i) \tag{3-63}$$

In the least squares data fitting method, a sum of square errors is formed according to

$$Q = \sum_{i=1}^{IMAX} (E_i)^2 = \sum_{i=1}^{IMAX} (f_{mi} - f_i)^2 \tag{3-64}$$

The objective, then, is to find those sets of X_k values which make Q a minimum. The minimization conditions will be governed by the set of equations represented by

$$\frac{\partial Q}{\partial X_n} = -2 \sum_i (f_{mi} - f_i) \frac{\partial f_i}{\partial X_n} = 0 \qquad (3\text{-}65)$$

in which the index n varies from n = 1 to KMAX to give KMAX equations from which the X_k parameters may be solved. If f_i were a linear function of X_k, the problem would be a simple linear least squares problem. Then the KMAX equations represented by (3-65) would give the classical least squares normal equations, which are linear, and a unique set of X_k would be determined by one matrix inversion.

Unfortunately, the f_i, as representing functions like ΔR and $\Delta \dot{R}$ derived in the previous sections, are nonlinear and the resulting normal equations from (3-65) are nonlinear. Excepting very special cases, solutions for X_k require iterative techniques. Further complications are that with nonlinear functions, f_i, the square error function (3-64), itself, may have more than one stationary point, i.e., there may be a number of sets of X_k for which (3-65) is satisfied.

A very simple approach to solving for X_k would be to calculate Q for all values of X_k that could be expected and pick the set that gives the overall minimum in Q. For one or two unknown parameters, this approach may be reasonable, but as the number of unknowns becomes greater, the search matrix of values becomes too large for practical computer calculations to be accomplished in reasonable times.

A very common approach in iterative schemes is to use a Taylor series expansion of the f_i function about some initial estimate of the X_k parameters and truncate the Taylor series at the linear terms. Thus, (3-64) and (3-65) can be treated as steps in which a set of ΔX_k is estimated, added to the initial guess values, and these new values are used as starting values for a new Taylor expansion to calculate the next ΔX_k set. The value of Q will tend to be reduced with each new X_k set, and the iterations may be stopped on the basis of a number

of criteria, such as ΔX_k values reaching certain minima or the Q value, itself, not changing significantly with new steps.

The first-order Taylor series expansion of f_i may be stated as

$$f_i \approx f_{io} + \left.\frac{\partial f_i}{\partial X_1}\right|_o \Delta X_1 + \left.\frac{\partial f_i}{\partial X_2}\right|_o \Delta X_2 \ldots + \left.\frac{\partial f_i}{\partial X_k}\right|_o \ldots + \left.\frac{\partial f_i}{\partial f_{X_{KMAX}}}\right|_o \tag{3-66}$$

in which f_{io} and $\left.\frac{\partial f_i}{\partial X_k}\right|_o$ imply an evaluation of the corresponding functions with initial values of X_k or X_{ko}, such that new values of X_k will be given by

$$X_k = X_{ko} + \Delta X_k \tag{3-67}$$

In the following discussions, the subscript will be dropped from the partial derivatives to simplify the notation, i.e., $\frac{\partial f_i}{\partial X_k}$ will represent $\left.\frac{\partial f_i}{\partial X_k}\right|_o$.

Substituting (3-66) in (3-64) gives

$$Q \approx \sum_{i=1}^{IMAX} \left(f_{mi} - f_{io} - \sum_{k=1}^{KMAX} \frac{\partial f_i}{\partial X_k} \Delta X_k\right)^2 \tag{3-68}$$

The ΔX_k are the unknown set of parameters to be solved in any one step. From (3-66),

$$\frac{\partial f_i}{\partial \Delta X_n} = \frac{\partial f_i}{\partial X_n} \tag{3-69}$$

Substituting (3-69) in (3-65) gives

$$\frac{\partial Q}{\partial X_n} = -2\left\{\sum_i (f_{mi} - f_{io}) \frac{\partial f_i}{\partial X_n} - \sum_k \Delta X_k \sum_i \frac{\partial f_i}{\partial X_k} \frac{\partial f_i}{\partial X_n}\right\} = 0 \tag{3-70}$$

The linearized equations then are of the form

$$\Delta X_1 \sum \frac{\partial f_i}{\partial X_i} \frac{\partial f_i}{\partial X_n} + \Delta X_2 \sum \frac{\partial f_i}{\partial X_2} \frac{\partial f_i}{\partial X_n} + \ldots \Delta X_{KMAX} \sum \frac{\partial f_i}{\partial X_{KMAX}} \frac{\partial f_i}{\partial X_n} = -\sum (f_{io} - f_{mi}) \frac{\partial f_i}{\partial X_n} \tag{3-71}$$

where, again, the index on n runs from 1 to KMAX, to give KMAX equations.

A more compact formulation of the problem is obtained if a partial derivative matrix is defined as

$$D = \begin{bmatrix} \frac{\partial f_1}{\partial X_1} & \frac{\partial f_1}{\partial X_2} & \cdots & \frac{\partial f_1}{\partial X_{KMAX}} \\ \frac{\partial f_2}{\partial X_1} & \frac{\partial f_2}{\partial X_2} & \cdots & \\ \vdots & & & \\ \frac{\partial f_{IMAX}}{\partial X_1} & \frac{\partial f_{IMAX}}{\partial X_2} & \cdots & \frac{\partial f_{IMAX}}{\partial X_{KMAX}} \end{bmatrix} \tag{3-72}$$

where, as stated, the evaluations are at an initial set of X_k, X_{ko}. Then, it may be seen that, for all values of n in (3-71), the full set of equations may be stated as

$$D^T D\,[\Delta X_k] = D^T E_r \tag{3-73}$$

where $[\Delta X_k]$ is a column matrix of the unknown parameter steps and E_r is a column matrix defined by the terms $-(f_{io} - f_{mi}) = E_{ri}$

$$E_r = -\begin{bmatrix} (f_{10} - f_{m1}) \\ (f_{20} - f_{m2}) \\ \vdots \\ f_{IMAX0}\ f_{mIMAX} \end{bmatrix} \tag{3-74}$$

The solution for ΔX_k set is obtained from the inverse of the D^TD matrix as

$$[\Delta X_k] = [D^T D]^{-1} D^T E_r \tag{3-75}$$

Because of the nonlinearity of the model, function f_i may allow more than one minimum in the Q function. Whether that minimum will correspond to the correct X_k set arrived at after a number of iterations will depend on the location of the starting values. Furthermore, the nonlinearity conditions may be such that a step of ΔX_k may actually increase Q in some iteration steps, so that

tests must be made to ensure that Q is minimized. Various auxiliary techniques may be used to control the ΔX_k values in such a way to ensure minimization. Different starting values may be used in different sets of iterations so that more than one stationary point in Q may be found, with the hope that the one with the lowest Q value (i.e., the global minimum) will give the correct answer. However, there is no assurance in all types of problems that the global minimum will give the correct solution if all the parameters are allowed to take on any range of values. It may then be necessary to set a priori limits on what the practical range of parameters should be and restrict the iterations to a search within those limits.

3.5c Error Analysis

Once a solution of X_k values has been achieved through an iterative scheme as described in Section 3.4, there may be interest in obtaining error bounds on the parameter estimates. If the errors are small, statistical inferences may be made, based on the same Taylor expansion linearization expressed in (3-66). If the final X_k values are assumed satisfactorily close to the true values, they may be treated as true values for the following approximations. From (3-66), deviations of f_i from the true mean value, f_{io}, may be expressed as

$$E_{xi} = (f_i - f_{io}) = \sum_k \frac{\partial f_i}{\partial X_k} \Delta X_k \tag{3-76}$$

or for the full set of E_{xi} expressed as a column matrix, $[E_{xi}]$, with elements from i to IMAX, and column matrix $[\Delta X_k]$,

$$[E_{xi}] = D\,[\Delta X_k] \tag{3-77}$$

Let the errors in E_{xi} be represented by a Gaussian error moment matrix given by $[\sigma_{Em}\ \sigma_{En}]$. Then statistical theory shows that, if E_{xi} are random variables linearly related to random variables ΔX_k through the transformation matrix, D, as given in (3-77), the variance-covariance or error moment matrix of E_{xi}, $[\sigma_{Em}\ \sigma_{En}]$, is related to the error moment matrix of ΔX_k, $[\sigma_{Xm}\ \sigma_{Xn}]$, through

$$[\sigma_{Em}\ \sigma_{En}] = D[\sigma_{Xm}\ \sigma_{Xn}]D^T \tag{3-78}$$

The moment matrix of $[\Delta X_k]$ can then be obtained from (3-78) as

$$[\sigma_{Xm}\ \sigma_{Xn}] = [D^T D]^{-1}\ D^T\ [\sigma_{Em}\ \sigma_{En}]\ L\ [D^T D]^{-1} \tag{3-79}$$

In the special case where the errors in the measurements of a variable like $\Delta\dot{R}$ are assigned a common variance, $\sigma^2_{\Delta\dot{R}}$, and covariance terms are zero, then $[\sigma_{Em}\ \sigma_{En}] = \sigma^2_{\Delta\dot{R}}\ [I]$, where I is the identity matrix. Equation (3-79) becomes

$$[\sigma_{Xm}\ \sigma_{Xn}] = \sigma^2_{\Delta\dot{R}}\ [D^T D]^{-1} \tag{3-80}$$

Since calculating $[D^T D]^{-1}$ is part of the iteration process for parameter estimation, once a conversion point is reached, one more calculation of this matrix is readily accomplished to obtain an error estimate. The diagonal terms in $[\sigma_{Xm}\ \sigma_{Xn}]$ would then give estimates of variances of solved parameters such as $\sigma^2_{\omega_S}$, $\sigma^2_{\omega_P}$ for spin rate ω_S or precession rate ω_P, and then the standard deviations, σ_{ω_S}, σ_{ω_P}, the commonly used form of error specification, would be obtainable.

3.5d More General Forms of Least Squares

The error function Q in (3-64) was stated without weighting the error terms. A more general formulation would be a weighted least squares according to

$$Q = \sum_i W_i\ (E_i)^2 \tag{3-81}$$

where W_i would be determined by some measure of how much more accurate one measurement of E_i is relative to another. A common weighting scheme would be to make $W_i = \dfrac{1}{\sigma^2_{Ei}}$, where $\sigma_{Ei}{}^2$ is a variance value associated with E_i. Then a weighting function matrix, W, would be given by a diagonal form which is

$$W = [\sigma_{Em}\ \sigma_{En}]^{-1} = \begin{bmatrix} \dfrac{1}{\sigma^2_{Ei}} & 0 & \cdots \\ 0 & \dfrac{1}{\sigma^2_{Ei}} & \\ \vdots & & \ddots \end{bmatrix} \tag{3-82}$$

It can be shown that (3-73) becomes

$$D^T W D [\Delta X_k] = D^T W E_r \tag{3-83}$$

and (3-67) becomes

$$[\Delta X_k] = [D^T W D]^{-1} D^T W E_r \tag{3-84}$$

If all of the variances are equal, (3-84) can be reverted to the original form in (3-75).

The weighted form would be of less significance in practical problems if only one variable like ΔR or $\Delta \dot{R}$ represented the measurement set. However, if both types of data could be measured simultaneously, the least squares problem should simultaneously include both sets. For example, assume that two f_i functions, labeled f_{Ai} and f_{Bi}, represent two different types of data like ΔR and $\Delta \dot{R}$. Then, the square error functions should read

$$Q = \sum_{i=1}^{IMAX} W_{Ai} (f_{Ami} - f_{Ai})^2 + W_{Bi} (f_{Bmi} - f_{Bi})^2 \tag{3-85}$$

and the W_{Ai} relative to W_{Bi} would become important. Even more generally, the number of measurements of each variable may not be equal or simultaneous, so that the index could run differently on each variable, as in

$$Q = \sum_{i=1}^{IMAX} W_{Ai} (f_{Ami} - f_{ai})^2 + \sum_{n=1}^{NMAX} W_{Bn} (f_{Bmn} - f_{Bn})^2 \tag{3-86}$$

The fundamental form of solution suggested by (3-84) would not change, however, because the appropriate matrices would be constructed according to a sequential ordering of the data sets represented by the measurements, f_{Am} and f_{Bm}. For example, D would be represented as

$$D = \begin{bmatrix} \frac{\partial f_{A1}}{\partial X_1} & \frac{\partial f_{A1}}{\partial X_2} & \cdots & \frac{\partial f_{A1}}{\partial X_{KMAX}} \\ \frac{\partial f_{A2}}{\partial X_2} & & & \\ \vdots & & & \\ \frac{\partial f_{AIMAX}}{\partial X_1} & \cdots & & \frac{\partial f_{AIMAX}}{\partial X_{KMAX}} \\ \frac{\partial f_{B1}}{\partial X_1} & & & \\ \frac{\partial f_{B2}}{\partial X_1} & & & \\ \vdots & & & \\ \frac{\partial f_{BMAX}}{\partial X_1} & \cdots & & \frac{\partial f_{BNMAX}}{\partial X_{KMAX}} \end{bmatrix} \qquad (3\text{-}87)$$

The ordering of W would follow as

$$W = \begin{bmatrix} \frac{1}{\sigma_{Ei}^2} & 0 & \cdots & & & & \\ 0 & \frac{1}{\sigma_{Ei}^2} & & & & & \\ \vdots & & \ddots & & & & \\ & & & \frac{1}{\sigma_{AIMAX}^2} & & & \\ & & & & \frac{1}{\sigma_{B1}^2} & & \\ & & & & & \ddots & \\ & & & & & & \frac{1}{\sigma_{BNMAX}^2} \end{bmatrix} \qquad (3\text{-}88)$$

and E_r would follow in a similar fashion, with the $(f_{Aio} - f_{Am})$ terms of (3-74) followed by $(f_{Bno} - f_{Bmn})$ terms in a continuation of the column matrix.

3.5e Special Functionalizations

The input data to the parameter estimation may be the actual samples of ΔR and $\Delta\dot{R}$, with model functions of unknown parameters as suggested in Sections 3.2., 3.3, and 3.4. However, various derivative forms may be found which would not necessarily require solutions of all of the parameters. For example, in the case of a simply rotating point, or pair of points, if the rotation rate is very rapid, then a varying amplitude cosine wave would be seen, theoretically as was suggested by (3-22), which was of the form

$$\Delta R = -(\Delta R_A \cos(\Omega t + \alpha) + \Delta R_B) \tag{3-89}$$

where

$$\Delta R_A = D \cos\beta \sin\kappa$$
$$\Delta R_B = D \sin\beta \cos\kappa$$

If the line-of-sight, $\vec{R}$, is slowly changing it may be possible to estimate the peak-to-peak variation which would give ΔR_A as suggested in Figure 3-20. This type of measurement may be possible even if the ΔR function is fragmentary or otherwise not specifiable well enough to obtain a complete set of instantaneous point values. Then different ΔR_{Ai} would be estimated at different time points indexed by i, with variations in $\vec{R}$ appearing in different values of κ_i. If the rotation axis direction is unknown, there would be two unknown variables needed to specify that direction. The extent of the scatterer orthogonal to the rotation axis, $D\cos\beta$, could be treated as a single unknown variable, $D_A = D\cos\beta$. A least squares error function might be of the form

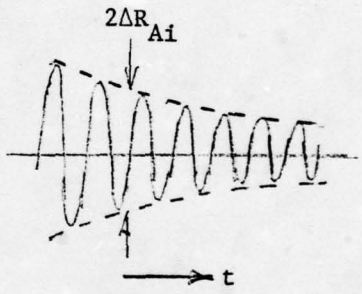

Figure 3-20

$$Q = \sum_i (\Delta R_{Ami} - \Delta R_{Ai})^2 \tag{3-90}$$

where

$$\Delta R_{Ai} = D_A \sin\kappa$$

and since

$$\vec{R}_i \cdot \vec{\Omega} = \cos\kappa_i \tag{3-91}$$

$$\Delta R_{Ai} = D_A \sqrt{1 - (\vec{R}_i \cdot \vec{\Omega})^2} \tag{3-92}$$

where $\vec{\Omega}$ is the rotation axis direction. The parameter estimation is reduced to three variables, but is still nonlinear and would generally require nonlinear iterative methods. A similar formulation could be made for the $\Delta\dot{R}$ function in (3-24), except that D_a might be modified to include the rotation rate in $D'_a = \Omega D\cos\beta$, and $D\cos\beta$ could be estimated if a rotation rate is estimated from the pattern periodicity.

In a similar fashion, advantage may be taken of other special conditions of target feature appearances which may be modeled in terms of at least partial parameters of the target motion or configuration. Data fitting may possibly be made with either linear or nonlinear functionalizations using the least squares methods.

3.5d Common Ambiguity In Single Tracks

In many cases of a track of an orbital or suborbital target, the line-of-sight vectors, $\vec{R}$, are nearly parallel to a common plane. This condition creates a pair of ambiguous solutions related to the plane geometry and the target rotational motion parameters. If the $\vec{R}$ vectors were coplanar, similar measurements would be obtainable if the free body rotation axis or momentum vector direction were placed at either of two symmetrical positions on opposite sides of the common $\vec{R}$ plane. Various of the parameters may have different values for the two ambiguous solutions, but the symmetrical positioning of axes relative to the $\vec{R}$ plane can be considered the primary condition. In the nonlinear iterative schemes for obtaining solutions, once the iterations have reached a minimization of the error function (Q) with one set of parameters, a set of starting values for the second solution usually can be readily derived. A curvature in the $\vec{R}$ plane may make one solution have a significantly larger error in the residual sets, but a slight $\vec{R}$ curvative could not be relied on to resolve the ambiguity. If multiple tracks of an orbital object can be obtained, thus giving

different $\vec{R}$ planes, this ambiguity could be resolved. For a suborbital object, if two radars track the same object simultaneously, then two $\vec{R}$ planes would be generated to resolve this ambiguity. Otherwise, the two solutions may remain equally valid, unless some special a priori conditions can be invoked.

The greatest problems with iterative schemes often are in terms of ambiguities other than coplanar $\vec{R}$, particularly those due to the periodic nature of the model functions. It is usually very important to have highly accurate starting values of rotation rates for convergence to a correct parameter minimum.

3.6 CONVERTING $\Delta\dot{R}$ TO CROSS RANGE

The ΔR function gives a projected target extent along the $\vec{R}$ axis as a direct measurement. If rotational motion parameters are known, a $\Delta\dot{R}$ function may be converted to a cross range function which may similarly give a measure of target extent, but along an axis orthogonal to the $\vec{R}$ vector. In the analyses of Section 1, the targets are assumed to simply rotate about an axis orthogonal to $\vec{R}$, and it is shown that multiplying the values of $\Delta\dot{R}$ ($= f_d \lambda/2$) by $1/\Omega$ (Ω = rotation rate) converts a $\Delta\dot{R}$ scale to a cross range scale. In more general cases, an effective rotation rate, Ω_e, must be used which will differ from Ω if $\vec{R}$ is not orthogonal to the rotation axis, as is shown in the following discussion.

Even if there is spin and precession (or if more complex modes exist), a resultant single angular rotation rate and direction may be determined at one instance in time, although this resultant rotation vector may change at other times. Therefore, at any one instant, a target may be viewed as simply rotating, and the results of the analysis in Section 3.2 may be useful in determining an effective rotation rate for a cross range scale conversion for that instant. If we assume $\beta = 0$ in the equations of Section 3.2, then $\vec{D}$ will represent general point extensions orthogonal to the rotation axis. In this case, (3-24) becomes

$$\Delta\dot{R} = \Omega D \sin\kappa \sin(\Omega t + \alpha) \tag{3-93}$$

By examining the geometry leading to (3-24), it may be seen that $D\sin(\Omega t + \alpha)$ is the projection of $\vec{D}$ onto an axis orthogonal to both $\vec{R}$ and $\vec{\Omega}$ and represents a cross range of the point scatterer. From (3-93),

$$\text{Cross Range} = D \sin(\Omega t + \alpha) = \frac{\Delta\dot{R}}{\Omega \sin\kappa} \tag{3-94}$$

The factor $1/(\Omega\sin\kappa)$ may then be seen in (3-94) as the value required to convert a range rate scale to cross range for $|\kappa| \neq 0$. An effective rotation rate may then be given by

$$\Omega_e = \Omega \sin\kappa \qquad (3\text{-}95)$$

The requirement to obtain the effective rate is that the instantaneous total rotation vector of the body be known. In practical data processing, this rotation vector must not change significantly during the integration span needed to resolve scatterers in Doppler frequency. The cross range resolution and ambiguity formulas of Section 1 may be applied if Ω_e is used instead of Ω and if the rotation angles are correspondingly modified. In Section 1.3b, $\Delta\Theta_T$ and $\Delta\Theta_s$ may be replaced by effective values $\Delta\Theta_{Te} = \Delta\Theta_T \sin\kappa$ and $\Delta\Theta_{se} = \Delta\Theta_s \sin\kappa$.

In the case of a rotating $\vec{R}$ and a rotating body, the same forms for effective rates and projection lines may be used if the rotation vector in the calculations is that of the resultant relative rotation between the body and $\vec{R}$. These modifications are discussed in more detail in Section 4.4 in reference to two-dimensional images.

For an axially symmetrical, precessing and spinning target, a somewhat different interpretation of effective rotation rate may be alternately given. In this case, there are only slipping reflection points on the target. Spinning motion about the axis of symmetry will not affect the $\Delta\dot{R}$ function, which is dependent only on the precession rate. Therefore, the equivalent motion is that of a target simply rotating at the precession rate about an axis parallel to the angular momentum vector, but with the symmetry axis tilted away from the rotation axis by the precession angle. In this interpretation, the effective rotation rate will not change during the precession cycle if $\vec{R}$ is fixed, unlike the case of using the vector resulting from both spin and precession components. (However, it must be remembered that if there are fixed points in addition to slipping points, then the fixed points will not scale properly in terms of true cross range extents.) The differences in the two interpretations for symmetrical objects include not only a different rate but also a different direction of the line

onto which the scatterer extents are projected to give the cross range measurements. This line is still orthogonal to $\vec{R}$, but, since it also must be orthogonal to the rotation vector, different rotation vector directions will give different projection line orientations.

Section 4 — Coherent Wideband Image Relationships

SECTION 4

COHERENT WIDEBAND IMAGE RELATIONSHIPS

4.1 OVERVIEW

Two-dimensional radar imaging concepts are introduced in Section 1, where it is generally assumed that the target is simply rotating about an axis orthogonal to the radar line-of-sight. In this section, the concept of the first-order wideband image is reviewed and discussed further. The emphasis is on image projection plane orientations and cross range conversion factors when the radar line-of-sight is not orthogonal to rotation axes and target rotation is not simple. A further discussion of extended surface responses is given, and the concept of multiple ray effects is also introduced.

4.2 REVIEW OF TWO-DIMENSIONAL IMAGING

Two-dimensional images of radar targets may be formed in a number of different ways. If a radar antenna aperture is wide enough in two dimensions, a narrow beam might scan a three-dimensional scene in two angles (in a search-light mode) and the intensity of signals at each beam position could be recorded on a raster or grid on an oscilloscope and photographed. The image from such beam scanning with a radar would be similar to an optical image of a view from the same direction as the illuminating source. A common flash camera photograph would give this type of optical image. The image projection plane is then orthogonal to the illuminating source.

If the radar aperture gives resolution in one angular dimension only, and if slant range resolution is sufficiently fine, a scene could be scanned in one angle, and signals could be displayed in angle and slant range. The effective projection plane would be parallel to the illuminating source direction. The common plan position indicator (PPI) display of signals from a rotating radar scanning a target area has an effective projection plane of this type. An optical analogy would be a photograph of an object with the flash or other light source directed orthogonally to the camera viewing direction. Since the camera

still resolves the scene in two angular dimensions, while the radar uses slant range resolution to replace one of the angles, the analogy is not exact, but the projection effects could be quite similar.

The radar systems of primary concern in these discussions are those which have apertures too small to allow a direct form of angular resolution for the target of interest. A radar system may be considered to have one other dimension, besides the two angles and slant range, in which resolution may be obtained, and that is Doppler frequency. Thus, the display of signal intensity in a two-dimensional frame of slant range and Doppler frequency might be considered an image of basic radar information independently of antenna aperture effects.

If different reflectors move independently of each other, this range-Doppler image will indicate only the slant range and Doppler of the reflectors. However, if the reflectors are related, additional interpretations might be made.

As has been discussed in Section 1, the Doppler frequency dimension may be converted to a target cross range dimension under certain conditions that include having scattering elements of the target rigidly connected and having relative rotation of the target as the source of Doppler spreading of the signals. This relative rotation may be effected by either the radar antenna moving relative to the target, or by actual target motion relative to the radar, or both. It is assumed that relative translational motion effects are removed from the signals and the only residual motion effects are those due to rotation.

Rotating the target about a fixed axis relative to a fixed radar gives equivalent signals to those obtained if the radar moved in a circle with a center fixed in a nonrotating target. (This concept is illustrated in Figure 1-19.) Thus, the data collected in a sequence along an arc of the circle may be stored as if they were received from an array of several antenna elements and can be used to form a much wider equivalent aperture than the single antenna used to collect the data. A very narrow beam may be formed and scanned in a phased array sense, with a display of signals in angle and slant range possible in the form of the PPI display. The resulting image projection plane is then parallel

to the illumination direction and orthogonal to the rotation axis. The projection plane is also parallel to the plane of the line-of-sight vectors ($\vec{R}$). This viewpoint of rotating target signal processing leads to the term "synthetic aperture" imaging which has been used to describe the type of high resolution radar maps of terrain made by radars in moving aircraft. Synthetic aperture terrain mapping has been performed for many years and was the precedent for imaging of rotating space objects. In most terrain mapping operations, the aircraft antenna moves along a straight line and thus there is an aspect change of the antenna relative to the fixed ground features.

In space object analyses, it has generally been found more convenient to specify requirements for cross range resolution at the target in terms of relative rotation angle rather than in terms of synthetic aperture beamwidth resolution, although equivalent forms may be derived. As was shown in Section 1, cross range resolution is theoretically inversely dependent on relative aspect change, $\Delta\theta_T$, regardless of how that aspect change occurs in time. In practice, there may be concern about time spans because of possible instabilities in a radar system or in the propagation media between radar and target. The aspect angle variation with time would also be important if equispaced data samples are required for algorithms like the FFT.

In the simple case of relative rotation of the target about an axis orthogonal to the line-of-sight, an analyst can determine over what integration time, T, the radar signals should be integrated through resolution formulas, such as $R_{cr} \simeq \lambda/2/\Delta\theta_T$ (as discussed in Section 1) where $\Delta\theta_T = \Omega T$ and Ω is the rotation rate. Since Fourier transforming will usually be of equispaced time data, the Doppler frequency scale is readily calibrated from the time between samples. Doppler frequency may then be converted to cross range through the multiplication factor $\lambda/2/\Omega$, and the processed signals can be displayed in intensity modulation form within properly scaled slant range and cross range frames. If $\vec{R}$ is not orthogonal to the effective rotation axis, then Ω may be modified as Ω_e, which will be discussed further in Section 4.3. Knowing the correct Ω_e, the same procedure would be followed to estimate integration time and scale factors as with Ω in the simpler case.

For a nonorthogonal and changing $\vec{R}$ and for more complex motion conditions, aside from the scale factor estimate, a difficult problem may be the determination of the orientation of image projection planes relative to each other within a body-fixed coordinate frame. Estimation of these parameters will be considered quantitatively in Section 4.4. However, another, more qualitative, view of the problem, which may be helpful in visualizing the projection plane orientations, will be discussed in Section 4.3.

A discussion of range-Doppler or synthetic aperture imaging of model range targets is given in Appendix A, which is a report explaining the use of this type of processing in analyzing the sources of scattering on a target, with examples from measurements. This report considers only the case of the target rotating about an axis orthogonal to the radar line-of-sight. Explanations of the digital signal processing are given in the main text, together with illustrations of input data and output results (see Appendix A, Figures 1 and 2). The processing of space object data for images can be made very similar to that used for the model range target data. The significant addition to the processing is the removal of translational motion effects. This compensation consists of an approximate alignment of the wideband amplitude envelopes and the phase shifts so that the resulting data appear as if derived from a target rotating about a fixed point. In model range data, this alignment was automatically present since the target rotated about a fixed axis. (Translational motion compensation is discussed in more detail in Section 1.6.)

In an addendum to Appendix A, illustrations of images from measurements of three simply shaped targets are given: (1) a cube, (2) a thick cylinder, and (3) a thin rod. These clearly illustrate the presence of localized scattering centers on targets and show how the range-Doppler image can be viewed as an orthogonal projection of reflection effects which locate target outline positions. Any one image frame does not give a complete sense of the target shape, but images from different mean aspect directions, including specular aspects, will tend to give a more complete outline. The addendum also shows how the position and amplitude of edge effect scattering can be predicted from asymptotic high frequency scattering theory in cases where the edges are sharp and well

defined. As stated before, however, the model range relative rotation geometry represents only special cases of the general conditions which may be encountered in practical space object tracking.

4.3 UNIT SPHERE CONCEPT OF IMAGE PLANE ORIENTATION

In first-order synthetic aperture imaging, the objective is to obtain a two-dimensional projection of scattering effects. The requirement is that there be a relative aspect change between radar and target. The further requirement is that the radar line-of-sight, $\vec{R}$, remain parallel to a common reference plane relative to a body-fixed coordinate system. The angular changes in $\vec{R}$ positions will determine the actual image projection plane, i.e., scattering effects will project orthogonally onto that plane.

In practical space object tracking problems, $\vec{R}$ will not generally remain parallel to a common target reference plane. However, there may be only slight deviations from coplanarity over shorter sections of a track, and the approximate image plane orientation may be allowed to change as the track proceeds. The problems of the analyst in creating a set of images may be stated to include: (1) a determination of the aspect changes of $\vec{R}$ relative to the target, (2) a determination of whether the coplanarity condition is sufficiently satisfied during different parts of a track to allow imaging with the necessary cross range resolution, and (3) a determination of the relative orientations of the image projection planes for different parts of a track.

The concept of a unit sphere plot of $\vec{R}$ may aid in the visualization of the problems, particularly the projection plane orientation. A target rotating about an axis orthogonal to the $\vec{R}$ vector may be used to represent a single target track. In this case, $\vec{R}$ projects on the unit sphere as a great circle arc as suggested in the sketch of Figure 4-1. The $\vec{R}$ vectors are all coplanar. A radar image may be considered in terms of an integration of signals from points along an arc

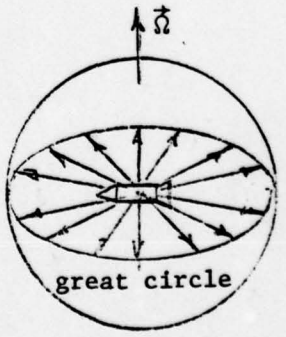

Figure 4-1

segment of the circle. Whatever the position of this arc, the image projection plane normal remains constant because of the $\vec{R}$ coplanarity. The mean $\vec{R}$ direction for an arc segment integration would determine the slant range axis of an image frame, and the cross range axis would be orthogonal to slant range. For different mean $\vec{R}$ positions, the projection of the target may appear to rotate relative to $\vec{R}$, but the basic shape of the projected outline would not change. Therefore, it would be valid to take a set of images from different $\vec{R}$ positions, rotate them about an axis parallel to the plane normals so that the projected outlines coincide and then superpose the set. Different parts of the target could be illuminated for different $\vec{R}$ directions, so that the composite could allow a more complete outline sense than any one image frame.

Now let the $\vec{R}$ vector make an angle κ with respect to the rotation axis. The unit sphere trace of $\vec{R}$ is now not a great circle arc and the $\vec{R}$ vectors are not coplanar, but form a cone with half-angle κ, as shown in Figure 4-2. Then the radar signals may be integrated over small segments of the arc, and the image projection plane for that arc may be considered as the plane tangent to the $\vec{R}$ cone at the line of the mean $\vec{R}$ for the integration span. Under these conditions, one can see that the image projection plane normal must change as different arc segments of signals are integrated, i.e., as the target rotates. Because of this change, the orthographic projections of the target outline must change, and it is not valid to simply superpose sets of images from different parts of the rotation cycle of the target when $|\kappa| \neq 90°$. The more realistic tracking case would be to allow $\vec{R}$ to change with time. As a simpler example, let $\vec{R}$ slowly rotate about an axis orthogonal to the body rotation vector $\vec{\Omega}$, so that κ varies linearly with time from $\kappa = 90°$ to $\kappa = 0°$. Then the trace of $\vec{R}$ on the unit sphere would be a spiraling path as suggested in Figure 4-3. The image projection plane normals from such a track would vary over a very wide range of directions. Images for regions of small $|\kappa|$ values would be superposable. Images from other aspects

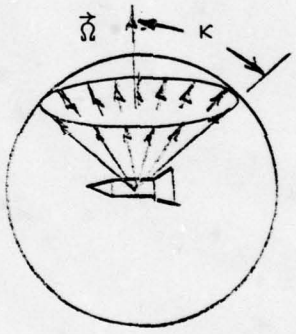

Figure 4-2

would have to be studied without the benefit of superposition. Different features may be revealed for different aspects, so a full set of images could be useful even if superposition is not possible.

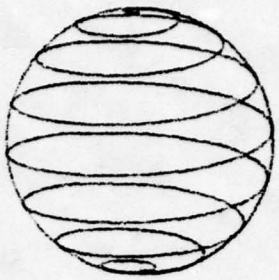

Figure 4-3

(Theoretically, signals from all aspects may be integrated coherently, but in the general form this image is three-dimensional. Space object tracking data have not been amenable to this type of processing.)

In the case of stabilized, near-earth satellite targets, an $\vec{R}$ trace generally follows an approximate great circle arc, although the rates of $\vec{R}$ change along that arc. The image projection planes may deviate slightly from coplanarity and superpositions would have certain distortions or smearings because the target outline projections could not be made to coincide, but image interpretations generally might not be difficult. A more complex case would be that of a slow body rotation comparable to the $\vec{R}$ rates. Then the $\vec{R}$ path may take on a somewhat irregular path as suggested by Figure 4-4, and projection planes could vary in a variety of directions.

Figure 4-4

Similarly, with spinning and precessing bodies, if the spin rate is fast relative to the precession rate and $\vec{R}$ rate, there might be a complex version of the spiraling effect suggested in Figure 4-3. The $\vec{R}$ vector would rotate rapidly about the spin axis, but an effective κ variation would be slower and κ would have an oscillation with the precessional motion of the spin axis. Comparable spin, precession, and $\vec{R}$ rates could make the $\vec{R}$ trace on the unit sphere very complex and image effects very difficult to interpret.

4.4 CALCULATIONS OF PROJECTION PLANE ORIENTATIONS AND SCALE FACTORS

4.4a Simple Rotation

To determine image plane orientations and scale factors, rotational motion parameter estimates must be available. The parameters may be calculated by various estimation techniques like the specular timing method that is well known for symmetrical targets in noncoherent SOI work, or from the range and range rate data fitting methods suggested in Section 3. Otherwise, the body parameters may be specified from a priori assumptions such as those that might be made for certain attitude stabilized objects.

If a target has been determined to be simply rotating, it will be assumed that a rotation vector, $\vec{\Omega}_T$, will be specified in an inertial frame, such as the celestial or inertial geocentric coordinate (IGC) system. Then for a selected signal integration time span, T, the radar line-of-sight unit direction vector, $\vec{R}$, will also be specified in the same inertial framework. Vector $\vec{R}$ may be converted from the usual azimuth and elevation angle data obtained during a track. A mean direction, $\vec{R}_m$, may be specified by taking the value of $\vec{R}$ at the mean time of the integration span, or by averaging the first and last $\vec{R}$ positions across the span. An approximate $\vec{R}$ rate, $\dot{\vec{R}}_m$, may be estimated by taking first differences of $\vec{R}$ about the mean time, for example by taking the initial, $\vec{R}_i$, and final, $\vec{R}_f$, values to obtain

$$\dot{\vec{R}}_m \simeq \frac{\vec{R}_f - \vec{R}_i}{T} \tag{4-1}$$

An approximate rotation vector, $\vec{\Omega}_R$, for $\vec{R}$ can be obtained from

$$\vec{\Omega}_R = \vec{R}_m \times \dot{\vec{R}}_m \tag{4-2}$$

(as was discussed in Section 2.3d).

Now the parameter which will determine the instantaneous range rates and, therefore, the instantaneous Doppler shifts of scattering centers is the resultant relative rotation vector component orthogonal to the instantaneous value of $\vec{R}$. The latter will be approximated by $\vec{R}_m$. The resultant relative

rotation vector, $\vec{\Omega}_{TR}$, between the target and the radar line-of-sight is equal to the difference between the two component velocities, or

$$\vec{\Omega}_{TR} = \vec{\Omega}_T - \vec{\Omega}_R \tag{4-3}$$

If $\vec{\Omega}_T = \vec{\Omega}_R$, there is no relative aspect change and imaging is not possible. The component of $\vec{\Omega}_{TR}$ orthogonal to $\vec{R}_m$ will be the rotation vector, $\vec{\Omega}_e$, which is significant to the imaging process. As illustrated in Figure 4-5, $\vec{\Omega}_e$ may be obtained from

$$\vec{\Omega}_e = \vec{R}_m \times (\vec{\Omega}_{TR} \times \vec{R}_m) \tag{4-4}$$

and

$$|\vec{\Omega}_e| = |\vec{\Omega}_{TR}| \sin\gamma \tag{4-5}$$

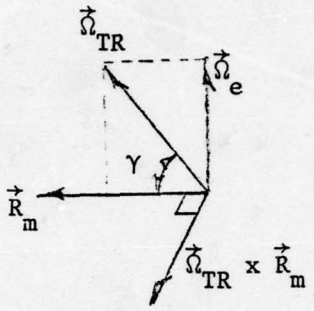

Figure 4-5

The magnitude of $\vec{\Omega}_e$ gives the effective rotation rate, Ω_e, needed to convert Doppler frequency to cross range and to determine the needed integration time for a specified cross range resolution. The direction of $\vec{\Omega}_e$ defines the normal to the image projection plane.

One can see readily that, if $\vec{\Omega}_{TR}$ is parallel to $\vec{R}_m$, Ω_e will be zero and imaging will not be possible. For a slowly varying $\vec{R}$, this condition would be equivalent to the "swinging bridge" aspect in more conventional SOI work.

If a rotating line of the target, such as a symmetry axis, is specified by another vector, $\vec{D}$, then it may be desirable to determine the projection of that line in the image plane. The image slant range axis direction is given by $\vec{R}_m$. The cross range axis direction, $\vec{R}_{cr}$, can be specified by

$$\vec{R}_{cr} = \vec{R}_m \times \vec{\Omega}_{eu} \tag{4-6}$$

where the unit rotation vector, $\vec{\Omega}_{eu}$, can be given by $\vec{\Omega}_e / \Omega_e$ to define the image plane normal. Then the components of $\vec{D}$ on $\vec{R}_{cr}$ and $\vec{R}_m$ will locate the line in the image plane according to

$$D_{sr} = \vec{D} \cdot \vec{R}_m$$

$$D_{cr} = \vec{D} \cdot \vec{R}_{cr} \qquad (4\text{-}7)$$

which is sketched in Figure 4-6.

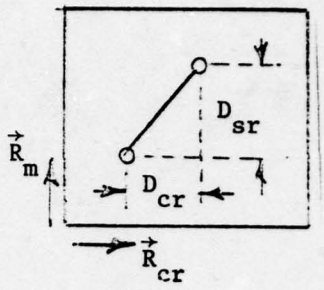

Figure 4-6

By treating all points on a target outline through a specification of $\vec{D}$ vectors, an outline of the target can be projected onto the radar image plane for any arbitrary orientation of the image projection plane. This type of projection can be very useful when a configuration estimate is made based on a limited set of measurements and it is desirable to check the results more closely by coordinating outline estimates with a large number of image responses. Not only might an initial outline estimate be checked, but also various other target features might be related more readily than could be done without a reference outline.

4.4b Stable Body Cases

Space objects are sometimes stabilized in attitude within a specified coordinate system. If stabilized in an inertial system, then the Section 4.4a estimate of $\vec{\Omega}_e$ and the projection parameters can be obtained simply by setting $\vec{\Omega}_T = 0$ in all of the formulas. The $\vec{R}$ rotations alone control the image plane orientations and scale factors.

For an earth-oriented body, a coordinate system can be arranged relative to an orbital plane position and a line towards the earth's center. As an example, if $\vec{\Omega}_p$ is the normal vector to the orbital plane as might be obtained from ephemeris data or directly from the radar tracking data, and $\vec{E}_n$ is the unit vector direction from the satellite to the earth's center, orthogonal to $\vec{\Omega}_p$, and similarly obtained, then the third axis could be given by $(\vec{E}_n \times \vec{\Omega}_p)$. The radar line-of-sight vector components along these three axes can be calculated and the image parameters estimated in exactly the same manner as the inertially stable case. The difference will be that the earth-oriented case will have a reference

axis rotation, once per satellite orbital revolution. If the target is a satellite which maintains its attitude stability from pass to pass, then image projections planes can be related from pass to pass to obtain a more complete view of the target. In the earth-stabilized cases, only bottomside illuminations are possible if stability is maintained, so shadowed topside regions of a target may remain undetermined. If the satellite has some distinguishing features in its outline, a test might be made on the true attitude stability by checking outline projections in frames from pass to pass. For example, if a number of overhead passes are observed, the projection geometry should be constant and, therefore, the same image responses should be seen. A variation in these image projections would indicate target changes between passes.

4.4c Slow Rotation Cases

Slowly rotating space objects generally give the most difficulty in obtaining rotational motion parameter estimates. A general approach when the estimates are unavailable is to create images as if the target were inertially stable. If the body rates are slow enough, the image orientations may be approximately those of a stable body, particularly in the regions of track where line-of-sight rates are fastest. For faster body rotation rates, the interactions of $\vec{\Omega}_T$ and $\vec{\Omega}_R$ can produce a complex set of image effects in the sense that both the cross range scale factor can be in error, which gives a projection distortion and the image plane orientation can vary in an unestimable manner. An example of a simulation of such effects is given in Figure 4-7. The example consists of projected outlines of a cube, as if imaged at the time of the overhead point and at several points of decreasing elevation angle during the orbital track. The effective body rotation period was about 10 minutes. The bottom row of projections in Figure 4-7 represents image effects if the body rotation parameters were known and therefore give true orthographic projections of a cube outline. The top row of projections is distorted relative to the bottom row because the assumed cross range scale factors based on inertially stable attitude conditions were incorrect. Without additional information, the analyst may only very roughly sense the target configuration and specify some dimensions in the slant range direction as minimum dimensions. Dimensions along the cross

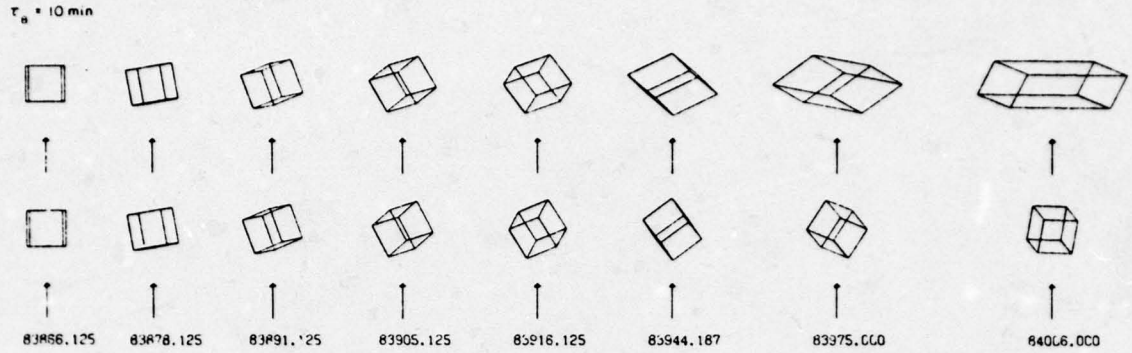

IN EACH SET, SIMULATIONS ON THE LOWER LINE HAVE BEEN CORRECTLY SCALED; THOSE ON THE UPPER LINE HAVE BEEN SCALED EMPLOYING THE INCORRECT ASSUMPTION OF INERTIAL STABILITY.

Figure 4-7

range dimension would be considerably more doubtful because of the unknown scale factor.

4.4d Spin and Precession

The concept of using an instantaneous rotation vector estimate to establish imaging parameters as defined for simple rotation in Section 4.4a is also theoretically applicable for more complex motions. In the review of spinning and precessing bodies in Section 3.1, spin rate, ω_s, and precession rate, ω_p, components of rotational velocity were defined in terms of the precession angle θ and ratios of moments of inertia according to (3-13). The instantaneous total rotational velocity, $\vec{\Omega}_T$, would then be the sum of $\vec{\omega}_p$ and $\vec{\omega}_s$, as sketched in Figure 4-8, and falls between the two vectors at an angle γ from $\vec{\omega}_s$. Then $\vec{\Omega}_T$ precesses about the total angular momentum vector, which is parallel to $\vec{\omega}_p$, in synchronism with the spin axis precession. If $\omega_p << \omega_s$, then γ is nearly equal to zero and imaging might be carried out as if the spin direction changed a negligible amount during a spin cycle. The problem might be treated as in the simple rotation case, but with the κ angle changing slowly, as was discussed in Section 4.2 for the unit sphere concept. With more comparable rates, ω_p and ω_s,

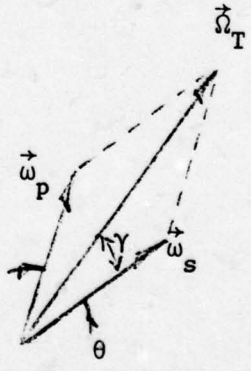

Figure 4-8

the projection relationships become even more complex. However, if the motion parameters are specified, then at least theoretically the image projection plane scale factors and relative projection plane orientations are calculable. A possible problem might be that the change in $\vec{\Omega}_T$ direction may be too fast for the $\vec{R}$ coplanarity condition to hold long enough for an aspect change which allows a meaningful cross range resolution value.

4.4e Axially Symmetrical Targets

If a target is truly axially symmetrical, then image processing may be carried out in at least two different ways. One approach would be that derived for more arbitrarily shaped targets as discussed in the preceding sections based on the calculation of an effective rotation vector, $\vec{\Omega}_e$. Then the images could be interpreted in terms of various projection plane attitudes relative to the target. Slipping point effects may be noticeably different than fixed point effects, but the general effect of varying outline projections would be present for more arbitrary relative motions.

However, since the scattering effects are independent of roll angle and dependent only on the angle, ϕ, between the line of sight, $\vec{R}$, and the symmetry axis direction, $\vec{S}$, a second approach could give images with a somewhat different interpretation. In this approach, the angle ϕ could be calculated as a function of time and the signals could be integrated as a function ϕ as if the target symmetry axis were simply rotating, or tumbling, about a fixed axis orthogonal to $\vec{R}$. This could be done independently of how the body rates and $\vec{R}$ rates changed, as long as segments of data with smoothly varying ϕ functions of time could be found. If equispaced angle samples were required, there would also be the problem of nonlinearly varying ϕ, so that an FFT type of transform algorithm may not be valid. However, if a set of images over a wide range of ϕ values could be formed, then a fairly complete outline of the symmetrical target may be obtained from a superposition of image frames. As in all these problems, the success of such a superposition could depend on a well-defined set of rotational motion parameters on which the ϕ calculations could be based.

4.5 EXTENDED SURFACE AND INDIRECT RAY SCATTERING

4.5a Surface Speculars

The concept of localized reflection centers has been found generally valid in approximating most scattering effects from targets that are large relative to wavelength. Reflection effects in a set of radar images within limited aspect angle variations do regularly appear as if arising from the same limited number of points although the apparent point locations and numbers may change over large aspect variations. These types of effects may be termed direct ray point scattering.

Extended surfaces that are flat or singly curved, such as flat plates or cylinders, tend to have dominant scattering localized at surface discontinuities at most aspect angles. However, at specular aspects large areas of an illuminated surface reflect signals with significant amplitude rather than just the discontinuity regions. At flat plate specular aspects, elements of the entire illuminated surface reflect equally. Cylinder surface scattering is dominated by elements in about the first half wavelength of depth along the incidence direction. Thus, surface specular effects may still be viewed in terms of direct reflections from target points but with the points uniformly distributed across an effective surface area. For two-dimensional images, the flat or singly curved surface specular effects become equivalent to line arrays of scatterers along line projections of the target surface. Figure 4-9 illustrates nonspecular and specular scattering from model range measurements of the same cylinder model discussed in the addendum of Appendix A. Also shown are the results of using the well known physical optics model for cylinders. The specular responses can be seen to spread across the entire length, approximately centered on the leading line of the cylinder outline. A second example of specular response is shown in Figure 4-10 for a small rocket-like model, about 17 inches long, based on measurement data from the same General Dynamics (GD) radar system used for the cylinder model. The flashes for the cylinder and cone appear in separate image frames, since the specular flashes appear at significantly different angles. The response function for the cone appears concentrated toward the large radius

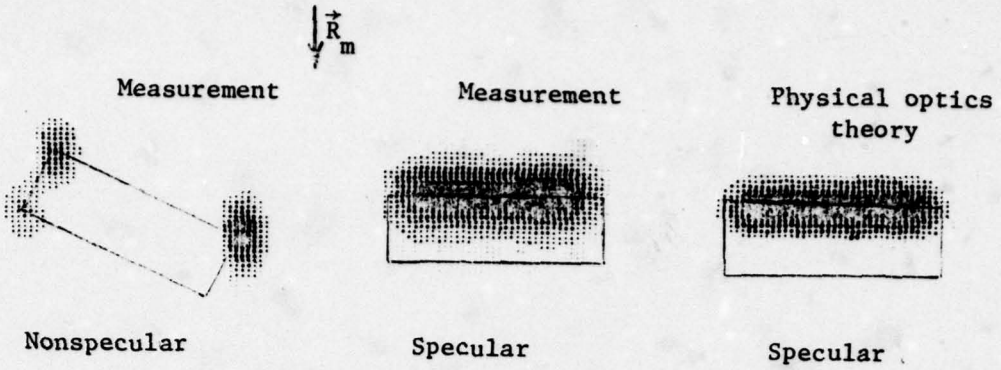

Figure 4-9

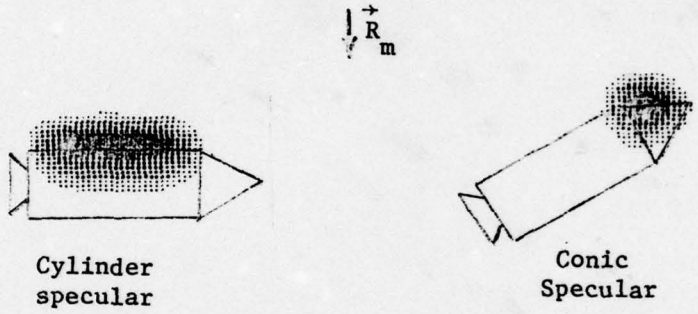

Figure 4-10

regions because elemental surface scattering amplitude is proportional to the radius of curvature for singly curved surfaces. A final example of specular responses is shown in Figure 4-11, which was from GD measurements of a stepped cylinder model, about 25 inches long. The specular flash responses in Figure 4-11 clearly separate the two cylinder sections and the smaller diameter cylinder shows a lower intensity than the large diameter section, as might be expected. In Figures 4-9 through 4-11, the incidence direction is indicated by $\vec{R}_m$. The slant range extent of the specular responses is mainly dependent on the transmitted pulsewidth and not the diametrical target extent.

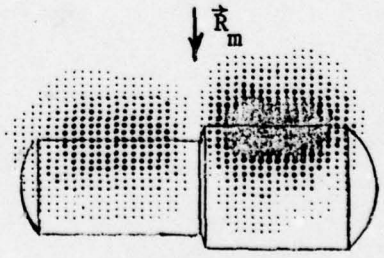

Figure 4-11

A thin long rod element, like an antenna, might not be detectable from just the nonspecular end point responses because the amplitudes are too low in terms of available radar dynamic range, relative to reflections from other parts of the target to which the element is attached. Then the high amplitude specular flash effect may be the only means of detecting such an element, and if a wide range of aspects to the target is observed, finely spaced images may be useful in a search for such elements.

4.5b Indirect Rays

In the direct ray point scattering concept, ray paths follow from the radar to a target reflection point and then back along the same path to the radar. Direct rays are suggested in the sketch in Figure 4-12 to explain the edge responses of the cylinder model of Figure 4-9.

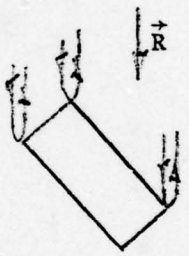

Figure 4-12

Other types of scattering are sometimes encountered which can be described in terms of rays striking one element or discontinuity on the target, then being diffracted in directions that lead to other points on, or within, the target before finally returning to the radar. The return paths may retrace the arrival paths or may be entirely different. Extraordinary examples of multiple path ray responses are illustrated in the Addendum of Appendix A from the long thin rod model. One of these ray paths is retraced in Figure 4-13, wherein the near end is reached first, the ray is guided along the rod length to the far end, and then reradiated back to the radar from the far end. Another ray path can be formed by some of the energy diffracted at the far end to be redirected back up the rod and reradiated to the radar from the initial near-end point. In theory, there are an infinite number of paths in various combinations of multiple

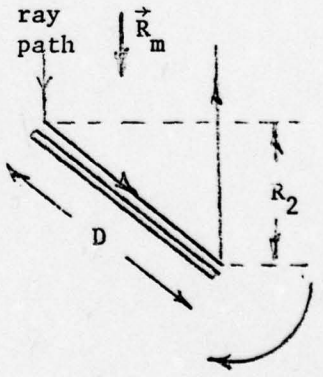

Figure 4-13

bounces between the rod end points, but the reradiated energy decreases with the number of bounces, so only a limited number can be observed with a practical system, as is noted in the Appendix A results.

Multiple ray respones tend to appear with image amplitude pulse shapes like those of direct ray responses. However, they generally appear outside the outline bounds of the actual target along the slant range direction as can be seen in the thin rod results in Appendix A. They must appear within the cross range bounds of the target.

If the multiple ray paths are known, the multiple ray response point locations in an image frame can be readily estimated. The slant range position of such a point is equal to the mean path length traversed in the round trip, and the cross range position corresponds to the time derivative of the mean path length (divided by the rotation rate, Ω, for the usual calibration factor). As an example, consider the rod ray sketched in Figure 4-13. The total length, R_T, of the ray path relative to point 1 is

$$R_T = D + R_2 \tag{4-8}$$

and the mean path length, R_{T2}, is

$$R_{T2} = \frac{R_T}{2} = \frac{D}{2} + \frac{R_2}{2} \tag{4-9}$$

The length D is a constant as the rod rotates, so the derivative of R_{T2} is simply

$$\dot{R}_{T2} = \frac{\dot{R}_2}{2} \tag{4-10}$$

since $\dot{R}_2/\Omega$ would give the cross range location of a point at the end 2 of the rod, the ray cross range location must be midway between 1 and 2 according to (4-10). Therefore, from (4-9) and (4-10), the ray response location can be stated as a point midway along the rod in cross range but extended in slant range from the midpoint by a distance equal to half the rod length, as illustrated in Figure 4-14. The measurement results in Appendix A agree with this analysis.

Another example of an interesting multiple ray effect was found in the images of the small rocket model of Figure 4-10 at near nose-on aspects. A

sample image is shown in Figure 4-15, where a response point may be noted near the bottom of the right hand side of the target, but away from the actual target outline. The path corresponding to this ray is also illustrated in the figure. The ray is believed to have been diffracted first by the cone cylinder-join, then guided along the cylinder surface to the back cylinder edge and reflected from the small cone nozzle surface in a specular sense, and finally returning to the radar along the same path as it entered. The response point is located in cross range at the same position as the front diffraction edge of the cone-cylinder join because the path length in the round trip to the back edge does not vary with aspect change beyond that point. The slant range position is determined by the path length to the rear conic. The multiple ray response disappeared in other image frames of this target at aspects where the front diffraction edge was shadowed. The shadowed nozzle conic section is believed to be a very significant reflector because, in the simple cylinder

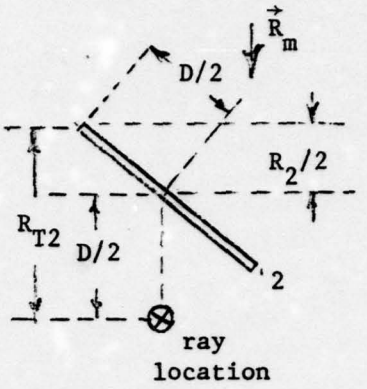

Figure 4-14

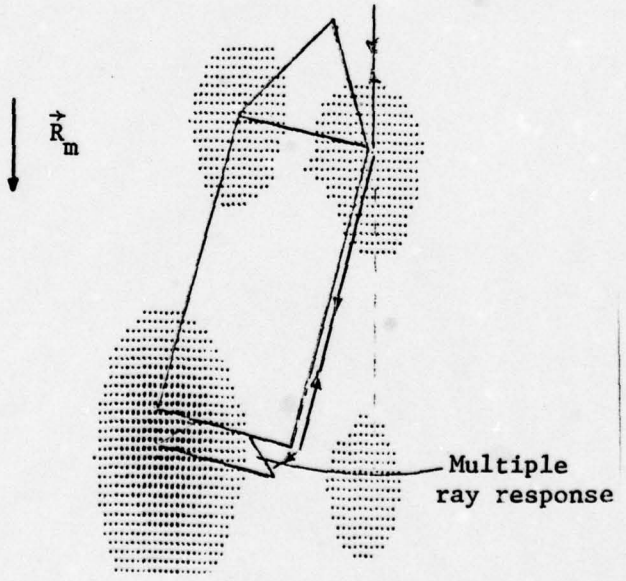

Figure 4-15

model images, this type of multiple ray effect, which could theoretically appear through diffraction from the shadowed cylinder edge alone, was not detectable.

Multiple ray phenomena can more often be expected in practical space object tracking from targets with some hollowness or cavity-like formations into which rays may enter and bounce about before reradiating outward. Such ray paths can follow internal specular surfaces, as well as diffracting edges, and the specular effects can give more significant reflection amplitudes than edge effects. The engine sections of rocket bodies covered by a cylindrical or conical fairing might form such cavities. Also, a conical rocket nozzle itself can have multiple ray effects in which specular flashes can be obtained from an inside wall that is shadowed from direct rays.

In general, multiple ray effects tend to be identifiable in radar images of unknown targets if they are observed at different aspect angles. The multiple ray responses do not rotate with the target in a rigidly connected point sense as do the direct ray responses. A common effect is that the ray appears as if it were a point on the end of a string in a pendulum sense, as may be noted in the example in the Figure 4-15.

Appendix A – SRC TR 70–150

APPENDIX A

RADAR TARGET SCATTERING DIAGNOSIS WITH WIDEBAND MEASUREMENTS AND COHERENT PROCESSING

This appendix was originally prepared as a separate report, SRC TR 70-150, and is reproduced herein in its entirety for easy reference.

TABLE OF CONTENTS

LIST OF ILLUSTRATIONS

LIST OF ILLUSTRATIONS (Continued)

LIST OF ILLUSTRATIONS (Continued)

LIST OF TABLES

RADAR TARGET SCATTERING DIAGNOSIS WITH WIDEBAND MEASUREMENTS AND COHERENT PROCESSING

OVERVIEW OF SCATTERING ANALYSIS

Practical purposes of analyzing the radar reflection characteristics of an object include the derivation of parameters for use in designing radar detection and discrimination systems and conversely, the design of objects which may become targets of such systems. Two general methods of analysis of a target configuration are (1) theoretical simulations of reflections using digital computers for detailed analysis, (2) direct measurements of full scale or small scale models with radar systems having the required parameters. Concentration on one of these approaches may become necessary because of the other's limits of applicability. Considerations include: costs of computer implementation, costs of model construction, requirements of accuracy, and necessary variations in parameters. Both methods have mutually exclusive practical limitations which tend to make them complementary when a large variety of problems is included, but for a particular problem, one of the approaches may indeed be better. The following is a brief comparison of methods. The intention is to give a context for use of wideband coherent measurements in synthetic aperture imaging applications to this problem.

Digital computer analysis of complex target configurations can require boundary matching techniques which become impractical because they demand a too large computer storage and a too long computer running time. This condition occurs as body dimensions increase from the order of a wavelength. The computer method does potentially have a flexibility advantage in convenience of changing body parameters, target orientations, and radar operating conditions. Measurement methods require constructing new configurations with target parameter changes and some degree of change in radar systems with each set of radar operation changes. In

measurement systems, complex target attitude variations are not easily achieved directly. However, measurements do not introduce the concern for effects of approximation assumptions such as spacing and number of matching points on a body. Practical measurement systems do not allow an unlimited target size, but acceptable target extents are generally greater in a measurement system than would be presently feasible in digital computations if point matching solutions are needed. With static measurement systems there is a concern for target support and background influence on data, in addition to antenna field effects and other electrical and mechanical system errors.

Digital simulations can compete in the case of larger shapes if the target configuration has major scattering effects arising from localized regions (e.g., edges and specular reflection surfaces) for which there are generalized scattering coefficients (e.g., geometric diffraction theory, physical optics theory). Such asymptotic formulations which are available tend to be limited in the kinds of localized configurations they describe, and in the degree of applicability for a given configuration. Their main application has been to first order, direct ray reflections. Their use in secondary, multiple ray tracing tends to become complex and more questionable as the numbers of localized scattering effects increases. However, in many problems the first order theories have been applied with powerful effect.

With high resolution measurement systems there can be an opportunity to analyze the larger targets with the localized scatterer approach, but without all of the assumptions of first order theory. The application of first order theory to localized regions for which such theories are available can be checked with measurements results and localized effects for which theories are not available can be empirically studied. The isolation of effects may considerably reduce complexity, with results which may be applied to systems in which the target configuration is unresolved with a simple addition of component reflections.

Wideband, coherent measurements can allow such target resolution in two dimensions. The bandwidth is used to allow an isolation of effects in slant range within areas that are fractions of an overall body dimension. If in addition to amplitude, phase is recorded from a rotating target, further processing of the wideband signals can be carried out to synthesize the effects of a wide antenna aperture in which a high degree of equivalent angular resolution in one dimension can be added to the slant range resolution to allow isolation of target regions in a two dimensional projection. One version of such processing is the first order synthetic aperture (backscattering) image. This is approximately a projection of localized scattering amplitudes onto a plane which contains the radar line-of-sight and which is also perpendicular to the plane containing the axis of body rotation and the line-of-sight. It represents a display of mean doppler versus mean slant range of scattering points on the target during short intervals of target rotation. In the case of axially symmetrical configurations, rotation about an axis perpendicular to the symmetry axis would tend to be sufficient for complete diagnosis of a target model. For an unsymmetrical shape, rotation about different axes to establish three dimensional locations of scattering effects might be possible. The processing for two dimensional images has been thoroughly studied in the problem of terrain mapping with signals from a moving aircraft, in which the effect is a rotation of the radar system about the target, the converse of the static measurements radar method. The more recent development of very wideband radar systems which have slant range resolution of the order of a few inches has allowed the technique to be useful in the analysis of the smaller, discrete targets such as missiles and satellites.

To summarize the application of wideband, coherent measurements, the results become especially meaningful when target dimensions are of at least a few wavelengths, the results are applicable directly when wideband radar systems are involved, and the results can also be useful in narrowband system problems. Isolation of scattering effects on an extended target to localized regions will allow direct locations of major sources of scattering

in a target design, including isolation of secondary effect such as multiple reflection rays.

The following discussions will describe a method of utilizing digitally recorded data from a backscattering model measurements range in generating synthetic aperture images in which target scattering effects can be localized. A set of results for three different target models is given in an addendum as an example of studies which might be made with this type of processing.

FIRST ORDER SYNTHETIC APERTURE PROCESSING

First order processing here implies assumptions that include scattering occurring from ideal, isotropic points on a target and signal processing matched only to a phase variation model corresponding to linear motion of a point during an integration interval. Theoretical relationships are derived in the addendum study, with examples which illustrate the applicability of the assumptions. This section will be limited to a discussion of some practical details of measurements and a few sample displays of data.

Figure 1 illustrates a model measurements arrangement and two samples of amplitude data displays. The target of this example is a small rocket model on a single axis rotator. A very short pulse of approximately Gaussian shape is transmitted. High speed sampling techniques are used to create from several transmitted pulses a digital record of a data sweep covering a fixed slant range gate. In-phase (I) and quadrature (Q) coherent detection of signals allows a measure of both amplitude and phase of the target. Data sweeps equispaced in target angle are recorded as the target rotates. A sample plot of the amplitude part of the data from several sweeps is shown in Figure 1 in a 3-D type of display. A calibration target is included in each sweep to permit calibration of target signals in terms of radar cross section. A sample intensity modulation plot of amplitude is also shown in Figure 1 which gives a sense of variation in slant range of reflection centers as the target rotates through slightly more than a half cycle. (The signal at broadside during this recording was quite high, saturating the receiver and also displaying the range sidelobes of the transmitted pulse.)

Figure 2 illustrates the method of processing the digital data to obtain two dimensional target images (amplitude of intensity modulation is really a third variable, or dimension) of the synthetic aperture form. A

C12973

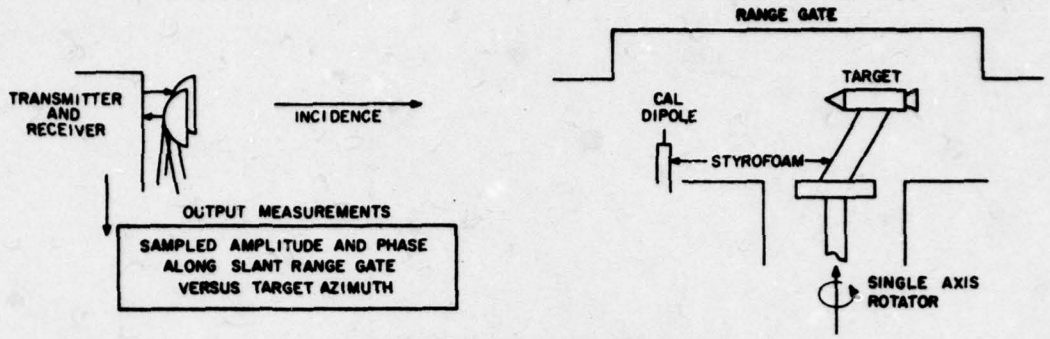

(a) MODEL RANGE MEASUREMENTS

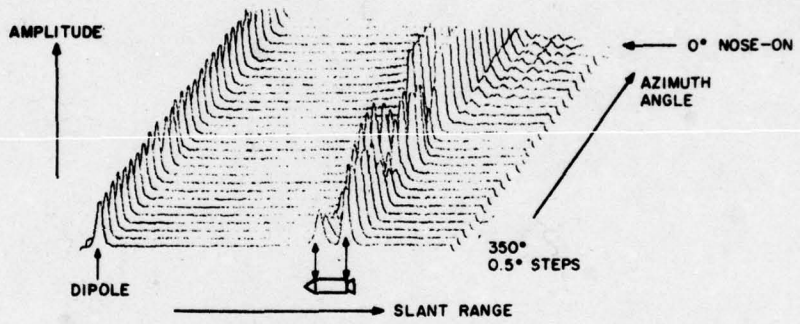

(b) 3-D PLOT OF DIGITAL AMPLITUDE

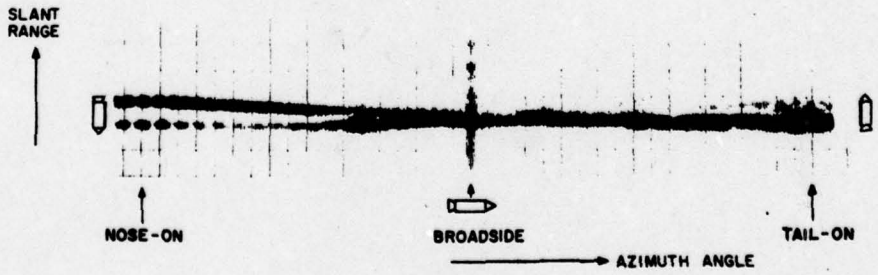

(c) RANGE-TIME-INTENSITY (RTI) PLOT OF AMPLITUDE
(PORTION OF TOTAL RANGE GATE SHOWN)

Figure 1. Illustrations of Measurement System and Signal Displays

A12974

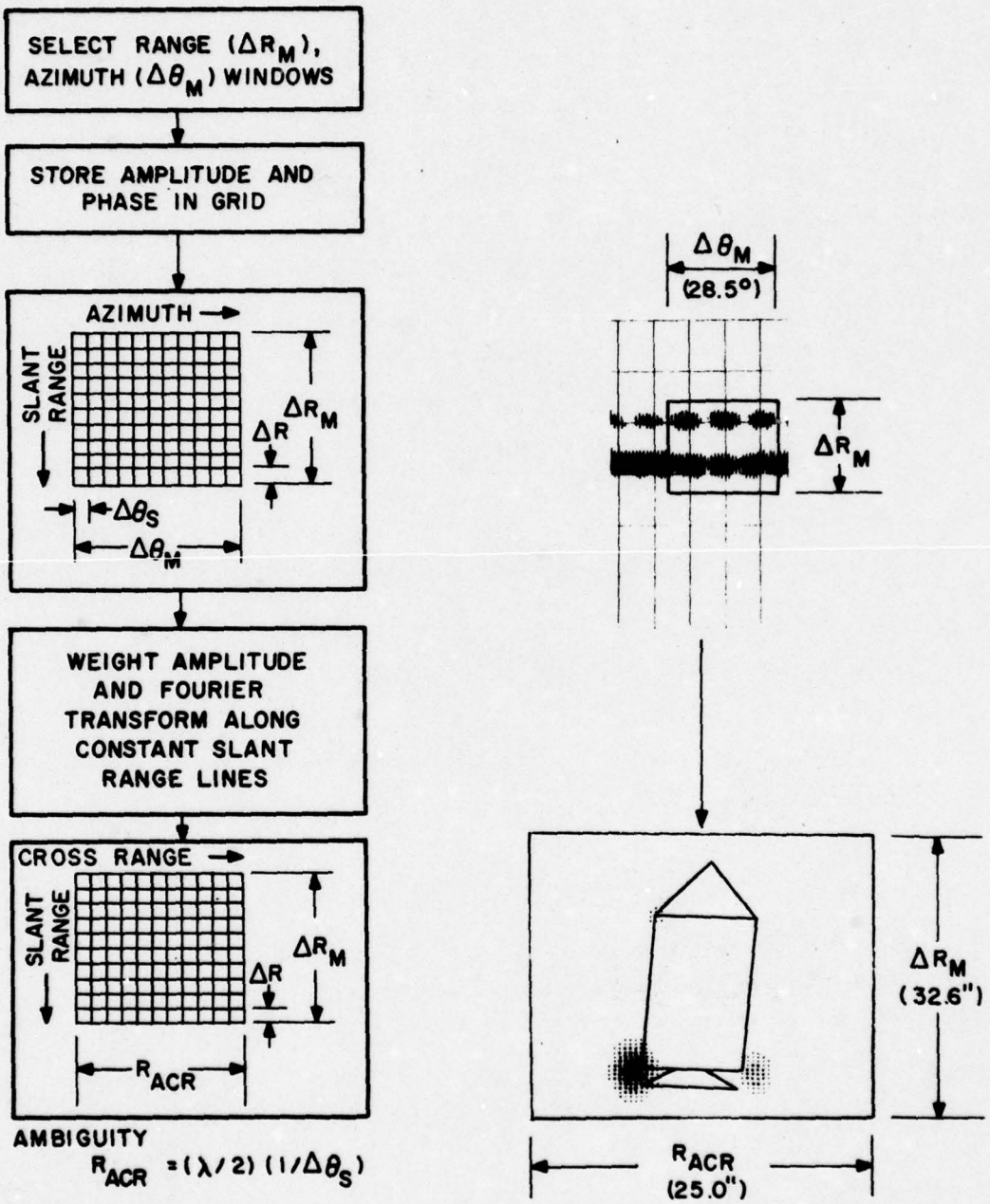

Figure 2. First-order Image Processing

certain region of recorded data is selected from the slant range gate and data for a number of aspect angles are entered into a computer storage grid which has dimensions of slant range and target azimuth angle. At constant slant range lines, data are amplitude weighted to reduce response sidelobes and Fourier transformed (aspect angle as the variable). The output result is then in the form of a grid which has the original slant range scale, but the azimuth angle dimension becomes a cross range scale. For the sample displays of Figure 2, a set of data centered slightly off the nose-on condition was selected for imaging. The number of input angle positions was 19, and the number of slant range samples was 64. A "Fast Fourier Transform" algorithm was used with 45 zeroes added to the 19 input points so that the transform output included an effective interpolation yielding 64 points. The intensity modulation was achieved with a six level quantization and five printed dots of varying diameter and a blank. (There is some distortion in this synthetic aperture image example because display scales were not equal, a matter of convenience in using a computer printer format.) Scattering is clearly isolated into four main target regions.

The data of Figures 1 and 2 were from measurements on a General Dynamics system at Fort Worth, Texas. Data have also been processed from a system at Syracuse, New York, operated by General Electric.

The following is a compendium of independent studies applying the synthetic aperture technique to measurements of a small cube, a thick cylinder, and a thin rod. The addenda are presented without reference to the preceding explanation. These studies include checks of measurement results with first order theoretical formulations and include approximate formulations of magnitude of error due to the first order assumptions of the processing.

ADDENDUM

APPLICATION OF SYNTHETIC APERTURE TECHNIQUES IN RADAR TARGET SCATTERING ANALYSIS OF A SMALL CUBE, THICK CYLINDER, AND THIN ROD

APPLICATION OF SYNTHETIC APERTURE TECHNIQUES IN RADAR TARGET SCATTERING ANALYSIS OF A SMALL CUBE, THICK CYLINDER, AND THIN ROD*

ABSTRACT

Scattering center effects in radar images of three simple target shapes were studied by using wideband radar data from rotating target models. Digital recordings of amplitude and phase data versus slant range at uniformly changing aspect angles were processed with a general purpose digital computer to produce synthetic aperture radar images giving two-dimensional resolution. Ray effects associated with surface discontinuities were isolated from a 3 inch (7.62 cm) aluminum cube, a 7 inch (17.78 cm) diameter by 21 inch (53.34 cm) length aluminum cylinder, and a 0.1 inch (0.254 cm) diameter by 24 inch (60.96 cm) length steel rod. The measurements were made on a General Dynamics system having a 9.0 GHz center frequency and about a 3.5 inch (8.9 cm) resolution in slant range. There was good agreement in comparisons of resolved signal amplitudes associated with edge discontinuities to estimates from first-order wedge diffraction theories for the cube and cylinder. Thick cylinder model data clearly indicated the presence of a ray type echo appearing by way of a shadowed region in addition to the expected direct rays associated with illuminated edges. In the steel rod images at least six isolated rays associated with direct and multiple paths could be detected, but all amplitudes were considerably lower than those of the ideal conductor thin wire theory used in comparison. The results illustrate the power of an added dimension of resolution through coherent signal processing of short pulse data in empiric scattering analysis and the practicality of applying digital techniques when target dimensions are limited.

*This work was sponsored by Rome Air Development Center, Air Force Systems Command, Griffiss Air Force Base, New York.

INTRODUCTION

Synthetic aperture techniques are most familiar in the application of terrain mapping from moving aircraft, but applications have also been suggested for isolated targets under other radar configurations [1]. This paper presents results of application of such techniques in digital processing of amplitude and phase data recorded from rotating targets illuminated by a stationary X-band radar having a wide bandwidth transmitted signal. The objective was to isolate scattering effects with resolution in a cross range as well as slant range dimension and compare results to those obtained from well known monochromatic formulations based on first order, high frequency diffraction theories. The three targets included a 3.0 inch (7.62 cm) cube, a thick cylinder, 7 inches (17.78 cm) in diameter by 21 (53.34 cm) inches long, and a long thin rod, 0.1 inch (0.254 cm) in diameter by 24 inches (60.96 cm) long. The first two models were of aluminum material; the rod was of steel.

The outputs of the processing included intensity modulation displays, which will be called "radar images", and also quantitative listings of amplitude data. The latter were used to derive radar cross section values for peak response points by reference to calibration target signals, and these values were compared to equivalent theoretical estimates based on various first order formulations [2] – [8], as summarized in Appendix A.

MEASUREMENTS RADAR SYSTEM

The radar measurements were made at a General Dynamics facility in Fort Worth, Texas on a system which could transmit a pulse of width between 3 and 4 inches (7.6 to 10.2 cm) in equivalent slant range (3 dB power points) at a 9.0 GHz (3.3 cm wavelength) center frequency. Sampling point intervals were at a minimum of 0.51 inch (1.3 cm) in slant range. At each range point an integrated video amplitude value and a pair of in-phase and quadrature amplitudes were recorded in a series of over 450 points representing a range sweep. The targets were moved on a single axis rotator with a styrofoam column target support. Sets of range samples were recorded at equispaced intervals of rotation angle. Separate parabolic antennas gave a slight bistatic angle, but the data were treated as from a monostatic system.

Processed data from two sets of linear polarizations are presented here for each target. One set is designated HH for received and transmitted polarizations (E-field) parallel to the local horizontal; i.e., the target azimuth plane. The other is for orthogonal polarizations to HH and is designated VV. A calibrated dipole reference target gave a basis for radar cross section estimations in both polarization sets. Accuracy of radar cross section estimation presented in the following discussions is of the order of one dB, with errors introduced due to measurement methods and motion model assumptions in the digital signal processing.

FIRST ORDER SYNTHETIC APERTURE PROCESSING

The mechanics of the data processing included gating a set of complex numbers at equispaced range sample points from a magnetic tape recording for a series of equispaced target angle positions and storing these in a computer array. The data samples were Fourier transformed across the angle dimension at constant slant range points after suitable amplitude weighting for sidelobe suppression.

Linear approximations of motion of points on a target were assumed in setting the cross range scales and determining resolution parameters. A brief derivation of these relationships can be obtained if a point target is considered rotating in an X-Y plane about an orthogonal axis centered in the X-Y system. Let radar incidence direction be parallel to the Y axis and let rotation of a line of length D from the center of rotation to the isotropically scattering point make an angle θ with the X axis. At some instant of the rotation, let the angle θ be θ_o and deviations from θ_o be equal to $\Delta\theta$, or

$$\theta = \Delta\theta + \theta_o \tag{1}$$

If the center of rotation is a displacement phase reference point, the slant range distance from this point can be given by

$$r = D \sin\theta \tag{2}$$

and the phase angle of the point for a single frequency can be given by

$$\phi = -2kr \tag{3}$$

where $k = 2\pi/\lambda$ is the wave number, λ the carrier wavelength. The first order linear approximation for r can then be given by

$$r = D \sin\theta \approx D(\sin\theta_o + \Delta\theta \cos\theta_o) \tag{4}$$

which can also be expressed as

$$r \approx Y_o + \Delta\theta\, X_o \tag{5}$$

where $Y_o = D \sin \theta_o$ and $X_o = D\cos\theta_o$ are the coordinates of the scattering point at the center angle θ_o. The signal from the point scatterer can then be described by the unit amplitude phasor

$$\epsilon^{-j2kr} \approx \epsilon^{-j2k\,(Y_o + X_o\,\Delta\theta)} \tag{6}$$

The location of Y_o in this first order approximation is assumed already available through the slant range resolution, and Fourier transforming with respect to $\Delta\theta$ can give the cross range location X_o. In the results presented here, the Hamming type of amplitude weighting was applied before transforming which was of the form

$$w(\Delta\theta) = 0.54 + 0.46 \cos\,(2\pi\Delta\theta/\Delta\theta_m) \tag{7}$$

where $\Delta\theta_m$ is the total angle span centered on θ_o. This weighting gives the transform of (6) a cross range equivalent pulse width at 3 dB power points equal to

$$\Delta R_{cr} = (1.3/\Delta\theta_m)\,(\lambda/2) \tag{8}$$

"Fast Fourier" algorithms were used in the computer analyses with power-of-two transform lengths. The sampling of data resulted in a cross range unambiguous dimension given by

$$R_{acr} = (\lambda/2)/\Delta\theta_s \tag{9}$$

where $\Delta\theta_s$ is the increment between angle samples.

All of the data presented here were obtained by processing a set of 19 angle sample points. In Fourier transforming the data, the output in cross range was increased to 64 units by adding zeroes to the 19 sampled point input arrays. The slant range dimension included 64 input samples

from the recorded data to give a final output image array of 64 by 64 points.

The amplitudes in the 64 by 64 array were presented in frame format by a computer printer with six printer characters, including a blank, representing six quantization levels. The upper five levels were stamped over with round dots of varying diameter in proportion to the signal level to give an intensity modulation effect. The output amplitudes were also available numerically and proper peaks were selected with aid of the intensity modulation images to estimate radar cross section values for significant scattering centers.

Magnitude of response of a moving point in the synthetic aperture image based on the above signal processing model will decrease with distance from the rotation center because the phase of the point is nonlinear and the pulse envelope moves in slant range during an integration interval. Appendix B gives approximate estimates of these integration losses as functions of distances moved through cross range and slant range resolution cells, derivations based on an ideal Gaussian pulse shape. These indicate that the integration loss errors in cross section values presented in the following discussions are within about 0.6 dB or less. Resolution values are also affected, and Appendix B derivations indicate that the above ideal cross range resolution is increased by about 8% or less for the limiting regions on the three target models. The values of amplitude and resolution are stated in the following without corrections for integration loss.

SMALL CUBE

The cube model was measured as it rotated about an axis perpendicular to two faces. Thus radar incidence was perpendicular to at least three illuminated edges at all aspect angles. Radar images for two different aspects from the measured data are presented in Figures 1 and 2 for HH and VV polarizations. The cross range processing included 19 angle samples in 2.0 degree increments giving a total angle span of 38 degrees about each center position. For these values the above linear theory formula gives a cross range resolution of about 1.3 inches (3.3 cm). The theory gives a cross range increment for Figures 1 and 2 of about 0.29 inch (7.37 cm). The slant range increment is 0.51 inch . Outline projections of the cube have been added in the figures to correlate peak signal areas with cube edges and these sketches are distorted according to these scale increments. (Retention of the unequal scale distortions was a matter of convenience in utilizing the available computer printer arrangement without further interpolations.) The blanking threshold for the Figure 1 and 2 displays is equal to 1/6 (or -15.5 dB) of the maximum output from the processor. Since each image has image intensity levels set relative to the maximum signal of a given frame, relative comparisons of peak intensities have meaning within a frame but between frames are not significant.

Radar illumination direction (and therefore slant range) is from the top of each image downwards and the results are somewhat analogous to an optical image if illumination were similarly from the top side of a frame toward the target and viewing was downward on the cube to observe the light reflections. For a highly polished cube, the optical image would tend to produce highlights at the corners, and with coarse optical resolution the resulting optical image might approach the radar image. This analogy is far from exact. A significant difference is that the radar signal is mainly from the illuminated edges perpendicular to the incidence directions and both top and bottom parts of the target contribute to the signal. The bottom is not blocked, as would occur optically. However, there is at least a tendency towards this

optical analogy, which makes it useful in inspection of the radar images.

Figures 1 and 2 clearly show that the dominant scattering effect can be described in terms of rays reflected from the illuminated cube edges perpendicular to the incidence direction. Distinctly different results are obtained with different linear polarization conditions. HH polarization tends to give more equal returns from the three edges while in VV polarization the leading edge is the main scatterer. Multiple rays would appear in these images at displaced slant range points if the same point received and reradiated the ray, and also at displaced cross range points if different points were involved in reception and reradiation. Such secondary ray effects are not clearly evident in the cube images. They would not be detectable if they were small in signal level because of either threshold or resolution limitations. The assumption in the following analyses is that intense regions in the images were mainly direct ray reflections.

Results in Figures 1 and 2 agree with theoretical simulations of the data as presented in Figures 3 and 4 which were based on first order wedge scattering theory as described in Appendix A. Short pulse scattering was simulated by assuming a band limited Gaussian type of pulse shape with main pulse width parameters approximately equal to those of the measurement radar, but without a match to range sidelobe effects. Thirty-one frequencies were used to simulate this theoretical pulse response in frequency. The formular of Appendix A was applied at the required set of pulse frequencies and aspect angles and weighted by the pulse response. These were then Fourier transformed to a time domain function after adding enough zeroes to give an interpolated time output of 64 points. The cross range processing of the samples was carried out as described for the measurements data. There are only slightly different relative intensity levels in comparing measured data images with the theoretical.

Assuming that the intense areas in the images indeed represent isolated returns from the associated cube edges, peak amplitudes were selected and converted to radar cross section values in units of dBsm (dB relative to one square meter). Table I gives a listing of observed cross section values for the three cube edges as defined by the sketch in Figure 5.

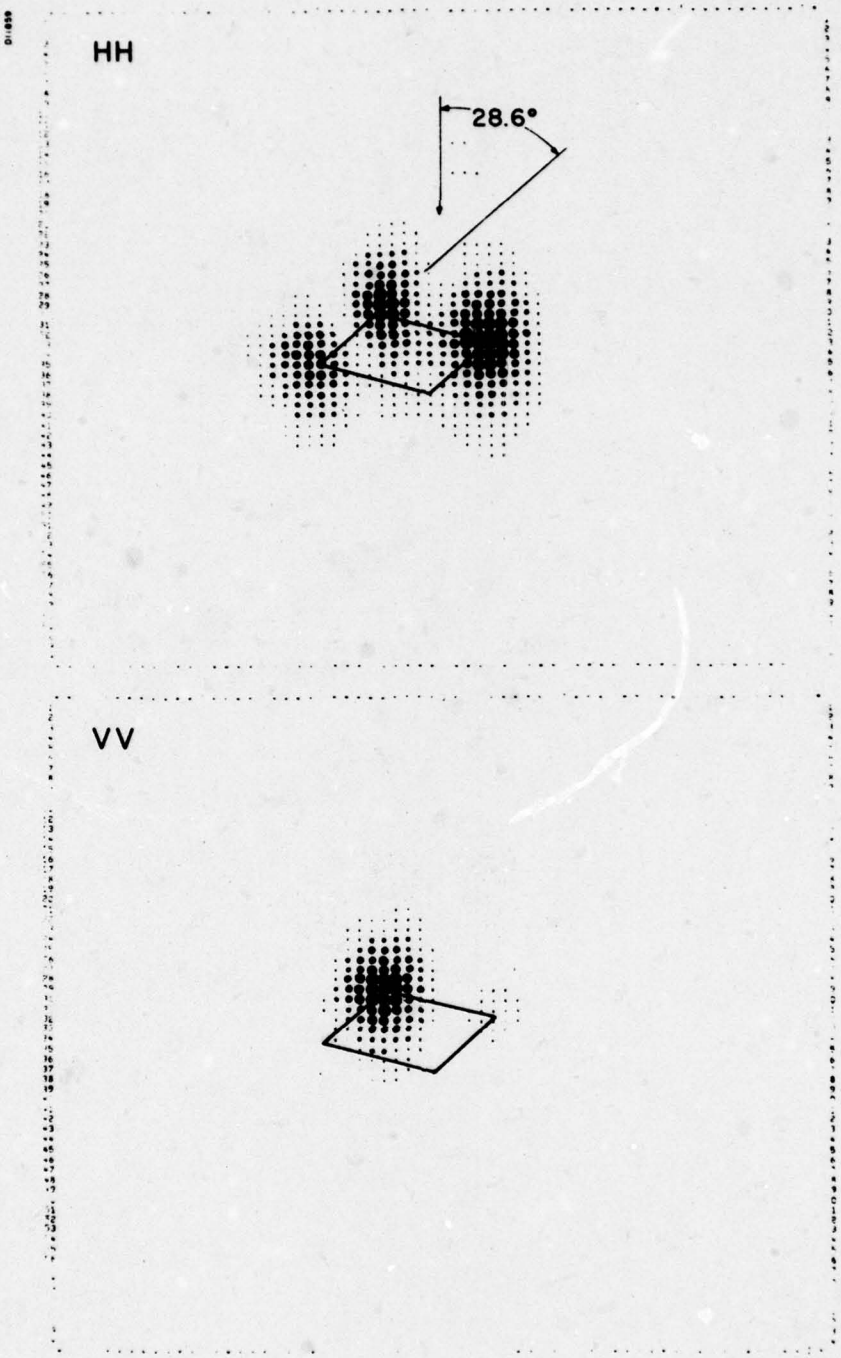

Figure 1. Radar Images of a Cube from Measurements Data, 28.6° Aspect, HH and VV Polarizations

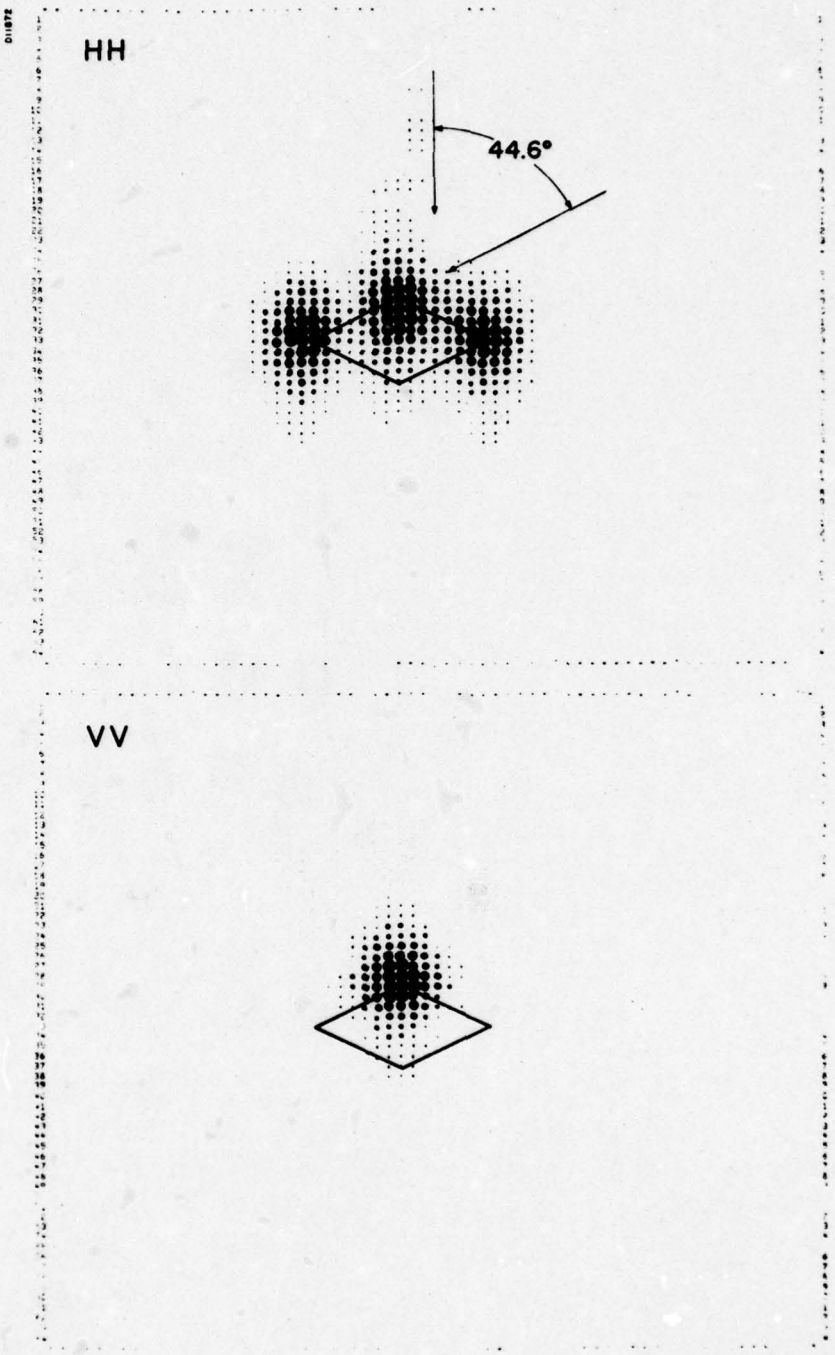

Figure 2. Radar Images of a Cube from Measurements Data, 44.6° Aspect, HH and VV Polarizations

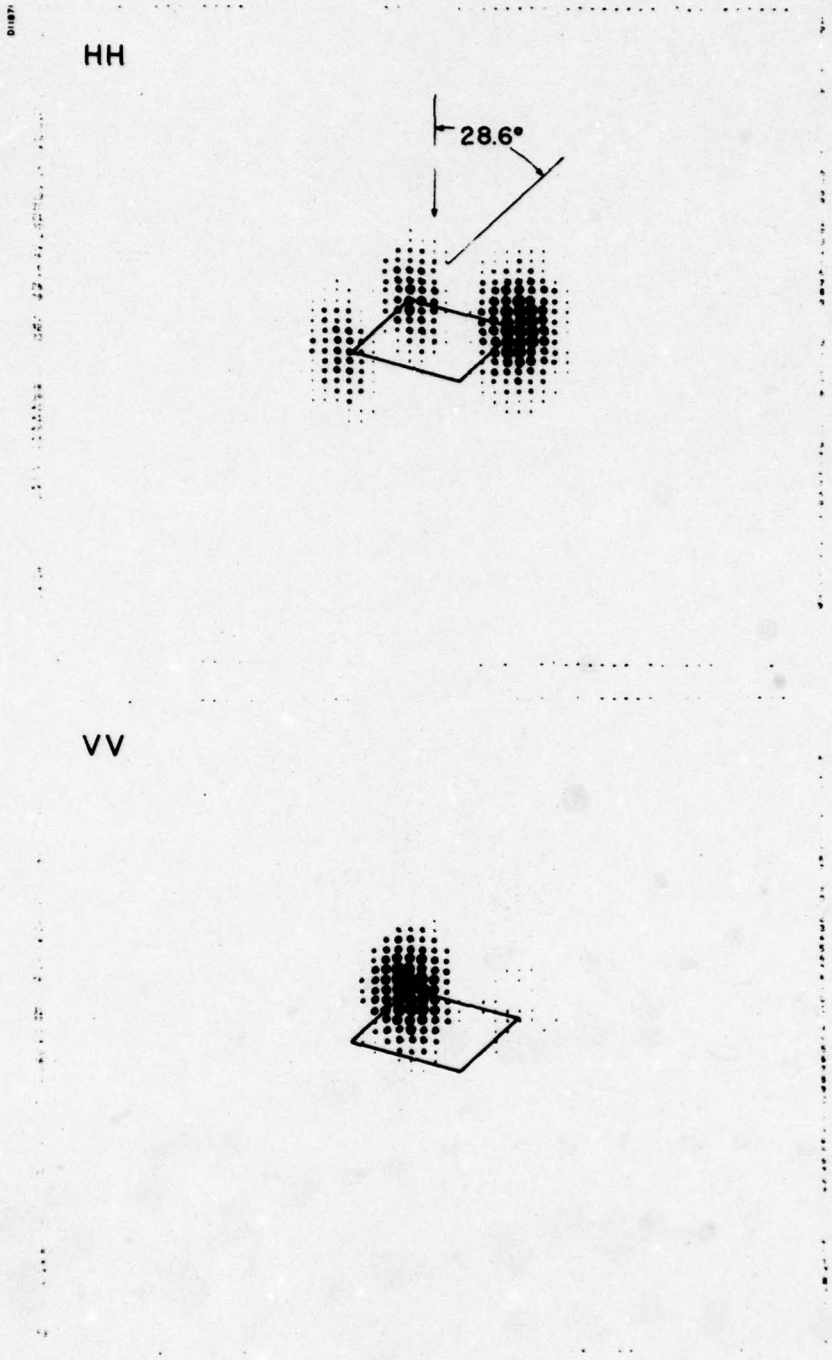

Figure 3. Radar Images of a Cube from Geometric Diffraction Theory, 28.6° Aspect, HH and VV Polarizations

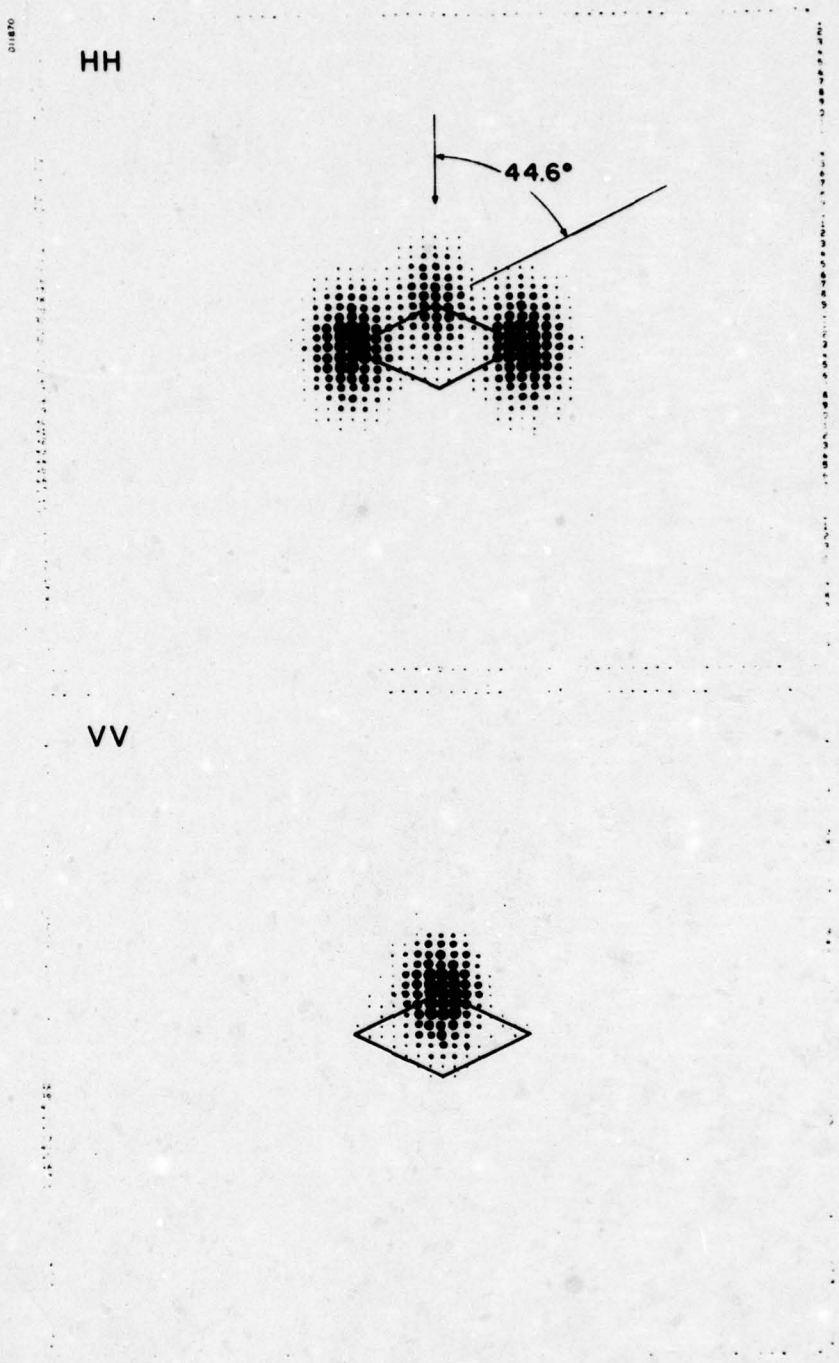

Figure 4. Radar Images of a Cube from Geometric Diffraction Theory, 44.6° Aspect, HH and VV Polarizations

Table I. Radar Cross Section Values in dBsm Versus Aspect Angle in Degrees for Cube Edges from Diffraction Theory and from Image Processing of Measurements

VV POLARIZATION						
Aspect	Edge A		Edge B		Edge C	
θ	Theory	Measured	Theory	Measured	Theory	Measured
28.6	-22.1	-21.0	-29.5	-34.4	-50.3	-50.0
44.6	-23.4	-22.6	-40.6	——	-41.0	——
60.6	-22.3	-21.2	-49.8	——	-32.3	-32.1
HH POLARIZATION						
28.6	-26.9	-27.6	-24.6	-26.7	-28.8	-29.1
44.6	-29.2	-28.0	-27.5	-28.4	-27.6	-29.2
60.6	-27.1	-28.1	-28.8	-28.7	-24.8	-24.8

A11876

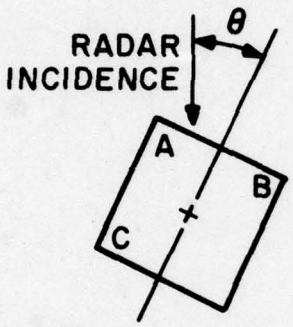

Figure 5. Sketch Defining Cube Edges and Aspect Angle

Figure 6 gives a plot of the measured data and average value curves from the theoretical function in Appendix A. Since a wide angle was involved in the coherent processing, the estimates must be considered as those approaching an averaged set rather than a fixed angle result. The measurement estimates were generally within a 1 dB deviation limit of the theoretical averages.

A11520

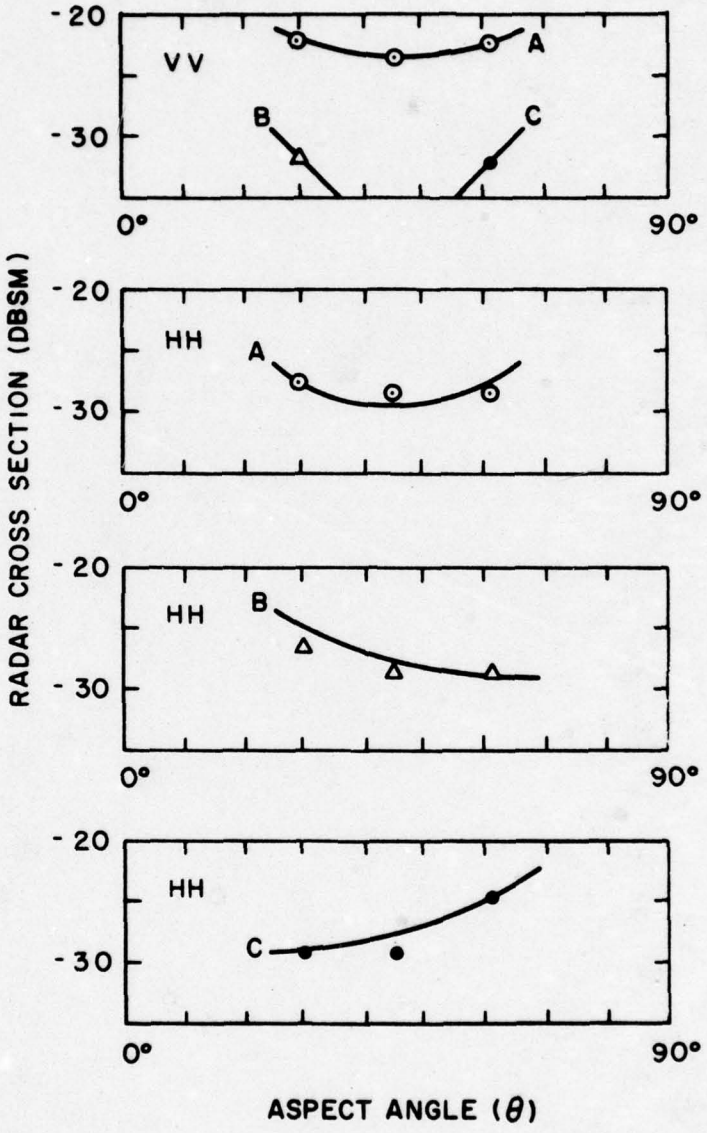

Figure 6. Plots of Radar Cross Section Estimates of Cube Edges from Image Processing and Theoretical Curves

THICK CYLINDER

The thick cylinder model was closed at both ends with flat plates mounted to form a sharp circular edge. Rotation was about an axis perpendicular to the cylinder axis. Figures 7 and 8 give the radar image results from the experimental measurements for two aspects, one near end-on, the second closer to broadside. These were obtained by processing 19 angle samples in 1.0 degree increments with slant range sampling at 0.51 inch (1.3 cm). Theoretical cross range resolution is then about 2.6 (6.5 cm) inches and the cross range increment is about 0.59 inch (1.5 cm). Sketches of the cylinder projection were added with only a slight skew since the display scales were of a less distorting ratio than in the cube figures. The results in Figures 7 and 8 show the expected three scattering centers associated with the three illuminated edge regions where the tangents to the edges were perpendicular to the incidence direction. The further (in slant range) edge responses are less intense in the VV cases than the HH cases.

A fourth echo source (first suggested by the General Dynamics investigators of amplitude only) was clearly present in the VV data processed from higher transmitter power levels. This is not present in the Figures 7 and 8 images because of the thresholding effect and lower transmitted power used in obtaining those data. Figure 9 gives images at two aspects in VV polarization from data obtained with a 20 dB higher transmitter power than in the measurements for the previous figures. The higher level signal caused receiver saturation distortion in Figure 9 for the leading edge regions, but at the far end an unsaturated pair of signal regions can be noted which include a return from the illuminated edge region and an apparent echo effect in the shadowed region. The latter is not predicted by first order theories, and was not detectable in HH polarization data. Near the end-on aspects, the fourth echo is stronger than that from the nearby illuminated edge, but near broadside it becomes relatively weaker. Because the intense region of the fourth scattering center is displaced in slant range from the actual cylinder edge in these images, a possible ray effect is indicated which would

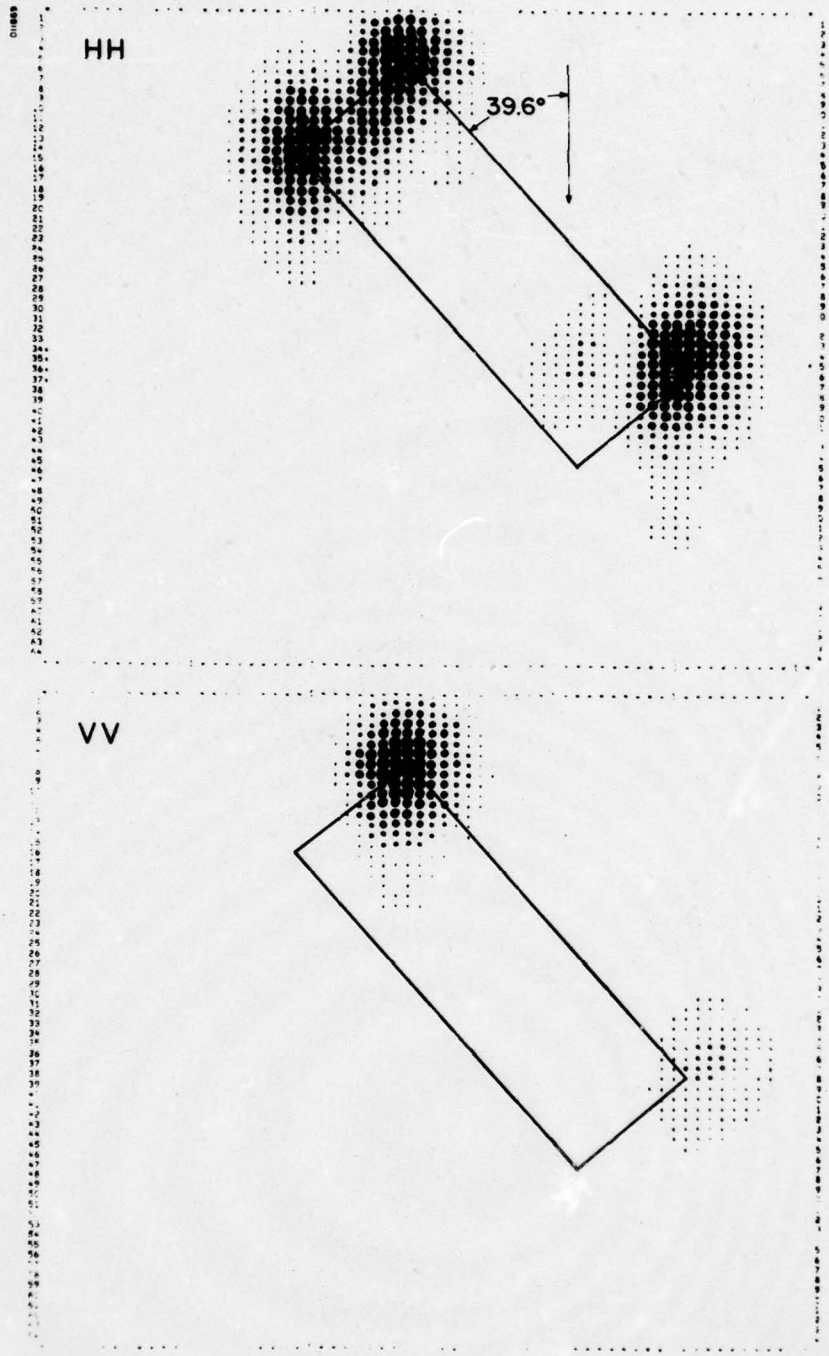

Figure 7. Radar Images of a Cylinder from Measurements Data, 39.6° Aspect, HH and VV Polarizations, -20 dB Transmitter Attenuation

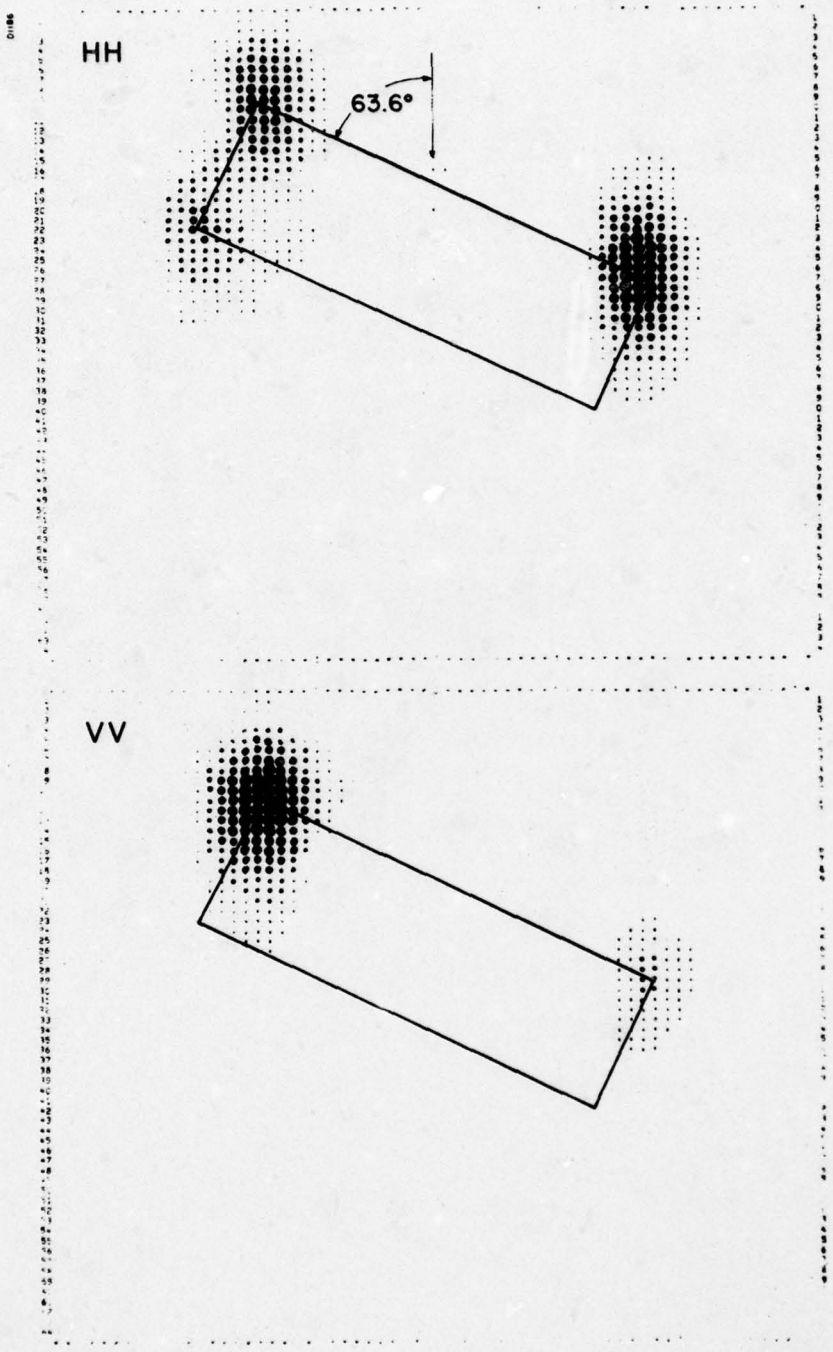

Figure 8. Radar Images of a Cylinder from Measurements Data, 63.6° Aspect, HH and VV Polarizations, -20 dB Transmitter Attenuation

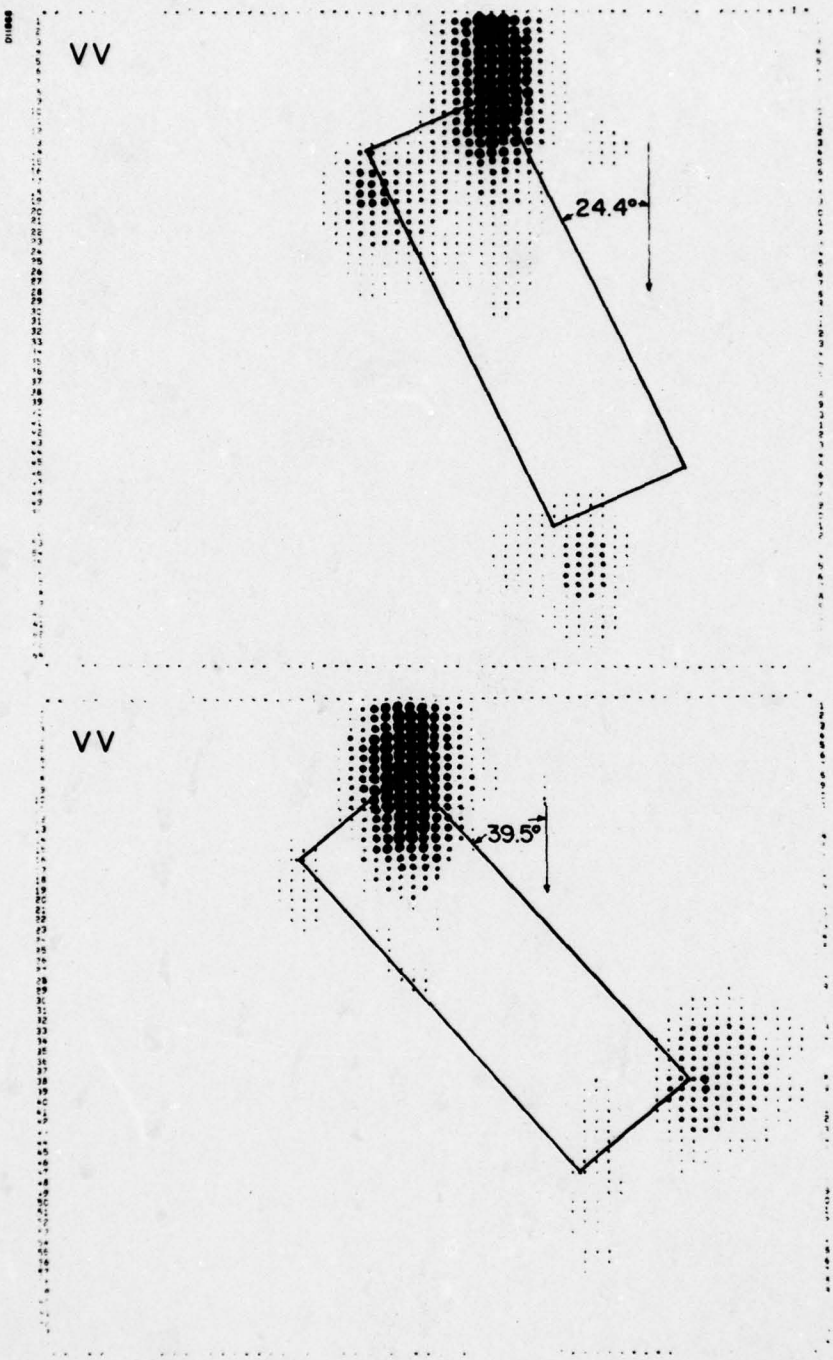

Figure 9. Radar Images of a Cylinder from Measurements Data, 24.4° and 39.5° Aspects, VV Polarization, 0 dB Transmitter Attenuation

include a reception point in cross range at the shadow boundary just above the peak in intensity, and a possible path along part of the shadowed edge and back through the opposite shadow boundary region. Further investigation of this phenomenon was not pursued here other than to obtain estimates of signal amplitudes which will be presented later.

A well known first order geometric diffraction theory formula, described in Appendix A, was used to simulate radar images of the illuminated edges in a manner comparable to the cube data simulation above with results for one aspect given in Figure 10, which is for a condition similar to that for Figure 8. Figure 8 compares well with Figure 10 with only slight differences in relative intensities, a result typical of those at other aspect angles for which simulations were made.

Images from measurements data were calculated for several aspects in addition to those shown here, and radar cross section estimates were made for scattering center peaks with numerical results listed in Table II. (Edges are defined in the sketch of Figure 11.) As in the cube case, but for a smaller angle span, these are an angle averaged form of amplitude estimate. Plots of these data points are given in Figure 12 together with curves based on the single frequency, geometric theory of diffraction formula without angle averaging. The measured points agree with the theoretical curves within 1 to 2 dB but there are deviations, particularly in the VV data for the two illuminated edges further in slant range. The fourth or shadow region amplitudes are also plotted in Figure 12 and listed in Table II, and these estimates decrease slowly with angle away from end-on aspect.

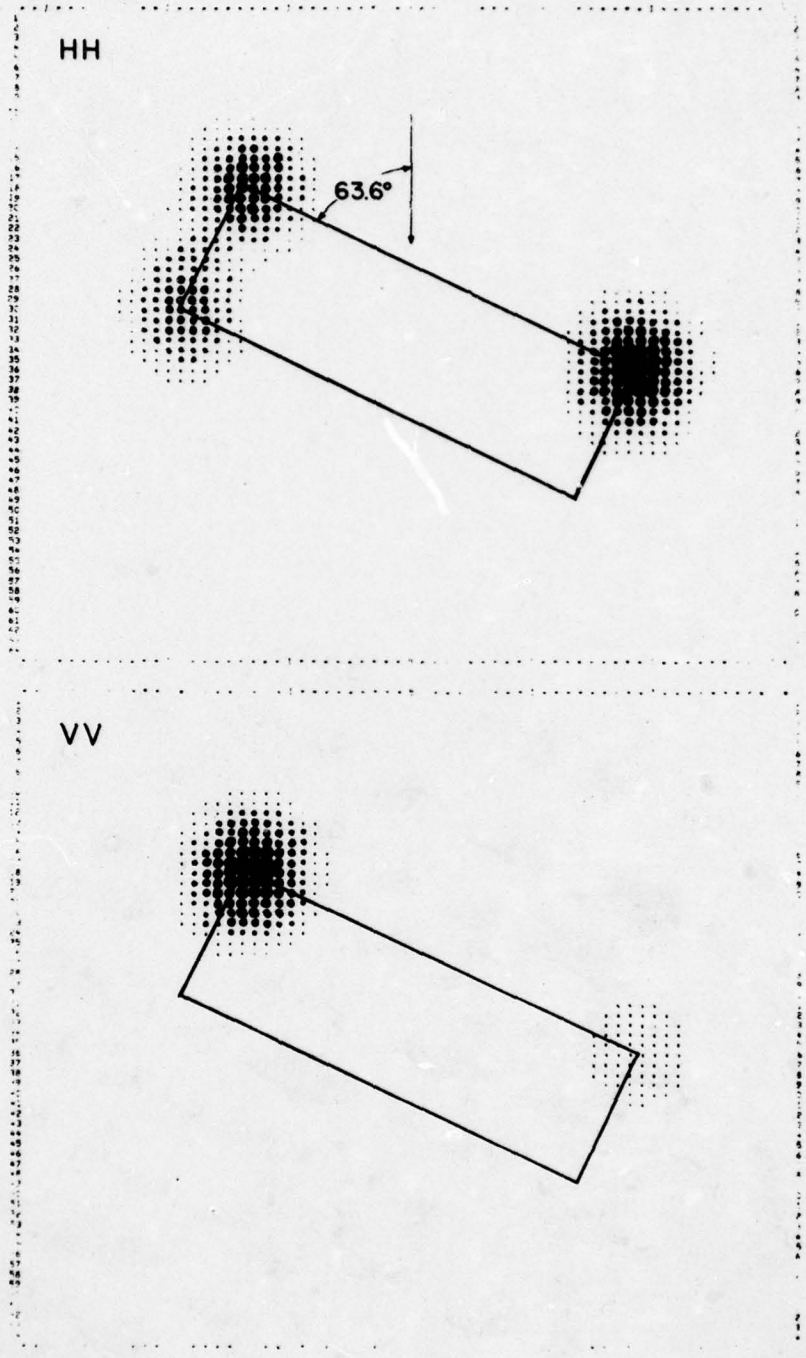

Figure 10. Radar Images of a Cylinder from Geometric Diffraction Theory, 63.6° Aspect, HH and VV Polarizations

A11877

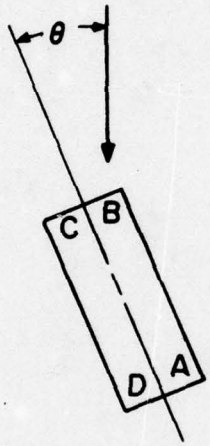

Figure 11. Sketch of Cylinder Projection Defining Scattering Edges and Aspect Angle

A11521

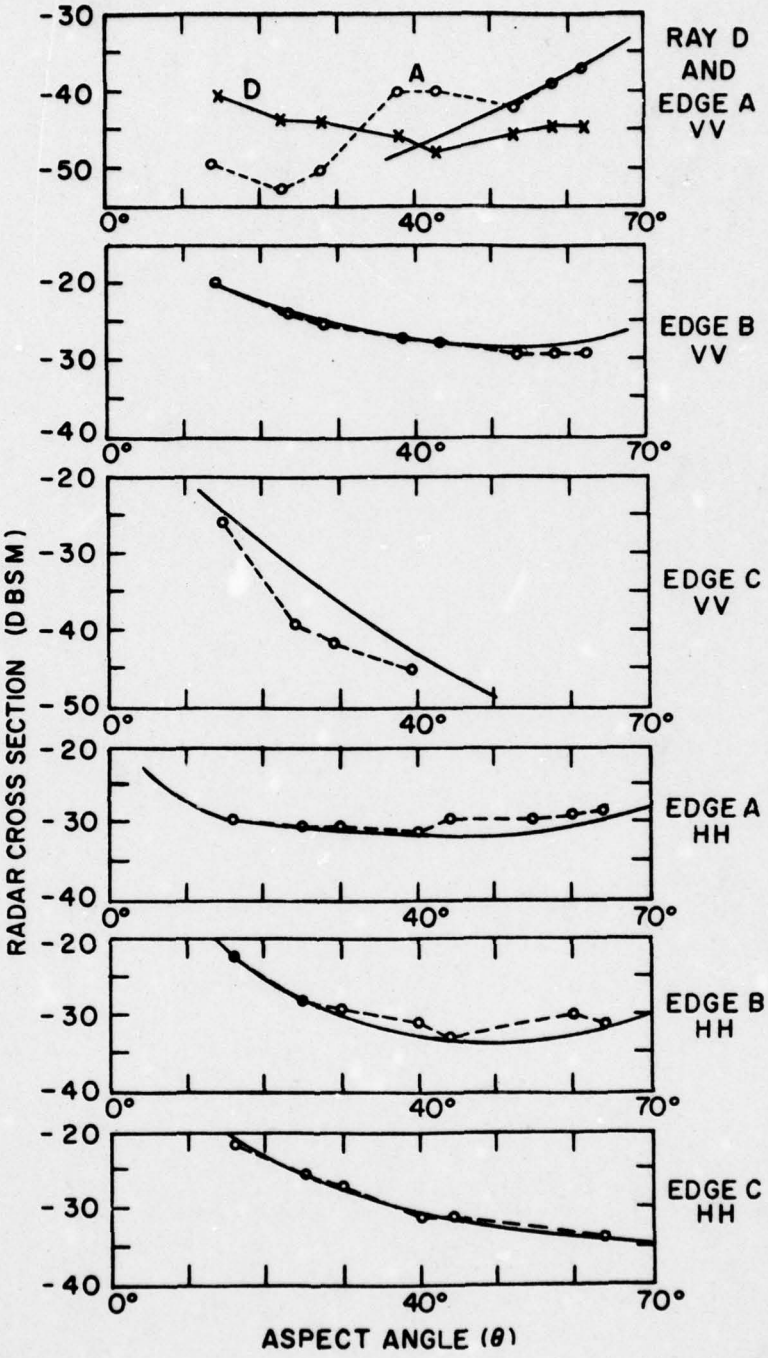

Figure 12. Plots of Cylinder Edge Radar Cross Section Values from Image Processing and Curves from Diffraction Theory. Ray D refers to a Shadow Region Reflection Effect.

Table II. Radar Cross Section Values in dBsm Versus Aspect Angle in Degrees for Rays from Edges of a 7 by 21 Cylinder Using Radar Image Processing of Measurements Data

VV POLARIZATION				
Aspect	Radar Cross Section of Edges			
θ	A	B	C	D Region
15.5	-49.4	-20.1	-26.0	-40.4
24.5	-52.6	-24.0	-39.6	-43.3
29.6	-50.4	-25.6	-42.0	-44.0
39.6	-40.3	-27.4	-45.7	-45.9
44.6	-40.2	-28.0	——	-48.0
54.4	-42.5	-29.9	——	-45.9
59.6	-39.6	-29.6	——	-44.9
63.6	-38.5	-29.4	——	-45.2
HH POLARIZATION				
15.5	-30.0	-22.6	-21.7	
24.6	-30.8	-28.4	-25.9	
29.6	-30.8	-29.8	-25.9	
39.6	-31.6	-31.7	-31.7	
43.7	-30.0	-33.3	-31.6	
54.6	-30.3	——	——	
59.5	-29.8	-31.0	——	
63.6	-29.1	-31.7	-34.4	

THIN STEEL ROD

The thin steel rod was about 17 wavelengths long, and multiple ray effects were expected, involving diffraction at the ends of the rod, and waves travelling along the rod length. Available first-order theories were not expected to give the correct magnitude of signal amplitudes since these theories did not include losses due to surface impedance effects which are expected to be significant in the case of a steel material. However, comparisons to these theories were made in terms of locations of ray responses in the radar images. Amplitude differences were used to estimate losses. Thin wire ray effects with short radar pulses were earlier studied by Borison and Hong [6] in short pulse data including only amplitude, which required taking into account a number of rays of approximately equal slant range in a single reflected pulse combination. In the results presented here, coherent processing allowed an almost complete separation of the rays unresolved in slant range when the aspect angles included in an integration were sufficiently away from end-on. A good cross range separation was not obtainable in the aspect region of the CW end-fire lobe which peaked at about 10° from end-on.

The rotation axis was perpendicular to the rod axis, making HH the principal polarization, and only results from that polarization will be presented. Radar images of the steel rod are shown in Figures 13, 14 and 15, for three different center aspect angles. Two images are shown in each figure: one for a linear output in six quantization levels similar to the previous images, the second with greater emphasis on lower amplitudes obtained by taking the square root before quantizing the amplitudes. The second brought out noise effects which predominate near the center of the cross range scale. The cross range processing included 19 angle samples in 1.0 degree increments, giving a theoretical 2.6 inch (6.5 cm) resolution and 0.59 inch (1.5 cm) cross range increment. Slant range was sampled more sparsely to give a longer slant range coverage and the slant range increment for Figures 13, 14 and 15 is 1.02 inches (2.59 cm). The rod sketched in the image changes apparent length with center aspect angle because of the rather wide difference in slant range and cross range scales. Figure 16 gives sketches and nomenclature

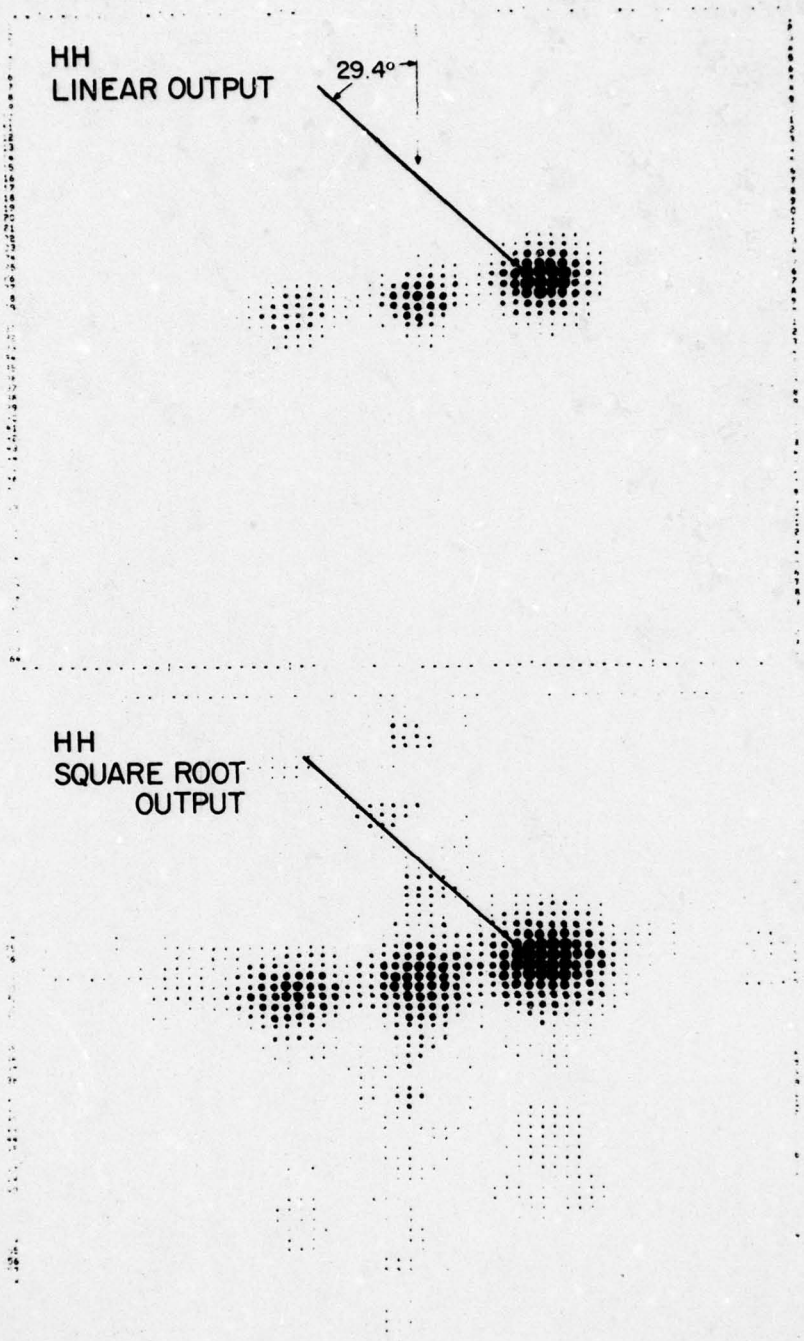

Figure 13. Radar Images of a Thin Steel Rod from Measurements Data, 29.4° Aspect, HH Polarization, Linear and Square Root Outputs

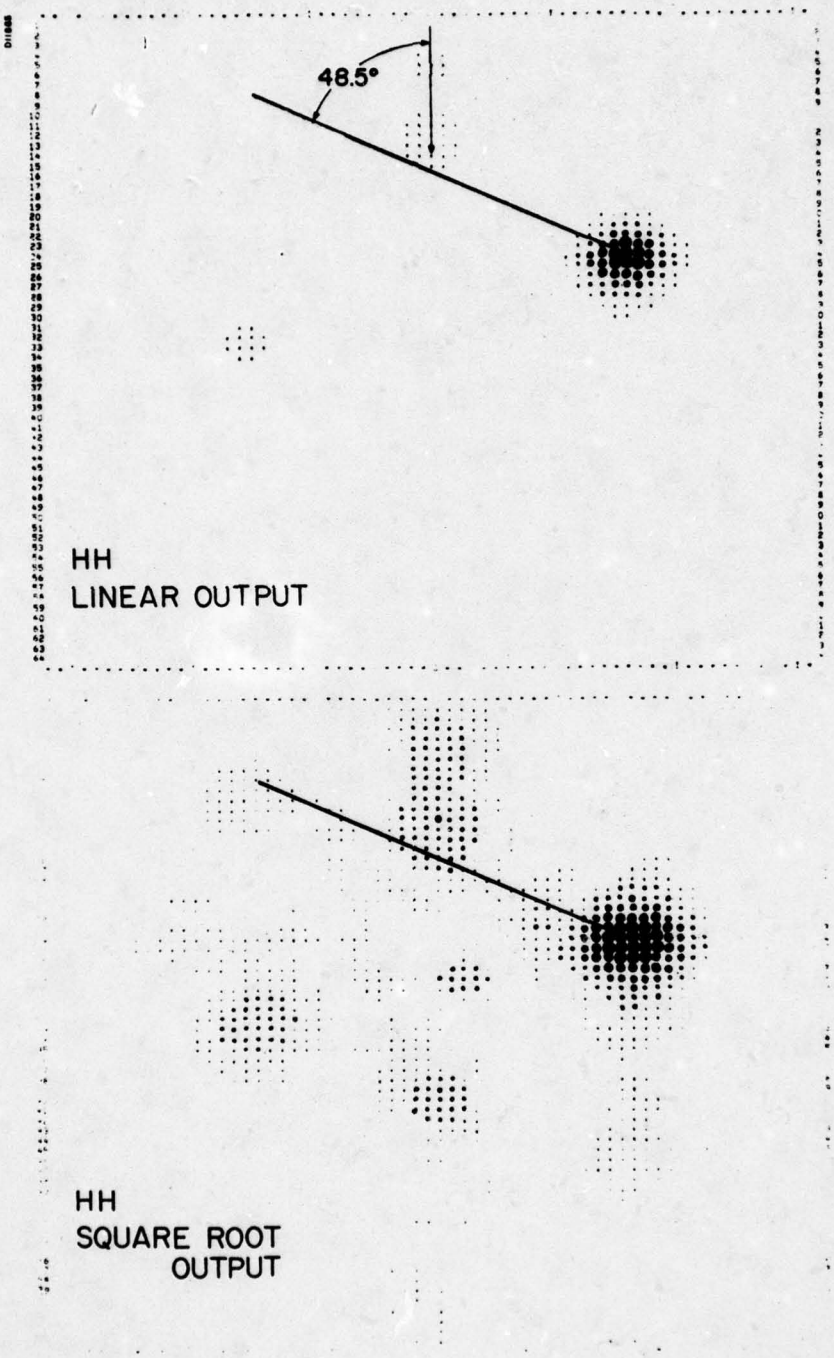

Figure 14. Radar Images of a Thin Steel Rod from Measurements Data, 48.5° Aspect, HH Polarization, Linear and Square Root Outputs

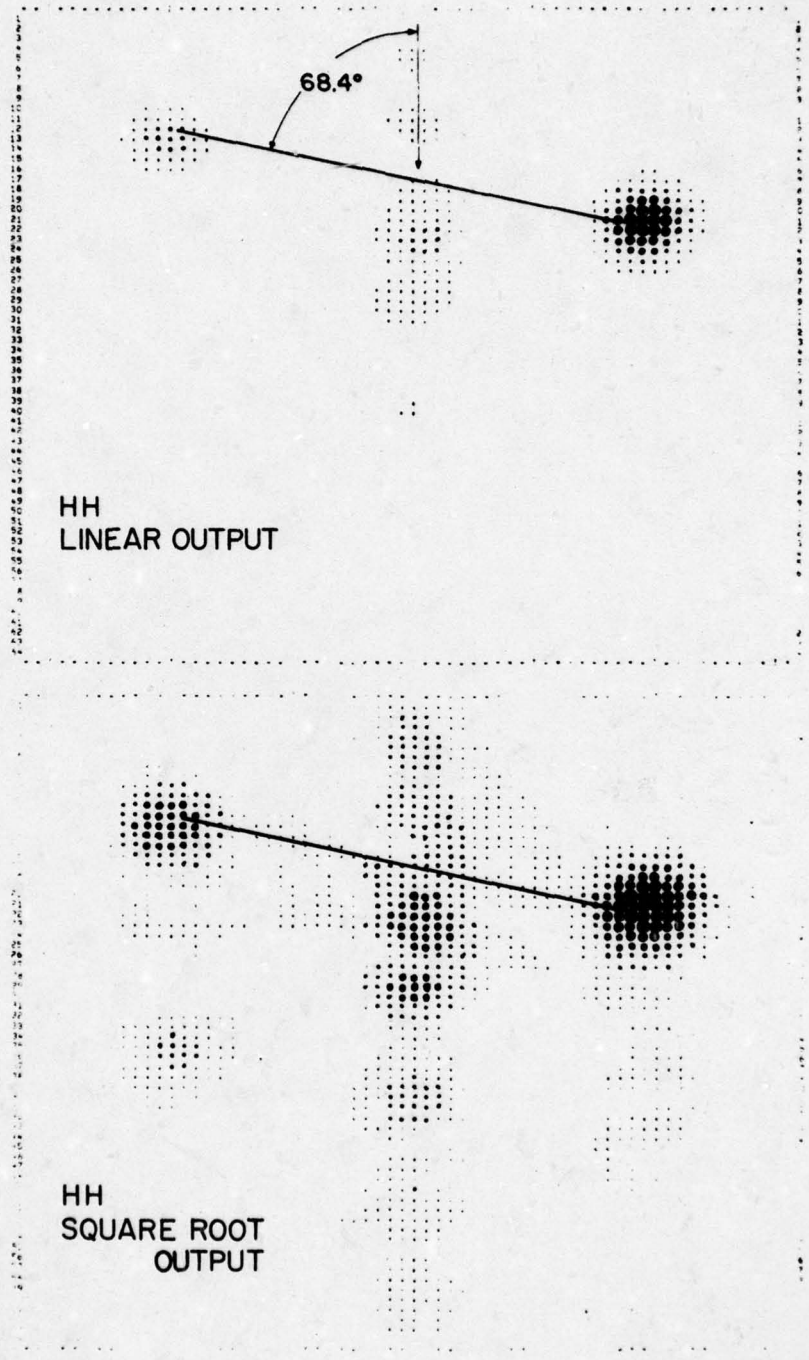

Figure 15. Radar Images of a Thin Steel Rod from Measurements Data, 68.4° Aspect, HH Polarization, Linear and Square Root Outputs

A11874

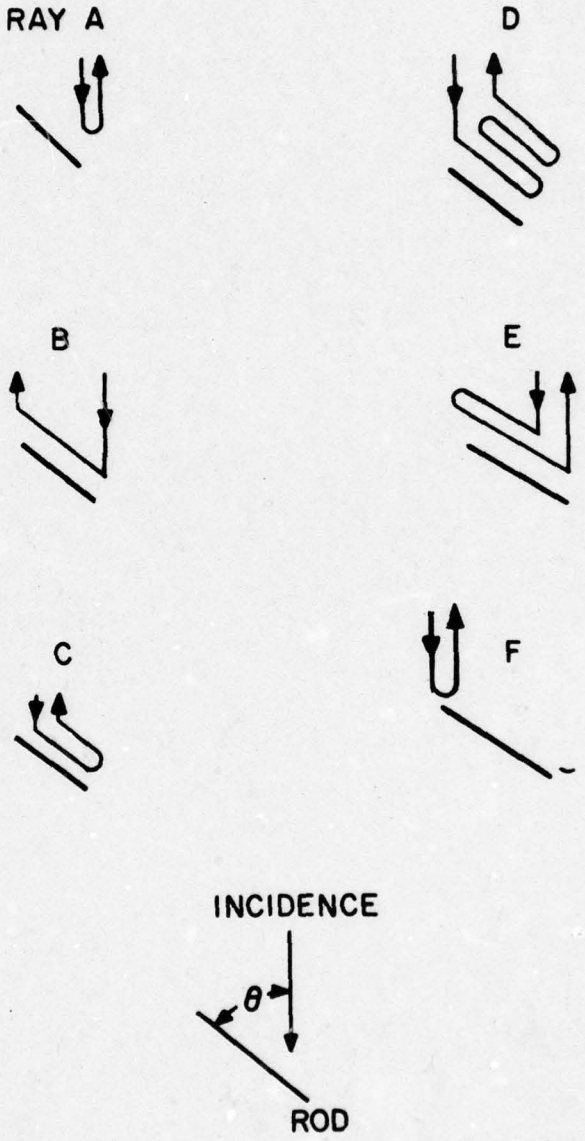

Figure 16. Sketches Defining Ray Paths Along Rod Length and Aspect Angle

describing ray paths along the wire which could be correlated with peak signal areas in the previous three Figures.

The response of the far end direct ray (A) is dominant in all of the images. The near end direct ray (F) is clearly evident in the near broadside aspect images.

A ray pair (B) produced echoes which appear clearly in Figure 13 near the center of rod in cross range, but displaced from the center by half a rod length in slant range. The centering of the cross range position is explained as follows: a ray entering at one end of the rod encounters a phase change due to motion of that end which is equal in magnitude of displacement but opposite in sign to motion of the end from which reradiation occurs, giving a net phase shift equal to that of the center of the rod. The single trip along the rod causes the half rod length slant range displacement from the center. As broadside aspect is approached in the series of images, this ray pair becomes lost in the noise effects. Thin wire diffraction theory for ideal conductors indicates that the ray entering the far end and reradiating from the near end should predominate over the ray entering the near end at most aspect angles away from broadside, so the center image responses might be assumed as isolating one ray.

A one round trip ray (C) associated with the near end gave a response identified by an image signal peak at the cross range of the near end but displaced in slant range by one rod length. A similar round trip ray (E) via the far end is detectable in the image. Only one double round trip ray (D) is detectable which is that associated with the near end. Other multiple travel rays gave responses too weak for detection in the available data and were lost in the noise.

Radar cross section values were estimated for the six detected ray scattering centers in a manner similar to that for the cube and cylinder. Values for a number of center aspects, including those of the previous figures, are listed in Table III.

Theoretical simulations were made using Ufimtsev's formula, described in Appendix A, for an ideal conductivity thin wire. Since this formula was based on a direct summation of rays diffracted from the ends of a wire as if

Table III. Radar Cross Section Values in dBsm Versus Aspect Angle in Degrees for Rays from a Thin Steel Rod Using Radar Image Processing of Measurements Data of HH Polarization

Aspect	Radar Cross Section of Rays					
θ	A	B	C	D	E	F
21.4	-43.0	-42.5	-46.4	-66.7	-63.9	-72.4
29.4	-44.8	-48.2	-51.0	-72.0	-66.5	-71.4
39.4	-46.4	-59.0	-56.9	-75.2	-71.0	-70.3
48.5	-47.4	-63.4	-61.1	--	-69.2	-67.6
58.4	-48.5	--	-62.7	--	-70.5	-61.2
68.4	-47.6	--	-64.6	--	-70.2	-54.7

semi-infinite, the rays are clearly evident in the terms of the equation. Radar images of the rod were simulated as in the cube and cylinder cases but using Ufimtsev's theory for the CW response input. Results are shown in Figure 17 for two aspect angles which can be compared to the upper frames in Figures 14 and 15. The clear difference between this theory and the measurements is that the single length ray (B) is dominant in the theoretical images while the far end direct ray (C) dominates the steel rod data.

Of curious interest was a comparison of results from the earlier, well known Van Vleck, et al., paper in which an integral equation solution (Method B) was extended to a long wire case (equation 34b in reference [8]). In the Van Vleck formulation, all of the ray effects are not as obvious in the terms of the equation. Simulated images in Figure 18 are based on the Van Vleck formula and are quite comparable to the Ufimtsev result in Figure 17 with the exception of an obviously spurious ray appearing ahead of the rod. Ray amplitudes of the Van Vleck theory were estimated from the simulated images for three angles, and listed in Table IV for comparison to Ufimtsev theory. The higher magnitude ray amplitudes (A) (B) are quite similar but, others deviate.

In examining the spurious echo in the Van Vleck result, another image simulation was made with a longer slant range coverage by sampling at wider slant range increments. The result in the bottom frame in Figure 19 clearly shows a number of additional spurious rays ahead of the rod in addition to the one seen in Figure 18. The bottom frame in Figure 19 was obtained by modifying the linear image output with a 0.2 exponent. Checks were made which insured that these spurious rays were not caused by the sampled data ambiguity effect in the slant range simulation.

Figure 20 gives a plot of the radar cross section values obtained from the radar imaging of the steel rod and also a set of curves based on the individual ray terms in Ufimtsev's formula. (The theoretical curves were from unaveraged CW values, but they compared closely with theoretical averaged amplitudes such as those in Table IV.) There may be some surprise in the rather large apparent attenuation effect between the direct ray theoretical amplitudes and those of the measured data, although the multiple ray amplitude

Table IV. Thin Wire Ray Radar Cross Section Values in dBsm Versus Aspect Angle in Degrees from Radar Image Processing Using Two First-order Theories

VAN VLECK THEORY						
ASPECT	RADAR CROSS SECTION OF RAYS					
θ	A	B	C	F	E	SPURIOUS
29.4	-33.1	-31.2	-45.	-48.9	-54.4	-43.4
48.5	-39.8	-38.9	-53.0	-62.0	-60.6	-51.0
68.4	-40.4	-42.8	-58.2	-49.3	-62.4	-55.0
UFIMTSEV THEORY						
29.4	-34.9	-31.5	-41.5	-68.6	-48.5	
48.5	-39.5	-38.0	-49.1	-62.7	-53.6	
68.4	-39.6	-41.4	-53.5	-50.6	-55.7	

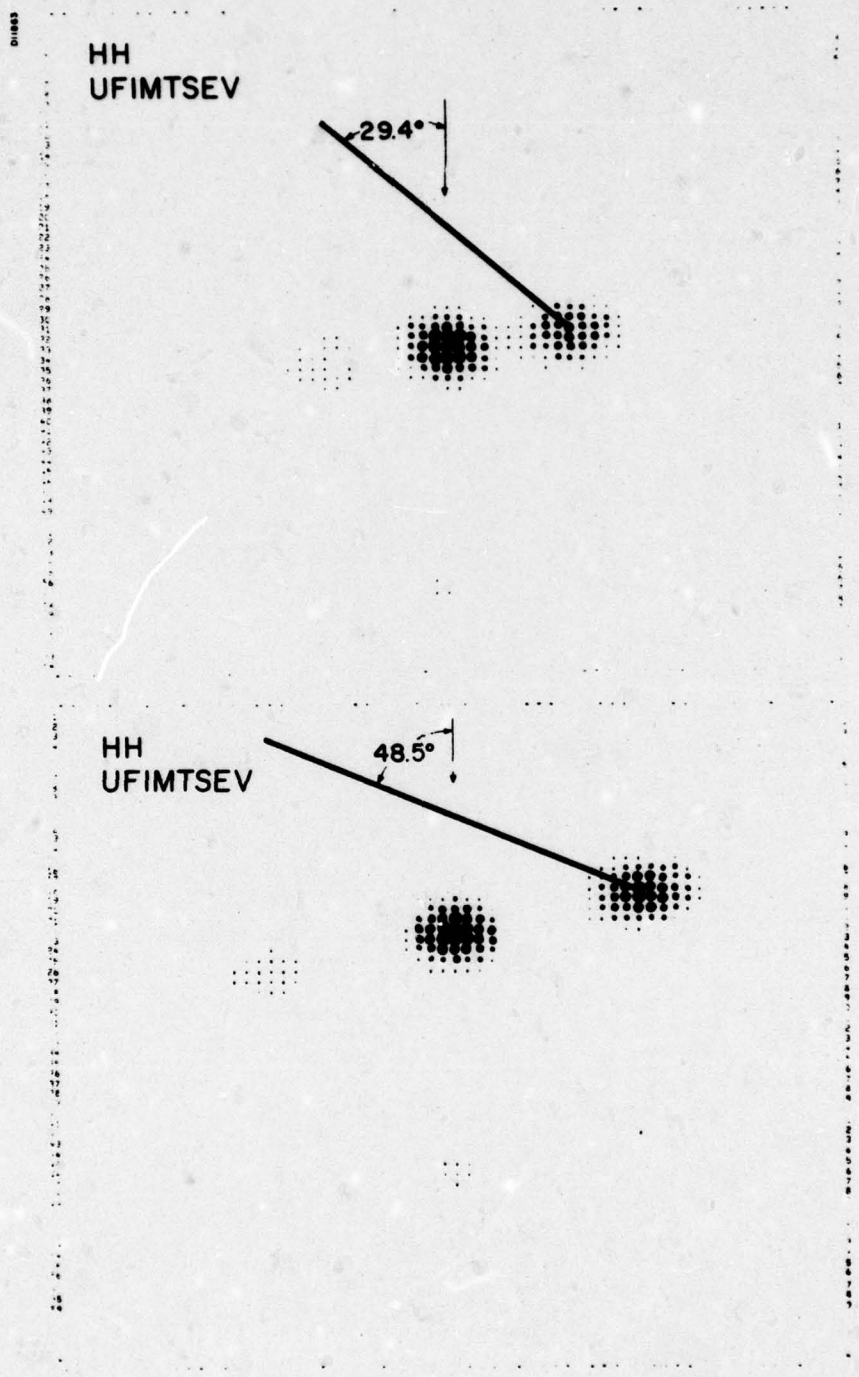

Figure 17. Radar Images of Ideal Conductor Thin Rod from Ufimtsev Theory, 29.4° and 48.5° Aspects, Linear Outputs

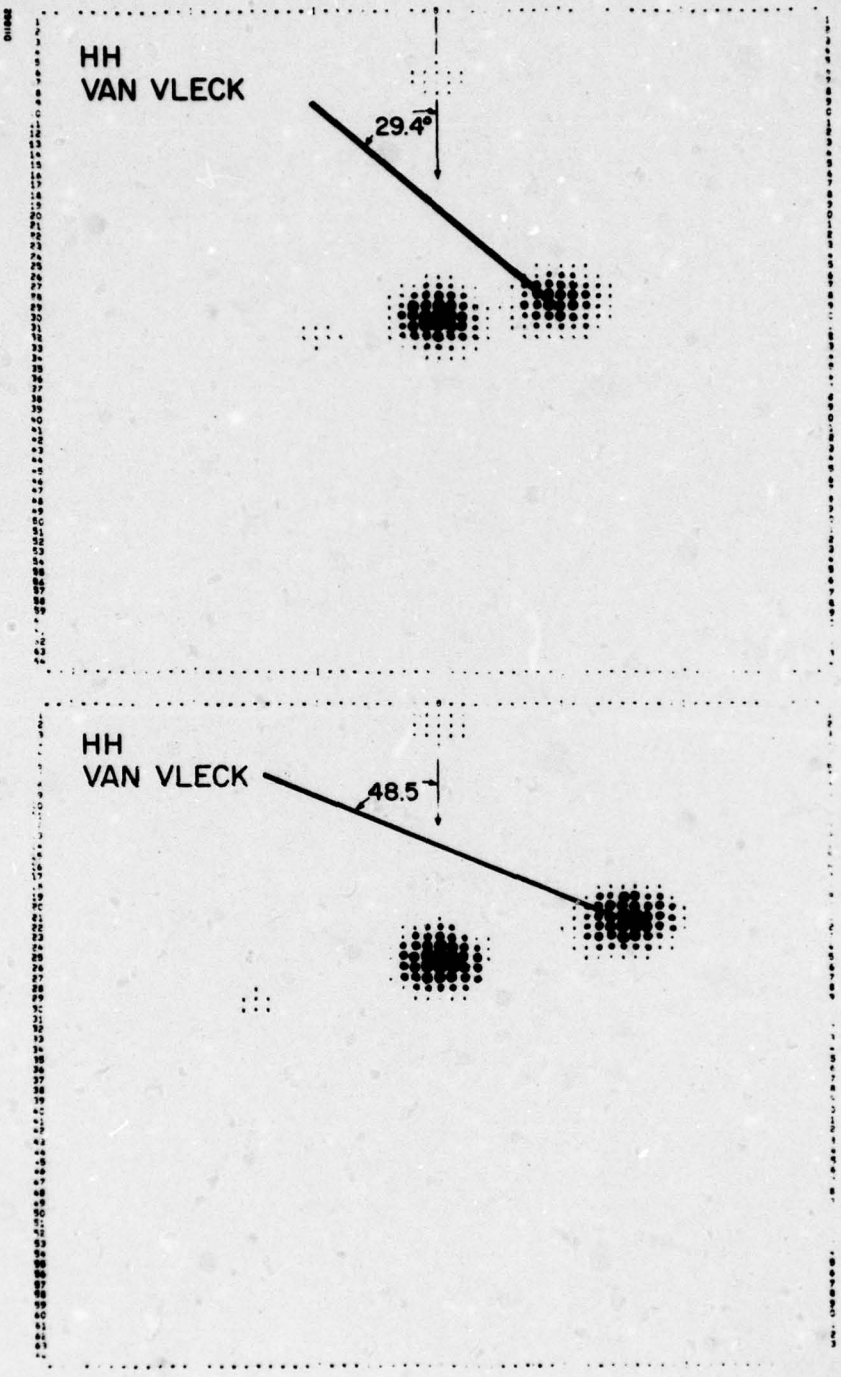

Figure 18. Radar Images of Ideal Conductor Thin Rod from Van Vleck Theory, 29.4° and 48.5° Aspects, Linear Outputs

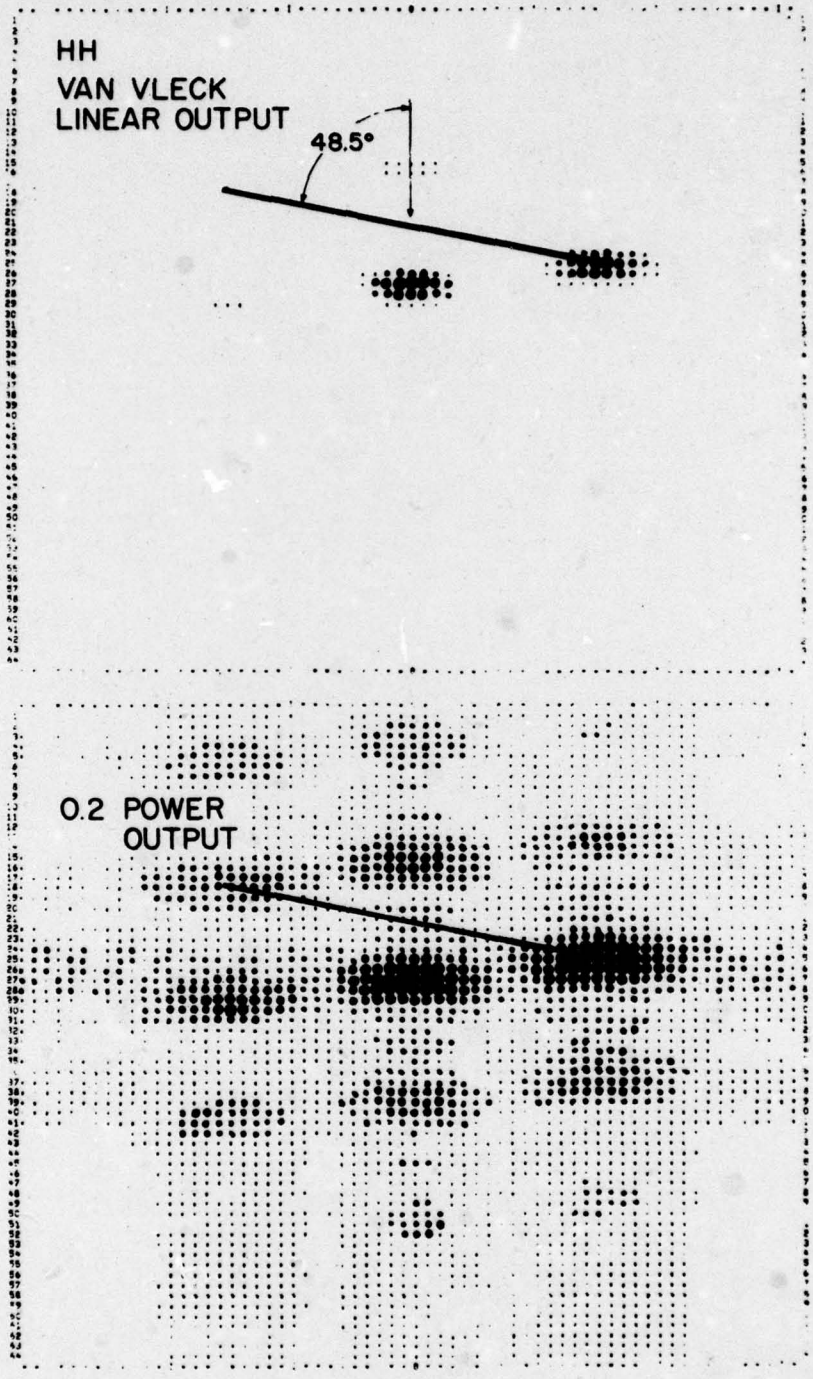

Figure 19. Radar Images of Ideal Conductor Thin Rod from Van Vleck Theory, 48.5° Aspect, Linear and 0.2 Power Outputs, Slant Range Scale Increment Doubled

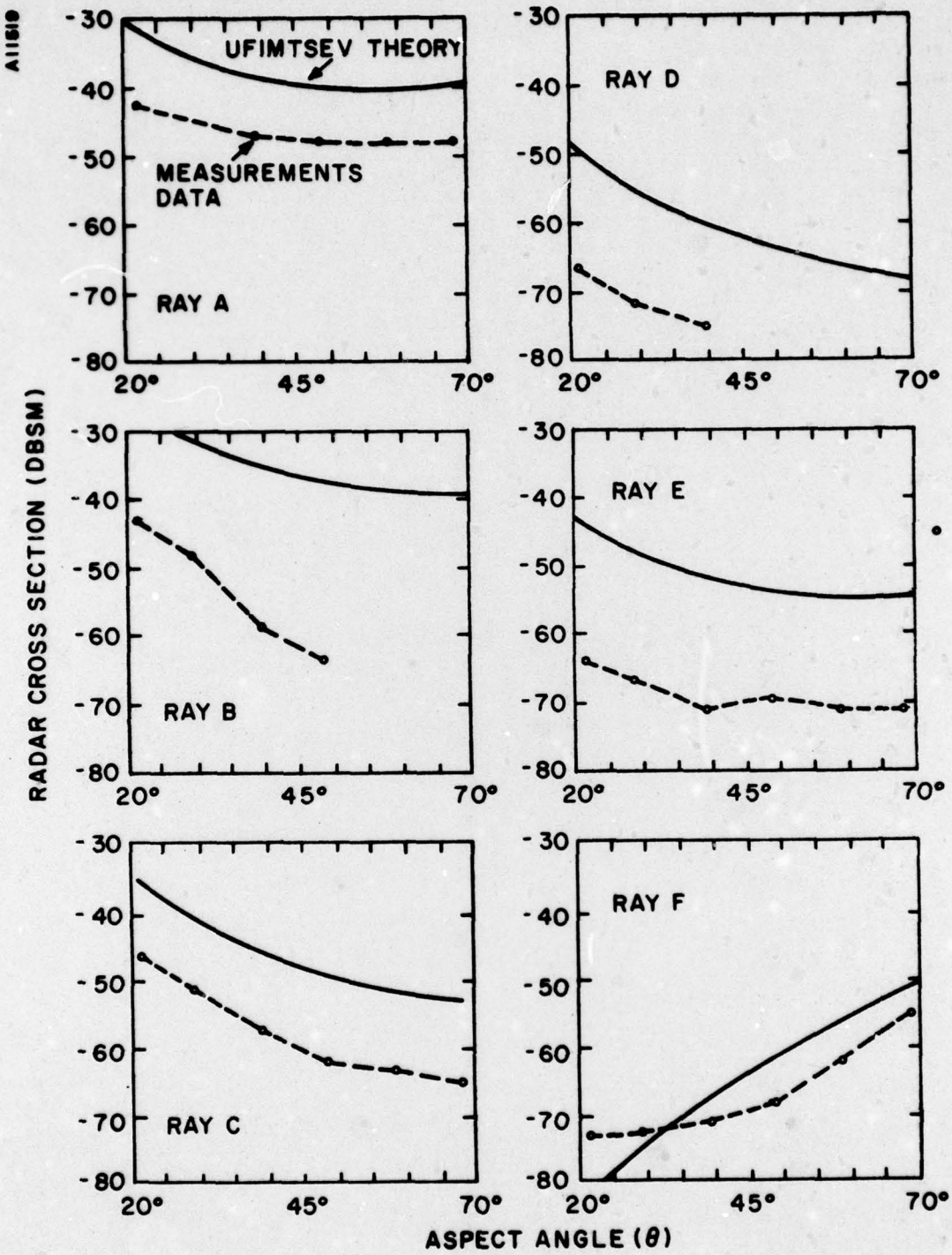

Figure 20. Plots of Radar Cross Section Values of Steel Rod Rays from Image Processing of Measurements Data and Curves from Ufimtsev's Ideal Thin Wire Theory

attenuations are as expected. The near end direct ray appears somewhat less attenuated than the far end direct ray. For signals outside the center cross range position, the lower threshold effect for these rod data appears to begin about -70 dBsm, and accuracy of estimates below this value is more questionable. However, the deviation of the near end direct ray (F) curve from the trend of the Ufimtsev curve may be a truer estimate since the actual rod diameter of 0.08 wavelengths is rather thick compared to the more usual thin wire values and the direct ray scattering from the flat end may be of a different mechanism than predicted by the Ufimtsev theory.

CONCLUSIONS

Coherent processing of wideband radar digital data in producing synthetic aperture displays is quite useful in isolating "scattering centers" on simple target configurations and in studying the amplitude versus aspect angle characteristics of the isolated scattering regions. The resulting data represent averages over the aspect angle scan used in the processing, but scattering from simple body discontinuities does tend to vary slowly with angle, and the averaging effect might not be a serious handicap, as is evident in the results for the three simple shapes presented here.

APPENDIX A

DIFFRACTION THEORY FORMULAS USED IN SIMULATIONS

Based on first order single diffraction wedge theory [2] - [5] the following functions were used to describe CW monostatic radar reflection amplitudes or the cube and cylinder. First for a section of semi-finite wedge of height, H, with incidence perpendicular to the edge nearest the radar

$$\sqrt{\sigma} = \frac{H}{\sqrt{3\pi}} \left\{ \frac{-1}{\frac{1}{2} + \cos(2\pi/3 + 4\theta/3)} \pm 2/3 \right\} \qquad (10)$$

where θ is an angle between direction of incidence and the perpendicular to a side. Upper sign is for linear polarization received and transmitted parallel to the edge (VV) lower sign for the orthogonal case (HH). The absolute magnitude squared will give the commonly used radar cross section term. For a total cube simulation three such terms were used with proper a spect angle considerations and phase terms determined by relative distances along the incidence direction.

A similar equation was used for the cylinder edge of radius, R, incidence assumed perpendicular to the edge tangent

$$\sqrt{\sigma} = \sqrt{\frac{R}{3k \sin\theta}} \left\{ \frac{-1}{\left[\frac{1}{2} + \cos(2\pi/3 + 4\theta/3)\right]} \pm 2/3 \right\} \qquad (11)$$

where $k = 2\pi/\lambda$, λ = wavelength. The above formula is for the nearest cylinder edge of three illuminated edges, and θ is the angle between incidence direction and the cylinder axis. Returns from the other two edges were derived from the above with the proper adjustment to θ, and relative phase angles were obtained from the geometric slant range displacements of the edges at various values of θ. The total CW echo was then a complex sum of the three terms. Polarizations VV and HH are given by upper and lower

signs, respectively.

Based on a semi-infinite thin wire diffraction theory, Ufimtsev [7] - [8] gave a formula for a length, L, radius, a, and angle of incidence from end-on, θ, of the form

$$\sqrt{\sigma} = \left\{ (2\pi/k) \frac{2i\, s(\theta)}{\sin\theta \sin 2\theta \left[\ln \left(\frac{2i}{\gamma ka \sin\theta} \right) \right]^2} \right\} \qquad (12)$$

where

$$s(\theta) = -\left\{ \sin^4(\theta/2) \ln \frac{i}{\gamma ka \sin^2 \theta/2} \right\}$$

$$+ e^{i2kL\cos\theta} \cos^4(\theta/2) \ln \left[\frac{i}{\gamma ka \cos^2(\theta/2)} \right]$$

$$- e^{ikL(1+\cos\theta)} \cos^4(\theta/2) \ln \left[\frac{i}{\gamma ka \cos(\theta/2)} \right] 2\, \psi_+$$

$$+ e^{ikL(1+\cos\theta)} \sin^4(\theta/2) \ln \left[\frac{i}{\gamma ka \sin(\theta/2)} \right] 2\, \psi_-$$

$$+ \left\{ \frac{1}{D} \left[(\psi_+)^2 + (\psi_-)^2 e^{ikL2(1+\cos\theta)} \right. \right.$$

$$\left. \left. - 2\psi_+ \psi_- \psi\, e^{ikL(3+\cos\theta)} \right] \cos\theta \ln \left(\frac{i}{\gamma ka} \right) \right\}$$

$$D = 1 - \psi^2 e^{i2kL}$$

$$\frac{1}{D} = \sum_{n=0}^{\infty} \psi^{2n} \epsilon^{i2nkL}$$

$$\psi = \frac{i\pi - 2 \ln (\gamma ka)}{\ln \left(\frac{i2kL}{\gamma k^2 a^2} \right) - E(2kL) \epsilon^{-2kL}}$$

$$\psi_{\pm} = \frac{i\pi - \ln (\gamma^2 q_{\pm})}{\ln \left(\frac{i2kL}{\gamma k^2 a^2} \right) - E \left(\frac{2kLq_{\pm}}{k^2 a^2} \right) e^{\left(-i2q_{\pm} \frac{kL}{k^2 a^2} \right)}}$$

$$q_{\pm} = \frac{(ka)^2}{2} (1 \mp \cos\theta)$$

$$E(x) = \int_{\infty}^{x} \frac{\epsilon^{it}}{t} dt$$

$$\gamma = 1.781$$

$$\ln = \log_e$$

$$i = \sqrt{-1}$$

APPENDIX B

ERRORS DUE TO LINEARITY ASSUMPTIONS

The radar cross section estimates presented in the main text were based on comparisons of peak image amplitudes of a rotating target to the peak amplitude of a fixed calibration target. A scattering center assigned a constant CW cross section with aspect angle will have an image response peak amplitude which decreases with distance from the center of rotation in a manner dependent on its position in a rotation cycle. This represents an integration loss due to signal processing not exactly matched to the rotating point target model. If the cross section estimates are used as representative of isolated phenomena dependent only on the local configuration of the scatterer, then the integration loss intoruces an error in the estimation. If the product of integration angle and distance from rotation center is small then this error might be neglected, depending on accuracy desired and relations to other measurement errors.

To obtain first order estimates of the errors due to integration loss, calculations were made assuming an ideal Gaussian pulse amplitude modulation, with the Hamming function in the angle dimension weighting, to simulate the model measurements and the linear processing. Second order functions were approximately fitted to the numerical results and these are valid in limited regions.

In the simulations, if a point moved only in slant range through a distance, Y_{sr}, during the integration through angle $\Delta\theta_m$, then the loss in peak amplitude was found to be approximately

$$L_{sr} \approx 0.43 \left(\frac{Y_{sr}}{\Delta R_{sr}}\right)^2 \quad , \quad \frac{Y_{sr}}{\Delta R_{sr}} < 2 \tag{13}$$

where L_{sr} is in units of dB, ΔR_{sr} is the 3 dB total width of the Gaussian pulse, and therefore the ratio $Y_{sr}/\Delta R_{sr}$ is the distance the point moved in units of slant range resolution. For the same condition, a degradation in cross range resolution from the ideal value, ΔR_{cr}, given by (8) of the main text was approximately described by a new resolution formula:

$$\Delta R_{cr}^{sr} \approx \left[1 + 0.044 \left(\frac{Y_{sr}}{\Delta R_{sr}}\right)^2\right] \Delta R_{cr} \quad , \quad \frac{Y_{sr}}{\Delta R_{sr}} < 2.5 \tag{14}$$

The above case might be representative of conditions when the line connecting a point is perpendicular to the radar incidence direction. When the connecting line is parallel to the incidence direction, the slant range motion is small but nonlinearity effects in the motion cause an effective motion through doppler resolution cells which also causes an error. Simulations were made for the latter condition assuming no slant range motion but a quadratic approximation for the cosine phase function of the rotating point. A theoretical loss factor was approximated by

$$L_{cr} \approx 0.17 \left(\frac{X_{cr}}{\Delta R_{cr}}\right)^2 \quad , \quad \frac{X_{cr}}{\Delta R_{cr}} < 2.5 \tag{15}$$

where L_{cr} is in units of dB, X_{cr} is the distance a point moved in cross range during integration, ΔR_{cr} is from (8) of the main text, and $X_{cr}/\Delta R_{cr}$ is therefore the cross range motion in units of ideal cross range resolution. The cross range resolution is also degraded from the ideal ΔR_{cr} case and this can be seen in the approximate new formula

$$\Delta R_{cr}^{cr} = \left[1 + 0.032 \left(\frac{X_{cr}}{\Delta R_{cr}}\right)^2\right] \Delta R_{cr} \quad , \quad \frac{X_{cr}}{\Delta R_{cr}} < 2.5 \tag{16}$$

where $X_{cr}/\Delta R_{cr}$ is the distance the point moved in cross range resolution units.

For motion less than the distance of a fixed point resolution cell, the above loss factors indicate an error of less than 0.5 dB and the degradation in cross range resolution is represented by a less than 5% increase. If these errors are intolerable for given problem conditions, then the approximate corrections might be applied as stated by the above approximations or by more accurate formulas, or a more accurate motion model can be used in the signal processing method. Introduction of the latter will increase complexity and costs of computation.

REFERENCES

[1] W.M. Brown, and R. J. Fredricks, "Range-Doppler Imaging with Motion through Resolution Cells", IEEE Trans. on Aerospace and Electronic Systems, Vol. AES-5, pp. 98-102, January 1969.

[2] J. B. Keller, "Diffraction by an Aperture", Journal of Applied Physics, vol. 28, pp. 426-444, April 1957.

[3] J. W. Crispin, Jr., R. F. Goodrich, and K. M. Siegel, Methods of Radar Cross Section Analysis, Academic Press, 1968, pp. 64-76.

[4] M. E. Bechtel, and R. A. Ross, "Radar Scattering Analysis", Cornell Aeronautical Laboratory Report, ER/RIS-10, August 1966.

[5] C. E. Ryan, Jr., and L. Peters, Jr., "Evaluation of Edge Diffracted Fields Including Equivalent Currents for the Caustic Regions", IEEE Trans. Antennas and Propagation, vol. AP-17, pp. 292-299, May 1969.

[6] S. Hong, S. L. Borison, D. P. Ford, "Short Pulse Scattering by a Long Wire," IEEE Trans. Antennas and Propagation, vol. AP-16, pp. 338-342, May 1968.

[7] P. Ya. Ufimtsev, "Diffraction of Plane Electromagnetic Waves by a Thin Cylindrical Conductor", Radio Engrg. Electron Physics (English Translation), vol. 7, pp. 241-299, 1962.

[8] J. H. Van Vleck, F. Block, M. Hamermesh, "Theory of Radar Reflection from Wires or Thin Metallic Strips", Journal of Applied Physics, Vol. 18, pp. 274-294, March 1947.

Additional Notes

UNCLASSIFIED

SECURITY CLASSIFICATION OF THIS PAGE (When Data Entered)

REPORT DOCUMENTATION PAGE

READ INSTRUCTIONS BEFORE COMPLETING FORM

1. REPORT NUMBER

2. GOVT ACCESSION NO.

3. RECIPIENT'S CATALOG NUMBER

4. TITLE (and Subtitle)
(6) Coherent and Wideband Imaging Analysis Handbook,

5. TYPE OF REPORT & PERIOD COVERED
(9) Training Course Notes,

6. PERFORMING ORG. REPORT NUMBER
(14) SRC-TR-75-148

7. AUTHOR(s)
(10) A. J. Moceyunas
~~or~~ R. J. Wallenberg

8. CONTRACT OR GRANT NUMBER(s)
(15) F41689-75-C-0141,
F41689-77-C-0006

9. PERFORMING ORGANIZATION NAME AND ADDRESS
Syracuse Research Corporation
Merrill Lane
Syracuse, NY 13210

10. PROGRAM ELEMENT, PROJECT, TASK AREA & WORK UNIT NUMBERS

11. CONTROLLING OFFICE NAME AND ADDRESS
Air Training Command, USAF
Randolph Air Force Base, TX 78148

12. REPORT DATE
(11) October 1976

13. NUMBER OF PAGES
246

14. MONITORING AGENCY NAME & ADDRESS (if different from Controlling Office)
(12) 209 p.

15. SECURITY CLASS. (of this report)
UNCLASSIFIED

15a. DECLASSIFICATION/DOWNGRADING SCHEDULE

16. DISTRIBUTION STATEMENT (of this Report)

17. DISTRIBUTION STATEMENT (of the abstract entered in Block 20, if different from Report)

18. SUPPLEMENTARY NOTES
None

19. KEY WORDS (Continue on reverse side if necessary and identify by block number)

apertures	model range data	radar images
broadband	motion	range (distance)
coherent radar	narrowband	rotation
images	parameter measurement	signal processing

20. ABSTRACT (Continue on reverse side if necessary and identify by block number)
This workbook contains part of the material for a training course in coherent narrowband and wideband radar signal analysis for size and shape estimation. Topics covered: signal processing methods, rotational motion simulation and parameter estimation, radar image relationships, and model range data examples.

420 003

DD FORM 1 JAN 73 1473 EDITION OF 1 NOV 65 IS OBSOLETE

UNCLASSIFIED

SECURITY CLASSIFICATION OF THIS PAGE (When Data Entered)